REPORT DOCUMENTATION PAGE

Form Approved OMB NO. 0704-0188

The public reporting burden for this collection of information is estimated to average 1 hour per response, including the time for reviewing instructions, searching existing data sources, gathering and maintaining the data needed, and completing and reviewing the collection of information. Send comments regarding this burden estimate or any other aspect of this collection of information, including suggesstions for reducing this burden, to Washington Headquarters Services, Directorate for Information Operations and Reports, 1215 Jefferson Davis Highway, Suite 1204, Arlington VA, 22202-4302. Respondents should be aware that notwithstanding any other provision of law, no person shall be subject to any oenalty for failing to comply with a collection of information if it does not display a currently valid OMB control number.
PLEASE DO NOT RETURN YOUR FORM TO THE ABOVE ADDRESS.

1. REPORT DATE (DD-MM-YYYY)	2. REPORT TYPE	3. DATES COVERED (From - To)
19-01-2012	Final Report	18-Nov-2004 - 17-May-2011

4. TITLE AND SUBTITLE	5a. CONTRACT NUMBER
Development of Flexible Extremities Protection utilizing Shear Thickening Fluid/Fabric Composites	W911NF-05-2-0006
	5b. GRANT NUMBER
	5c. PROGRAM ELEMENT NUMBER
	611104

6. AUTHORS	5d. PROJECT NUMBER
Mahesh Hosur, Norman Wagner, C.T. Sun, Vijaya Rangari, Jack Gillespie, Shaik Jeelani, Hassan Mahfuz	
	5e. TASK NUMBER
	5f. WORK UNIT NUMBER

7. PERFORMING ORGANIZATION NAMES AND ADDRESSES	8. PERFORMING ORGANIZATION REPORT NUMBER
Tuskegee University Tuskegee University 204 Kresge Center Tuskegee, AL 36088 -1923	

9. SPONSORING/MONITORING AGENCY NAME(S) AND ADDRESS(ES)	10. SPONSOR/MONITOR'S ACRONYM(S)
U.S. Army Research Office P.O. Box 12211 Research Triangle Park, NC 27709-2211	ARO
	11. SPONSOR/MONITOR'S REPORT NUMBER(S)
	47303-MS-BCE.42

12. DISTRIBUTION AVAILIBILITY STATEMENT

Approved for Public Release; Distribution Unlimited

13. SUPPLEMENTARY NOTES

The views, opinions and/or findings contained in this report are those of the author(s) and should not contrued as an official Department of the Army position, policy or decision, unless so designated by other documentation.

14. ABSTRACT

ABSTRACT

A systematic approach was undertaken to enhance spike resistance of flexible body armor. A traditional STF composite is consisted of fumed silica particles (about 7 nm in diameter but highly agglomerated due to van der Waals forces), PEG, and Kevlar. PEG is added to an aqueous suspension of silica and the solution is evaporated to

15. SUBJECT TERMS

STF, Flexible Armor, Kevlar, Spectra, Spike Test, Knife Test

16. SECURITY CLASSIFICATION OF:			17. LIMITATION OF ABSTRACT	15. NUMBER OF PAGES	19a. NAME OF RESPONSIBLE PERSON
a. REPORT	b. ABSTRACT	c. THIS PAGE			Shaik Jeelani
UU	UU	UU	UU		19b. TELEPHONE NUMBER
					334-727-8970

Standard Form 298 (Rev 8/98)
Prescribed by ANSI Std. Z39.18

Report Title

Development of Flexible Extremities Protection utilizing Shear Thickening Fluid/Fabric Composites

ABSTRACT

ABSTRACT

A systematic approach was undertaken to enhance spike resistance of flexible body armor. A traditional STF composite is consisted of fumed silica particles (about 7 nm in diameter but highly agglomerated due to van der Waals forces), PEG, and Kevlar. PEG is added to an aqueous suspension of silica and the solution is evaporated to remove water. This process of adding PEG to silica suspension and evaporation is continued several times until the concentration of silica to PEG comes around 55:45 by weight. At this ratio, the mixture is usually termed as Shear Thickening Fluid (STF) since it shows a sudden spike in viscosity at a certain shear rate when tested in a Rheometer. This sudden rise in viscosity is due to hydroclustering of silica particles within the carrier fluid, PEG. Such hydroclustering requires some movement and orientation of particles which is only possible when the carrier fluid is in liquid or in semi-liquid condition. Once STF is impregnated with Kevlar (with the help of ethanol, and subsequently dried) movement of silica particles are restricted further. Chances of hydroclustering and any alignment of particles to provide an instantaneous rise in viscosity and offer resistance to spike penetration are remote. It is therefore believed that under dry condition, resistance to spike penetration mostly comes from the energy required to (i) separate the filaments in fiber tows, (ii) deform the fiber, which is directly related to the elastic energy of the fiber, and (iii) plow through the particle-polymer-fiber layers – which is related to frictional energy. We believe, a considerable amount of energy is absorbed by steps (i) and (iii). Energy absorption in these two steps can be increased if we can increase the bonding between the three components; particle, polymer, and fiber. We cannot do much with the fiber deformation and fracture (step-ii) until its elastic energy and cut properties are improved. We focused on increasing the chemical bonding. Following steps were taken:

Size of the silica particles was increased to 30 nm to reduce agglomerations. These particles were then functionalized with a silane coupling agent to develop a bonding with PEG. This helped develop a Si-O-Si (siloxane) bond as evidenced in the FTIR spectra of silated silica. SEM pictures also showed that particles are highly clustered around the filament after functionalization. After functionalization of particles, spike resistance increased to 40 J-cm2/g. With regular STF composite, this value was around 15-20 J-cm2/g.

Since particles were treated with silane during functionalization, it was decided to remove PEG from the system and simplify the procedure. The objective was to increase bonding between particle and polymer which could be maintained without having PEG in there. However, the ratio of particle to polymer remained as before since we needed enough silica for frictional energy. NIJ tests indicated a spike resistance of 45 J-cm2/g, i.e., we did not loose any spike resistance.

Next, we attempted to develop a bonding between particle, polymer and Kevlar fiber. Treatment of silica particles with silane installs an amino functional group (N-H) on the surface of the silica particles. On the other hand, Kevlar also has an N-H (amide) functional group in its repeating amide group. Formaldehyde is an ideal tool to connect such pairs of amine. We decided to include Glutaraldehyde (Gluta) in our system. Use of this cross-linking fixative polymer (Gluta) allowed formation of three distinct bonds; C-N bonding, C-H band, and C-C stretch which were evidenced by FTIR spectra. These bonds were identified by their absorption frequencies. With the addition of Gluta, the peak for each of the three bonds increased indicating that the total number of bonds (i.e., cross-linking density) has increased. Such higher concentrations of chemical bonds allowed silica particles to bond much more intensely with the polymer and the Kevlar fiber. Spike resistance of this system was phenomenal – 220 J-cm2/g, almost 10 times more than that of regular STF-Kevlar system – an unprecedented materials property for flexible armor was achieved.

Enter List of papers submitted or published that acknowledge ARO support from the start of the project to the date of this printing. List the papers, including journal references, in the following categories:

(a) Papers published in peer-reviewed journals (N/A for none)

Received	Paper

2012/01/19 1? 41 Mahesh Hosur, Jessie Mayo, Eric Wetzel, Shail Jeelani. Studies on the fabrication and stab resistance characterization of novel thermoplastic-Kevlar composites, Solid State Phenomena, (02 2008): 0. doi:

2012/01/19 1? 40 Tarig Hassan, Vijaya Rangari, Shaik Jeelani. Sonochemical synthesis and rheological properties of shear thickening silica dispersion, Ultrasonics Sonochemistry, (02 2010): 0. doi:

2012/01/19 1? 38 Tarig Hassan, Vijaya Rangari, Shaik Jeelani. Synthesis, Processing and characterization of shear thickening fluid (STF) impregnated fabric composites, Materials Science and Engineering A, (01 2010): 0. doi:

2012/01/19 1(37 Jessie Mayo, Eric Wetzel, Mahesh Hosur, Shaik Jeelani. Stab and puncture characterization of thermoplastic-impregnated aramid fabrics, International Journal of Impact Engineering, (04 2009): 0. doi:

2012/01/19 1(23 Amanda Lim, Sergey Lopatnikov, Norman Wagner and John Gillespie. Investigating the transient response of a shear thickeningfluid using the split Hopkinson pressure bar technique, Rheol Acta, (06 2010): 0. doi:

2012/01/19 1(22 Amanda Lim, Sergey Lopatnikov and John Gillespie. Development of the split-Hopkinson pressure bar technique for viscousfluid characterization, Polymer Testing, (08 2009): 0. doi:

2012/01/19 0! 25 Amanda Lim, Sergey Lopatnikov, Norman Wagner and John Gillespie. Phenomenological modeling of the response of a dense colloidal suspensionunder dynamic squeezing flow, Journal of Non-Newtonian Fluid Mechanics, (04 2011): 0. doi:

2012/01/19 0! 29 Zhaoxu Dong, and C.T. Sun. Testing and modeling of yarn pull-out in plain woven Kevlar fabrics, Composites Part A: Applied Science and Manufacturing, (04 2009): 0. doi:

2012/01/19 0! 34 Dennis P. Kalman · Norman J. Wagner. Microstructure of shear-thickening concentratedsuspensions determined by flow-USANS, Rheol Acta, (03 2009): 0. doi:

2012/01/19 0! 33 Dennis Kalman, Richard Merrill, Norman Wagner, Eric Wetzel. Effect of Particle Hardness on the PenetrationBehavior of Fabrics Intercalated with DryParticles and Concentrated Particle-FluidSuspensions, Applied Materials, (11 2009): 0. doi:

2012/01/19 0! 36 Amanda Lim, Sergey Lopatnikov, Norman Wagner, John Gillespie. An experimental investigation into the kinetics of a concentrated hard-sphere colloidal suspension during Hopkinson bar evaluation at high stresses, Journal of Non-Newtonian Fluid Mechanics, (04 2010): 0. doi:

2012/01/19 0! 28 ZHAOXU DONG, JAMES M. MANIMALA AND C. T. SUN. MECHANICAL BEHAVIOROF SILICA NANOPARTICLE-IMPREGNATEDKEVLAR FABRICS, Journal of Mechanics of Materials and Structures, (05 2010): 0. doi:

2012/01/19 0! 14 Hassan Mahfuz, Floria Clements, Vijaya Rangari, Vinod Dhanak, and Graham Beamson. Enhanced stab resistance of armor composites with functionalized silica nanoparticles, Journal of Applied Physics, (03 2009): 0. doi:

TOTAL: 13

Number of Papers published in peer-reviewed journals:

(b) Papers published in non-peer-reviewed journals (N/A for none)

Received	Paper

TOTAL:

Number of Papers published in non peer-reviewed journals:

(c) Presentations

1.J. Mayo, Jr., A. Lewis, M. V. Hosur, S. Jeelani, "Cut Studies of Brittle and Ductile Fibers," SAMPE 2009 Conference, Baltimore, MD, May 2009

2.Vijaya K. Rangari, Tarig Hassan and Shaik Jeelani, "Synthesis and Mechanical Properties of Shear Thickening Fluid/Kevlar Composite for Body Armor Application," SAMPEE-2008, May 16-21, Long Beach, CA.

3.Hassan Mahfuz, Vincent Lambert, Patrick Bordner, and Vijaya Rangari, "Improving Stab Resistance of Flexible Body Armor using Silane Coupling Agents and Cross-linking Fixatives with Silica Nanoparticles," invited presentation at the 2008 ASME International Mechanical Engineering Congress and Exhibition (IMECE), Boston, MA, Oct. 31 – Nov. 6, 2008.

4.Mahfuz, H., Clements, F. and Justin, S., "Functionalization of Silica Nanoparticles to Improve Stab Resistance of Kevlar Fabrics," SES 2006, University Park, PA, August 13-16, 2006.

5.Mahfuz, H., Lambert, V. and Bordner, P., "Improving Stab Resistance of Flexible Body Armor using Silane Coupling Agent and Cross-Linking Fixatives with Silica Nanoparticles," ASME International Mechanical Engineering Congress and Exposition, October 31 – November 6, 2008, Boston, Massachusetts, Presented at the Conference.

6.International Congress on Rheology 2008, 8/5/2008, Effects of particle hardness on shear thickening colloidal suspension rheology, University of Konstanz, Germany, Department of Physics, 7/4/2008 (invited lecture), Microstructure of Shear Thickening Colloidal Dispersions: "STF Armor"- Nanoparticle Composites for Flexible Ballistic Materials.

7.SoftMatt-2008, 6/19/2008, – Micromechanics of concentrated, near hard-sphere suspensions (poster) 7.ACS Colloid and Surface Science Symposium,

8.NCSU, 6/16/2008 – Particle Hardness Effects on Concentrated Colloidal Suspension

9.Rheology, ACS Colloid and Surface Science Symposium, NSCU, 6/16/2008- The influence of Interparticle Interactions and Hydrodynamic Forces on Shear Thickening in Concentrated Colloidal Dispersions and Slurries

10.Chemical Engineering, UC Santa Barbara, CA, May, 2008 (invited lecture)- The Rheology Of Colloidal & Nanoparticle Dispersions: "Stf Armor™"- Nanoparticle Composites For Flexible Ballistic Materials.

11.Chemical Engineering, Purdue Univ. Indiana, Feb. 2008 (invited lecture) – The Rheology Of Colloidal & Nanoparticle Dispersions: "Stf Armor™"- Nanoparticle Composites For Flexible Ballistic Materials.

12.Chemical Engineering, UC Riverside, CA, Feb. 2008 (invited lecture) – The Rheology Of Colloidal & Nanoparticle Dispersions: "Stf Armor™"- Nanoparticle Composites For Flexible Ballistic Materials.

13.Rheophysics, ESCPI Paris, France, Jan. 2008- Shear-induced organization in colloidal dispersions: The hydrocluster microstructure in shear thickened colloidal suspensions

14."Investigating the High Strain Rate Compression Shear Behavior of a Discontinuous Shear-Thickening Fluid (STF)." 1st place award in the 21st Annual Technical Conference of the American Society for Composites Student poster competition.

15."Implementing the Split-Hopkinson Pressure Bar Technique for Viscous Fluid Evaluation." 1st place award in the 53rd International SAMPE Symposium and Exhibition, Long Beach CA, May 2008.

16. Sreedhar Poluchalla, Mahesh V. Hosur, Shaik Jeelani, "Investigations on the Stab Resistance of Kevlar Fabrics Impregnated with Shear Thickening Fluid," ASME International Mechanical Engineering Congress and Exposition, 15 November 2007, Seattle, WA

Number of Presentations: 1.00

Non Peer-Reviewed Conference Proceeding publications (other than abstracts):

<u>Received</u>   <u>Paper</u>

   TOTAL:

Number of Non Peer-Reviewed Conference Proceeding publications (other than abstracts):

Peer-Reviewed Conference Proceeding publications (other than abstracts):

Received	Paper

2012/01/17 1: 31   Zhaoxu Dong and C.T. Sun. Testing and Modeling of Yarn Pullout of Plain Woven Kevlar fabric, CompTest 2008. 2008/10/20 00:00:00, . : ,

2012/01/17 1: 30   Zhaoxu Dong and C. T. Sun. Modeling Nano-Particle Colloid/Fabric Composites, American Society for Composites (ASC). 2006/09/17 00:00:00, . : ,

2012/01/17 1: 18   Hassan Mahfuz, Vincent Lambert, Patrick Bordner and Vijaya Rangari. Development of Stab Resistant Body Armor Using Silated SiO2 Nanoparticles Dispersed into Glutaraldehyde, NSTI Nanotech 2008. 2008/05/04 00:00:00, . : ,

2012/01/17 1: 17   Floria Clements, Hassan Mahfuz, Eric Wetzel and Justin Stewart. M50/V50/A50 Method for Characterizing Stab Resistant Materials for Body Armor Applications, 2007 Society of Experimental Mechanics (SEM) Conference. 2007/06/03 00:00:00, . : ,

2012/01/17 1: 16   Hassan Mahfuz, Floria Clements and Justin Stewart. Development of Stab Resistant Body Armor Using Fumed SiO2 Nanoparticles Dispersed into Polyethylene Glycol (PEG) through Sonic Cavitation, NSTI-Nanotech 2006. 2006/05/07 00:00:00, . : ,

2012/01/17 1: 15   Floria Clements and Hassan Mahfuz. ENHANCING THE STAB RESISTANCE OF FLEXIBLE BODY ARMOR USING FUNCTIONALIZED SIO2 NANOPARTICLES, 16th International Conference on Composite Materials (ICCM-16), Kyoto, Japan. 2007/07/08 00:00:00, . : ,

2012/01/13 1: 13   J. B. MAYO, JR., M. V. HOSUR, S. JEELANI, E. D. WETZEL. Cut Behavior of High Performance Fibers, The 1st joint American- Canadian International Conference on Composites September 17, 2009. 2009/09/17 01:00:00, . : ,

2012/01/13 1: 12   H. Rao, , M.V. Hosur, , J. Mayo, Jr., , S. Burton, , S. Jeelani. Stab Characterization of Hybrid Ballistic Fabrics, 2009 Annual Society for Experimental Mechanics Conference, Albuquerque, NM, June 1-4, 2009.. 2009/06/02 01:00:00, . : ,

2012/01/13 1: 11   Jessie B. Mayo, Jr., , Andre Lewis, , Mahesh V. Hosur, , Shaik Jeelani. Cut Studies of Brittle and Ductile Fibers, SAMPE 2009 Conference, Baltimore, MD, May 2009. 2009/05/20 01:00:00, . : ,

2012/01/13 1: 10   Harish M Rao, Jessie Mayo. Jr., Mahesh V. Hosur, Shaik Jeelani. STAB CHARACTERIZATION OF BALLISTIC FABRICS IMPREGNATED WITH SHEAR THICKENING FLUID, Fall Meeting of the Society for Advancement of Materials and Process Engineering (SAMPE), Sept. 9-11, 2008, Memphis, TN. 2008/09/10 01:00:00, . : ,

2012/01/13 1: 9   M. V. Hosur, J. B. Mayo Jr., E. Wetzel, S. Jeelani. Studies on the Fabrication and Stab Resistance Characterization of Novel Thermoplastic-Kevlar Composites, International Conference on Materials for Advanced Technologies – ICMAT-2007, July 1-6, 2007, Singapore.. 2007/06/03 01:00:00, . : ,

2012/01/13 1: 8   J. B. Mayo, Jr. , M. V. Hosur, E.Wetzel, S. Jeelani. RESISTANCE OF NOVEL THERMOPLASTIC-KEVLAR COMPOSITES TO SPIKE PENETRATION, 2nd International Conference on recent advanced in composite materials, Feb. 20-23, 2007, New-Delhi, India. 2007/02/21 01:00:00, . : ,

2012/01/13 1: 7   Jessie Mayo B. Jr., , Mahesh V. Hosur, , Shaik Jeelani. Dynamic and Quasi-Static Stab Resistance of Thermoplastic and Silica-Polyethylene Glycol Gel Infused Fabrics, 22nd Annual Technical Conference of the American Society for Composites, . 2007/09/17 01:00:00, . : ,

TOTAL: **13**

Number of Peer-Reviewed Conference Proceeding publications (other than abstracts):

(d) Manuscripts

Received	Paper

TOTAL:

Number of Manuscripts:

Books

<u>Received</u>   <u>Paper</u>

   TOTAL:

Patents Submitted

Patents Awarded

Awards

1. Shaik Jeelani: 2011 Presidential Award for Mentoship - presented by President Obama at the White House on December 12, 2011.

2. Mahesh Hosur: 2009-2010 Faculty Performance Award for Research in the College of Engineering, Architecture and Physical Sciences.
Mahesh Hosur: Nominated by the College of Engineering for the Tuskegee University Faculty Achievement Award in Spring 2011.

3. Hassan Mahfuz: Researcher of the Year (FAU), 2008

4. Hassan Mahfuz: Elected Fellow of ASME, December 2010

5. Amanda Lim, 1st place award in the 21st Annual Technical Conference for the American Society for Composites, Student Poster Competition

6. Amanda Lim - 2nd place award at the 2007 SBaltimore-Washington SAMPE, Student Nite Competition

7. Amanda Lim - 1st place award in the 53rd International SAMPE Symposium and Exhibition, Long Beach, CA, May 2008

8. Amanda Lim - 1st place award in the 11th International Congress of the SEM Student Paper Symposium, Orlando, FL, June 2008

Graduate Students

NAME	PERCENT_SUPPORTED	Discipline
Harish Rao	0.50	
Sreedhar Reddy Poluchalla	0.50	
Jessie B. Mayo Jr.	0.50	
Jessie B. Mayo Jr.	0.70	
Amanda Lim	0.70	
Dennis Kalman	0.75	
James Manimala	0.75	
Z. Dong	0.75	
Floria Clements	0.75	
Vincent Lambert	0.75	
Justin Stewart	0.25	
Abiola Gaines	1.00	
Tarig Hassan	1.00	
Andrew Lewis	1.00	
Ron Egress	0.25	
FTE Equivalent:	**10.15**	
Total Number:	**15**	

Names of Post Doctorates

NAME	PERCENT_SUPPORTED
Jessie B. Mayo Jr.	0.75
Sergey Lopatnikov	0.50
Y. Zhou	0.25
Joe Deitzel	0.10
Bazle Gama	0.10
FTE Equivalent:	**1.70**
Total Number:	**5**

Names of Faculty Supported

NAME	PERCENT_SUPPORTED	National Academy Member
Mahesh Hosur	0.10	
Shaik Jeelani	0.05	
Vijaya Rangari	0.10	
Hassan Mahfuz	0.10	
Jack Gillespie	0.05	
Norman Wagner	0.05	
C.T. Sun	0.10	
FTE Equivalent:	**0.55**	
Total Number:	**7**	

Names of Under Graduate students supported

NAME	PERCENT SUPPORTED	Discipline
Andre Lewis	0.50	Mechanical Engineering
Shifra Burton	0.50	Chemical Engineering
Patrick Bordner	0.50	Ocean Engineering
DeAnna Sewell	0.50	Ocean Engineering
Jarmarius Keith	0.50	Mechanical Engineering
Joe Houghton	0.50	Mechanical Engineering
Emory Head	0.50	Mechanical Engineering
Keosha Forest	0.50	Mechanical Engineering
Brian Rosen	0.50	Materials Engineering
Monica Tubbs	0.50	Mechanical Engineering
Benjamin Schiffman	0.50	Chemical Engineering
Josh Schein	0.50	Chemical Engineering
Shanise Hudley	0.50	Mechanical Engineering
James McGovern	0.50	Mechanical Engineering
Amir Usher	0.50	Mechanical Engineering
Joe Houghton	0.50	Mechanical Engineering
Bryan Clayton	0.50	Mechanical Engineering
Chris Miller	0.50	Mechanical Engineering
FTE Equivalent:	**9.00**	
Total Number:	**18**	

Student Metrics
This section only applies to graduating undergraduates supported by this agreement in this reporting period

The number of undergraduates funded by this agreement who graduated during this period: 18.00

The number of undergraduates funded by this agreement who graduated during this period with a degree in science, mathematics, engineering, or technology fields:...... 18.00

The number of undergraduates funded by your agreement who graduated during this period and will continue to pursue a graduate or Ph.D. degree in science, mathematics, engineering, or technology fields:...... 10.00

Number of graduating undergraduates who achieved a 3.5 GPA to 4.0 (4.0 max scale):...... 8.00

Number of graduating undergraduates funded by a DoD funded Center of Excellence grant for Education, Research and Engineering:...... 8.00

The number of undergraduates funded by your agreement who graduated during this period and intend to work for the Department of Defense 13.00

The number of undergraduates funded by your agreement who graduated during this period and will receive scholarships or fellowships for further studies in science, mathematics, engineering or technology fields:...... 10.00

Names of Personnel receiving masters degrees

NAME
Jessie B. Mayo Jr.
Harish Rao
Sreedhar Poluchalla
Floria Clements
Vincent Lambert
Tarig Hasan
James Manimala
Total Number: 7

Names of personnel receiving PHDs

NAME	
Jessie B. Mayo Jr.	
Amanda Lim	
Dinnis Kalman	
Zhaoxu Dong	
Total Number:	**4**

Names of other research staff

NAME	PERCENT SUPPORTED
Dorothy Bernett	0.10
FTE Equivalent:	**0.10**
Total Number:	**1**

Sub Contractors (DD882)

Inventions (DD882)

Scientific Progress

Most significant accomplishments are as follows:

•A systematic study has been conducted to understand the cut and fracture behavior of various types of commercial fibers for potential application to flexible armor. Unique testing facilities have been developed at ARL to conduct these experiments. This component of the project has demonstrated an overwhelming amount of collaboration between Tuskegee University and ARL.

•It has been demonstrated that ultrahigh molecular weight polyethylene (UHMWPE) based fibers such as Spectra and Dyneema has superior cut resistance than that of Kevlar. The study also showed that S-glass fiber has very good potential for armor application. But further studies are needed to confirm this finding.

•A sonochemical procedure has been introduced to produce shear thickening fluid (STF) in large quantities. The procedure uses silica nanopowder dispersed into polyethylene glycol (PEG) using high frequency ultrasonic waves in presence of a solution. Large amount of solution and high intensity of irradiation allows uniform distribution of nanoparticles in the polymer.

•NIJ tests have demonstrated that Spectra provides more stab resistance than Kevlar as it was concluded in the cut and fracture studies. Multiple soaking of the fabric with silica-silane-Gluta solution have shown that knife resistance can be enhanced almost 3 times; from 6 J-cm2/g to 20 J-cm3 /g for zero-layer penetration.

•Micro droplet tests have indicated that dynamic friction at the fiber/matrix interface was responsible for such enhancement in knife resistance.

•A comprehensive study on the high strain rate behavior of STF has been completed. Complex relationship between particle volume fraction, strain rate, and onset of shear thickening has been deduced through mathematical formulations, and later validated through Hopkinson bar experiments.

•A two dimensional homogenized continuum model has been developed to characterize the non-linear anisotropic material properties of the neat and nanoparticle-impregnated fabrics under large deformation. Validation of the model was performed by simulating a 300 off-axis tension test and a static indentation test.

Technology Transfer

Cut Resistance of High Performance Fibers

Jessie B. Mayo, Jr.[1,2], Mahesh V. Hosur[1], Shaik Jeelani[1], and E. D. Wetzel[2*]

[1]Tuskgee Center for Advance Materials, Tuskegee University, Tuskegee, AL 36088

[2]U.S. Army Research Laboratory, Aberdeen Proving Ground, MD 21005

Abstract

I.   Introduction

Fibers are classified as organic (aramids, extended chain polyethylenes, aromatic polyester fibers, aromatic heterocyclic polymer fibers, etc.) and inorganic (carbon, glass, metals, carbides, oxides, etc.) and are used in several applications. These applications include but are not limited to automotive, sports, composites technology, and flexible body armor. The flexible body armor industry has utilitzed many types of fabrics woven from high performance fibers that show good resistance against ballistic threats. Some examples of fabrics that show good ballistic resistance are Kevlar, Twaron, Technora, PBO and Spectra. The fibers that make up these fabrics are elastic and have high tensile moduli (Duan et al., 2006).

Well known is the fact that most body armor technologies have sufficient resistance against ballistic threats but have less resistance against cut and puncture threats. Puncture refers to intrusion of a material by a pointed object such as an ice-pick or awl. The pointed object has a tendency to "window" or displace the fibers and yarns of the woven material so that the object can easily enter through the fabric. Cut/shear occurs when an instrument with a continuous cutting edge transversely fractures the yarns/fiber bundles causing immediate severance. Mayo et al. (2009) examined the cut resistance of neat and thermoplastic impregnated Kevlar. Mayo et al. found that heat pressing thermoplastic films into hydrophobic Kevlar 706 dramatically increased cut and puncture resistance of the woven fabric. Decker et al. (2007) increased the puncture resistance of Kevlar and other woven fabrics by impregnating the fabric with shear-thickening fluid. Erlich et al. (2003) examined the resistance of Zylon to sharp fragments by means of quasi-static penetration push testing. Anctil et al. used a regime of P1 knives, S1 knives, engineered spikes, and flechettes as characterization tools to examine woven fabric resistance. These woven fabrics included Kevlar, Twaron, Spectra, Dyneema and Zylon.

When the concern is the cut resistance of yarns or fiber bundles, there are notable works. Shin and Shockey (2003) developed a test for measuring the cut resistance of Zylon yarns. Such

a study was done in order to develop a test procedure that reliably and reproducibly measures the cutting resistance of yarns under tension-shear conditions. Further studies by Shin and Shockey would expand the study to Kevlar and Spectra (2006). A very limited amount of single fiber cut studies have been conducted. Knoff (2001) investigated the fiber transverse deformation work and cut performance of protective apparel.

Mechanical characterization of single fibers is a study that has been conducted by many. Hearle et al. (1969) studied the theory of tensile mechanics of staple fiber yarns. Liu et al. (2007) examined the tensile properties of electrospun multi-walled nanofibers. The dynamic tensile response of aged Zylon (PBO) was examined by Rhorer et al. (2007). Transverse compression testing was studied by Cheng et al. (2004) and Singletary (2000). Forster et al. (2006) examined the effect of bending on Zylon fibers. Very few mechanistic studies have been conducted on single fibers. Single fiber studies, which are more fundamental that fabric and yarn studies, are necessary to fortify and improve several types of materials.

The scope of the current study is to explore the relationship between fiber type on cut resistance and the implications for the design and performance of stab resistant body armor, to provide comprehension of how fiber structure influence cut behavior, and to understand on a fundamental level, the physics/mechanics of cut behavior.

II.   Experimental

The fibers that were examined are in Table 1.

Table 1. Fibers examined in cut resistance study.

Trade Name	Chemical Composition	Denier	Diameter	Strain to failure (%)	Density (g/cm^3)	Modulus (GPa)	Tensile Strength (GPa)
Kevlar 129	aramid	840	13	3.3	1.44	96	3.38
Twaron	aramid	840	9.46	3.3	1.44	96	3.38
Dyneema SK-76	UHMWPE	400	18.8	3.6	0.98	88	2.62
Zylon (PBO)	aromatic heterocyclic	500	12.3	3.5	1.54	180	5.8
Vectran	aromatic polyester	1500	23.5	3.3	1.41	75	3.2
Technora	aramid	1500	12.3	4.6	1.39	73	3.44
S2-glass	glass	2980	9.29	5.5	2.48	85	4.8
Carbon fiber	graphite	800	8	2	1.8	234	4.83

Kevlar and Twaron have identical molecular structures and scientific name (poly-paraphenylene terephthalamide). One major difference between the two high performance fibers is their diameter. The diameters of these fibers as observed by the author through scanning electron microscopy were 13.0 µm and 9.46 µm for Kevlar and Twaron, respectively.

These fibers were held in place with a specially designed fiber clamp that is shown in Fig. 1. The fiber clamp fixture has a rotary platform, angle indicator, and rubber clamps. The two rubber clamps on the fixture were 127 mm apart, which gave the fiber to be investigated a gage length of 127 mm. The fiber was clamped at one end and at a position of 127 mm at that end. A Celanese food processing blade (American Cutting Edge, Inc., Centerville, OH) was mounted in

the crosshead fixture of a 20 N load cell of an Instron 5500 (Grove City, PA) materials testing system.
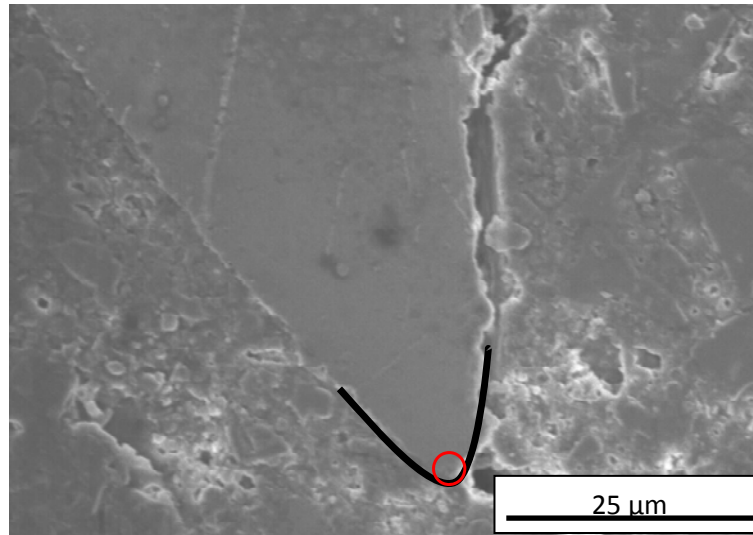

Figure 1. Scanning electron micrograph which show tip diameter (red circle) of Celanese blade.

The Celanese blade was used because of low error and data reproducibility. The blade has a tip radius of 14 μm. The blade cutting speed was maintained at 30 mm/min until the fiber was completely severed. Load vs. displacement curves were generated from the data obtained from the testing data.

The cut strain to failure was determined by using the Pythagorean theorem $x^2 + y^2 = r^2$.
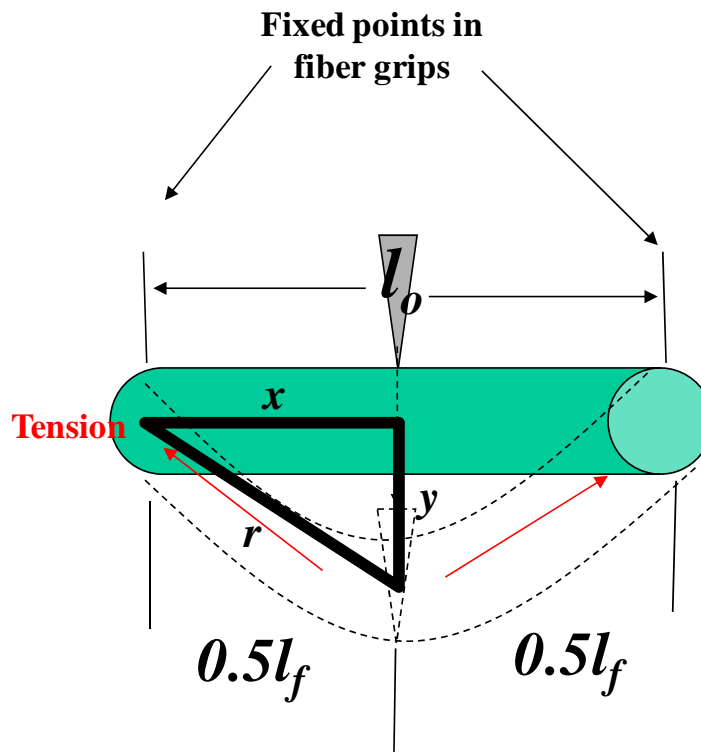
Here x is the half of the length of the fiber (63.5 mm), y is the extension or displacement of the fiber at failure, and r is the half length of the fiber at failure. Thusly, the formula used to determine the cut strain to failure is

$$\varepsilon_c = \frac{l_f - l_o}{l_f}.$$
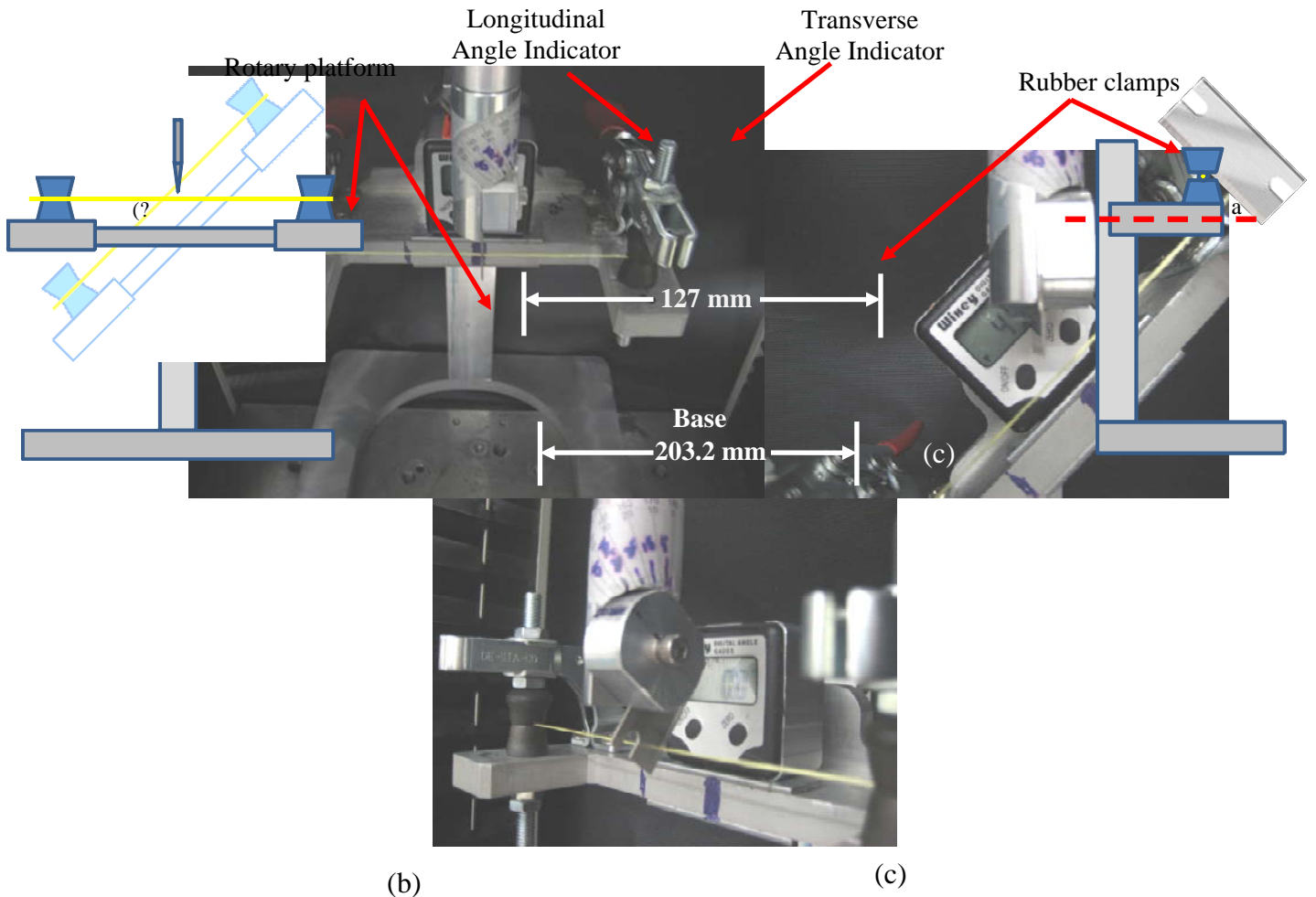
Figure 2. Photographs of (a) fiber clamp fixture showing normal incidence cut resistance testing, (b) longitudinal incidence, (c) transverse incidence, and (d) normal incidence cut resistance testing.

The effect of cutting angle on cut performance was evaluated through two arrangements; longitudinal (Fig. 2b) and transverse (Fig. 2c). The numbering convention θ-α was used to refer to the longitudinal-transverse cut angles for a given experiment. All fibers were cut at longitudinal angles and transverse angles varying from 0º to 45º in 5º increments. Longitudinal cut testing involved varying the angle of the fiber under investigation while keeping the blade at $\alpha = 0°$, and transverse cut testing involved varying the angle of blade while keeping the fiber at $\theta = 0°$. All of the fibers listed in table 1 were tested for cut resistance.

III.   Results

1. General behavior
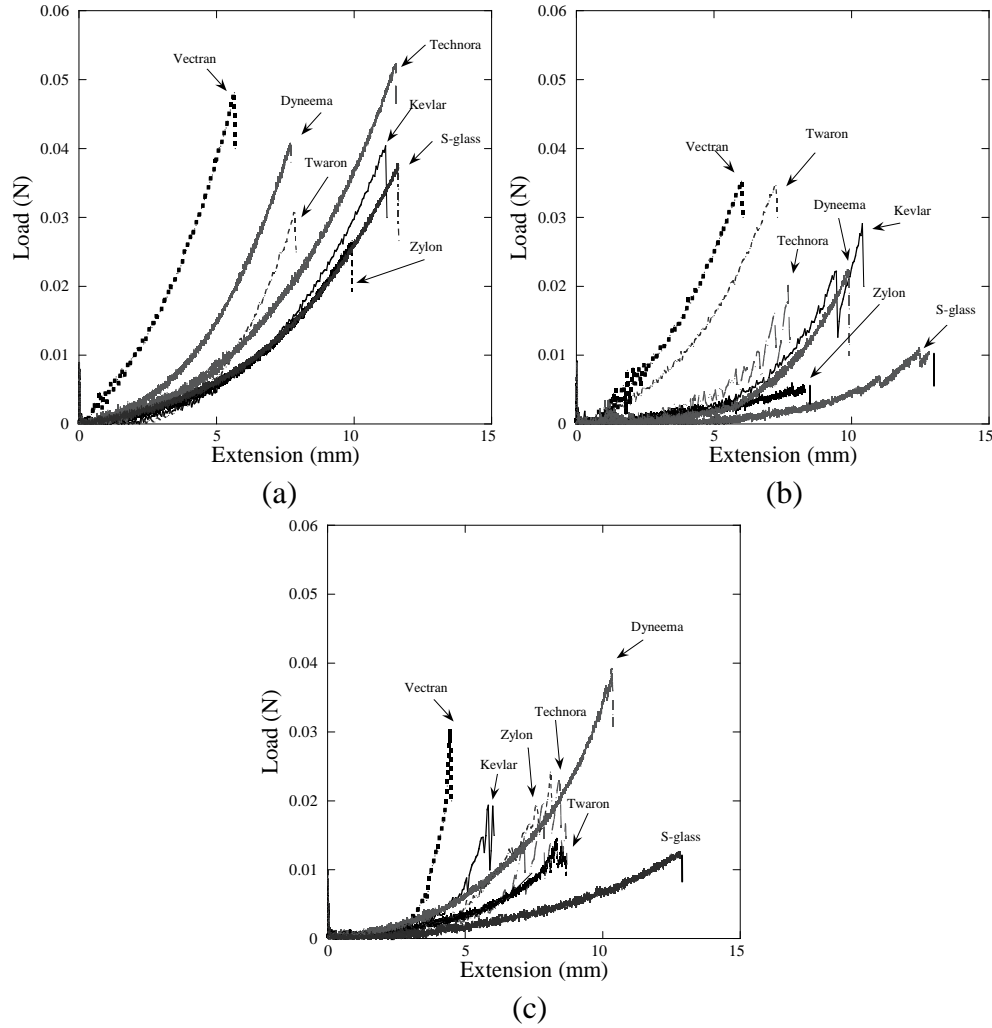
Figure 1. Force as a function of extension for high performance fibers cut at (a) normal incidence (0-0), (b) 45° longitudinal incidence (0-45) and, (c) 45° transverse incidence (45-0) by Celanese blade.

Figure 1a shows general behavior of high performance fibers during cut resistance testing at normal incidence with a Celanese food processing blade. This data is the raw data before diameter normalization. The raw data is given in Newtons (N) while extension is given in millimeters (mm). There is a gradual increase in load with extension/displacement for each fiber curve. The response drops to zero at failure. Without diameter normalization, Technora has highest cut resistance and Zylon has the lowest cut resistance.

Figure 1b shows the general behavior of high performance fibers during cut resistance testing at 45° longitudinal incidence with a Celanese food processing blade. At this fiber angle, Vectran has the highest cut resistance force with Twaron being very close in magnitude. Zylon has the lowest magnitude of all of the fibers tested. As the fiber angle changed from 0° to 45° the response of some of the fibers became more noisy.

Figure 1c shows the general behavior of high performance fibers during cut resistance testing at 45° transverse incidence with a Celanese food processing blade. At this blade angle, Dyneema has the highest cut resistance force and S-glass has the lowest cut resistance force.

2. Size effects and scaling

(a)   (b)
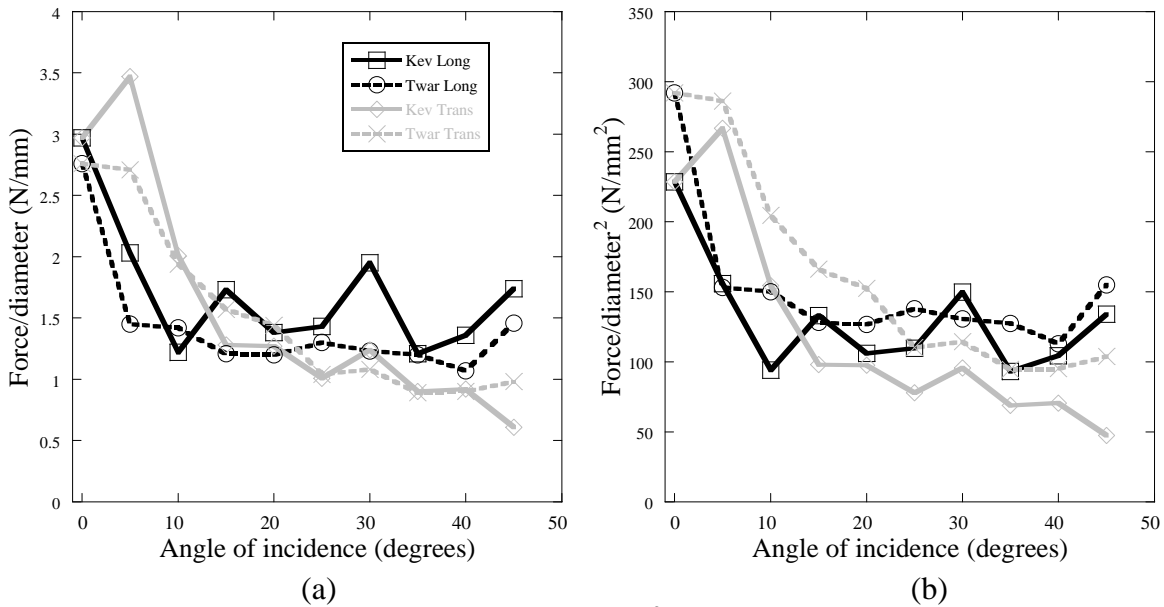
Figure 3. (a) Force/diameter and (b) force/diameter^2 as a function of angle of incidence for Kevlar and Twaron fiber cut with Celanese blade.

This section compares Kevlar and Twaron. In this section, the reasons for the force/diameter designation are discussed. It is most reasonable to normalize by the fiber diameter instead of diameter^2 because it is envisioned that the blade-fiber contact was a line contact rather than a cross-sectional area loading. Alternatively, one could choose to normalize the cutting force by the fiber cross-sectional area, proportional to fiber diameter squared. To begin, once the Kevlar and Twaron cut resistance data is normalized by either the diameter or diameter^2; the plots with the closest comparable data will determine the correct normalization scheme.

Figure 3a and 3b show the force/diameter and force/diameter^2 as a function of angle of incidence for Kevlar and Twaron. The plots contain both longitudinal and transverse cut resistance results. There is a greater amount of overlap with force/diameter plot than with force/diameter^2 plot. F/d is chosen for normalization of the fibers.
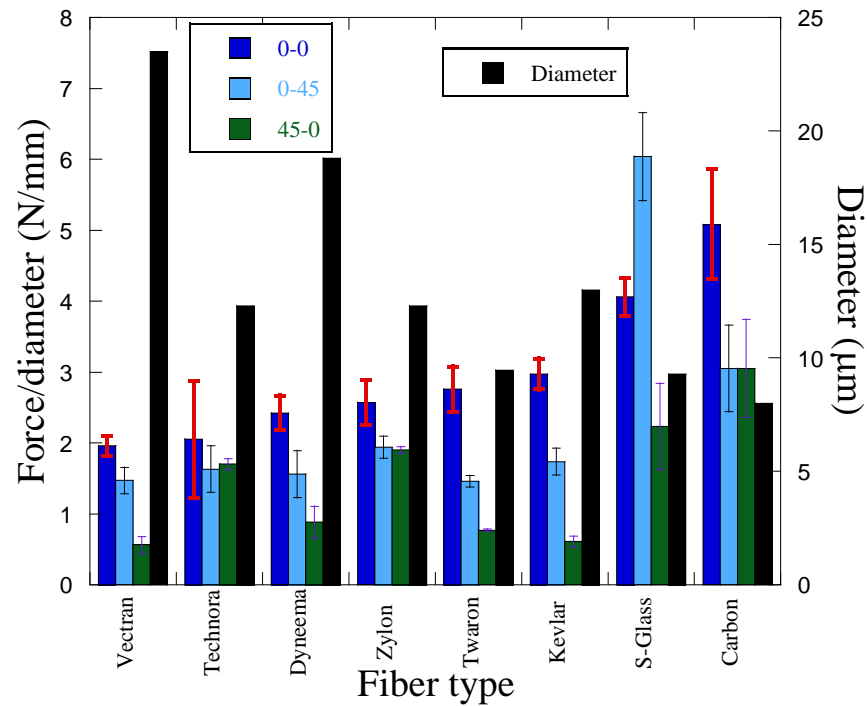
Figure 4. Force/diameter and diameter as a function of fiber type for all fibers tested for cut resistance at 0-0, 0-45, and 45-0.

Figure 4 is a plot of the force/diameter (left y-axis) and diameter (right y-axis) as a function of fiber type for all of the fibers that were tested for cut resistance. Fibers are listed with respect to magnitude of cut resistance at 0-0 from lowest to highest cut resistance. At 0-0 Vectran, the fiber with the largest diameter, has the lowest cut resistance. The reader must keep in mind that the diameter is a characterization tool because diameter effects have been discarded because of normalization. At 0-0 carbon fiber has the highest cut resistance. The two inorganic fibers are among the highest cut resistance cases. As the testing goes from 0-0 to 0-45 to 45-0, Vectran, Zylon, Twaron, Kevlar, and carbon fiber cut resistance decreases as the angle changes. S-glass is the only fiber where the 0-45 test is higher than 0-0 and 45-0.
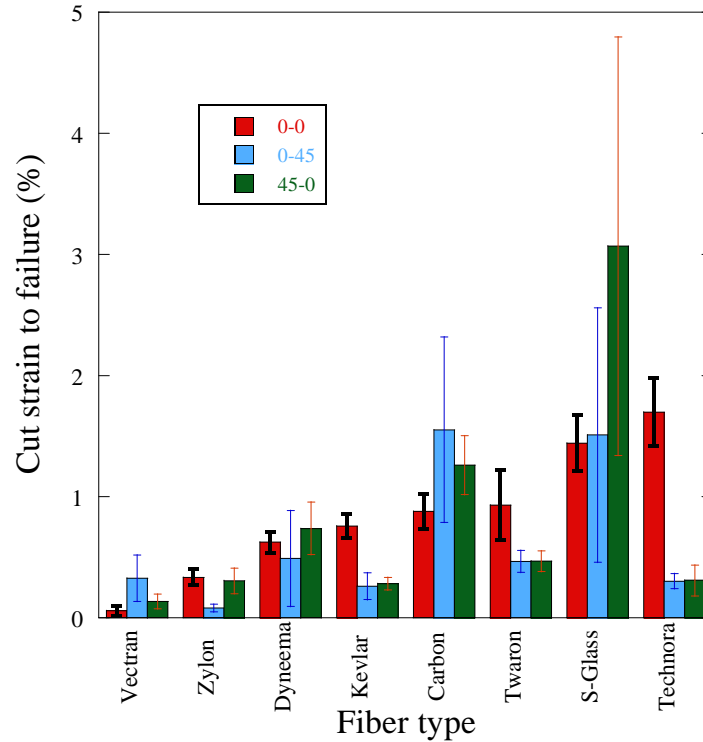
Figure 5. Cut strain to failure as a function of fiber type for all fibers tested for cut resistance at normal incidence, 45° longitudinal degrees, and 45° transverse degrees.

3. Cut Strain to Failure Results

Figure 5 shows the cut strain to failure as a function of fiber type of the fibers examined in the cut resistance study. At normal incidence (0-0), Vectran had the lowest cut strain to failure while Technora has the highest. At 45 longitudinal degrees (0-45), Zylon had the lowest cut strain to failure while Carbon had the highest cut strain to failure. At 45 transverse degrees (45-0), Vectran had the lowest cut strain to failure while S-glass had the highest. Errorwise, S-glass had significant errors for angled testing.

4. Organic fiber results

In general, as the fiber angle increased, the organic fibers cut resistance decreased in the lower angles but began to level out for the duration of the testing. As the blade angle increased, the organic fibers cut resistance decreased. On average, considering all angles tested; Zylon had the highest cut resistance and Vectran had the lowest out of the organic fibers. Vectran and Technora average cut resistances were very close in magnitude with Kevlar cut resistance not far behind. Twaron had the lowest cut resistance of the tested organic fibers.

Table 2. Summary of average force/diameter (N/mm) of longitudinal cut resistance testing.

Fiber	0-0	0-5	0-10	0-15	0-20	0-25	0-30	0-35	0-40	0-45	Average
Kevlar	2.97	2.03	1.22	1.73	1.38	1.43	1.95	1.21	1.36	1.74	1.70
Twaron	2.76	1.45	1.42	1.21	1.20	1.30	1.23	1.20	1.07	1.46	1.43

Dyneema	2.42	2.04	1.98	1.43	1.46	1.61	1.00	1.20	1.43	1.56	1.61
Zylon	2.57	2.05	1.80	1.44	1.57	1.40	1.25	1.48	1.15	1.94	1.67
Vectran	1.96	1.80	1.87	1.32	1.75	2.02	1.56	1.66	1.75	1.47	1.72
Technora	6.67	1.61	1.27	1.31	1.31	1.38	1.58	1.79	1.23	1.63	1.98
S-glass	4.06	4.11	2.41	3.75	4.22	4.69	3.82	4.92	5.82	6.04	4.38
Carbon	5.08	5.26	5.68	7.29	5.88	5.76	4.34	4.52	5.61	3.05	5.25

Table 3. Summary of average force/diameter (N/mm) results of transverse cut resistance testing.

Fiber	0-0	0-5	0-10	15-0	20-0	25-0	30-0	35-0	40-0	45-0	Average
Kevlar	2.97	3.47	2.01	1.28	1.27	1.01	1.24	0.9	0.92	0.61	1.568
Twaron	2.76	2.13	1.53	1.24	1.14	0.82	0.85	0.7	0.71	0.77	1.265
Dyneema	2.27	0.96	1.14	1.73	0.73	1.04	0.6	0.81	0.64	1.8	1.172
Zylon	3.52	2.96	2.33	1.65	1.1	1.33	0.86	0.86	0.55	1.9	1.706
Vectran	1.96	2.93	1.52	1.52	1.38	1.18	0.63	0.94	0.65	0.56	1.331
Technora	4.13	2.73	2.22	1.74	1.23	1.37	1.25	0.79	0.9	1.7	1.806
S-glass	4.19	4.1	3.61	4.04	3.73	5.09	3.5	2.9	2.13	2.23	3.552
Carbon	5.08	5.26	5.68	7.29	5.88	5.76	4.34	4.52	5.61	3.05	5.247

5. Inorganic fiber results

At normal incidence Carbon had a higher cut resistance that S-glass. Generally, as the longitudinal angle of incidence increased, the cut resistance of the S-glass increased while the carbon fiber decreased only slightly. As the transverse angle of incidence increased, the cut resistance of the inorganic fibers decreased. S-glass has higher cut resistance than carbon fiber at 0-45. Carbon has higher cut resistances than s-glass at 0-0 and 45-0. Carbon had higher standard deviation and more random response to cut resistance testing. Being that no microscopic techniques were used, it was unclear as if single fibers of carbon were being tested as opposed to multiple fibers.

6. Microscopy of failed fibers

Scanning electron microscopy was done with a Hitachi S-4700 (Chiyoda, Tokyo, Japan) field emission scanning electron microscope. The accelerating voltage used for the scanning electron micrographs (SEMs) was 20 KV. The working distance between the detector and the fiber was between 12 and 20 mm. The fibers, after cut testing, were sputtered with a few nanometers of platinum by a Hummer XP (Alexandria, VA) sputter machine.
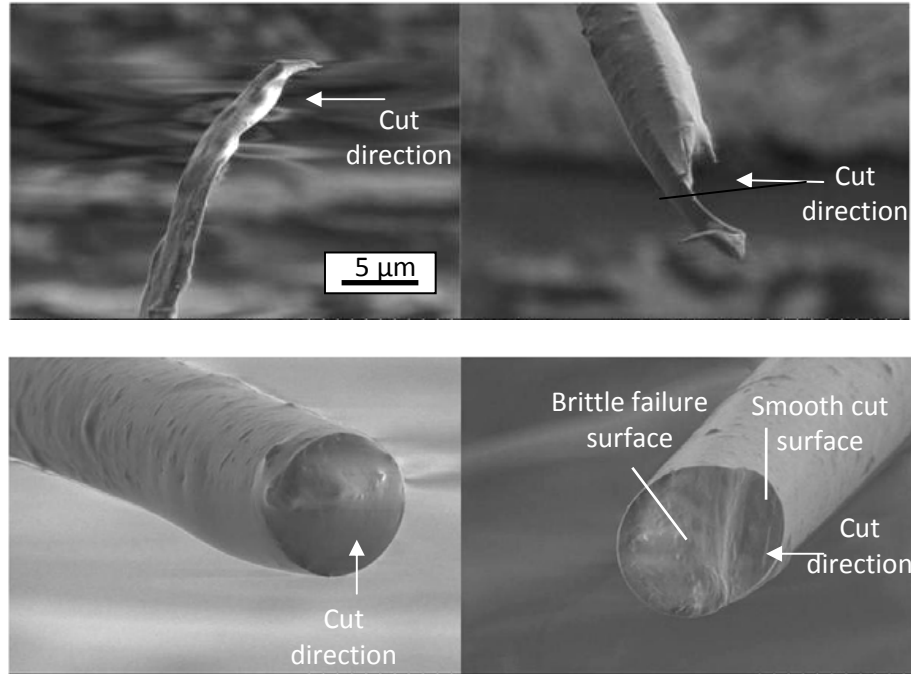
Figure 7. SEMs of (top) Kevlar and (bottom) S-glass fibers after cut resistance testing at normal incidence.

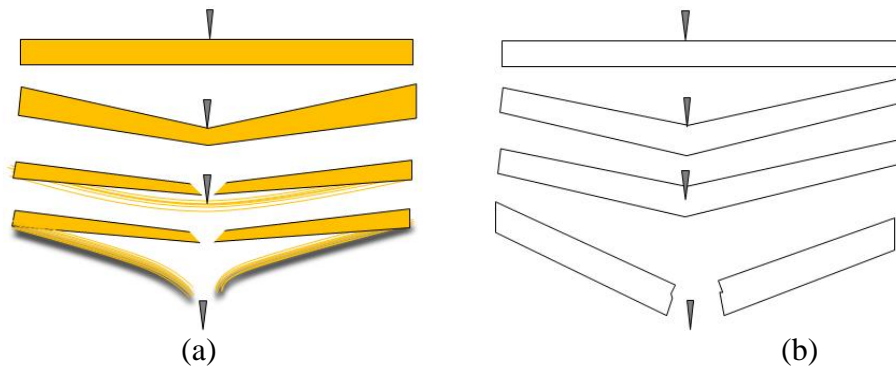(a)   (b)

Figure 8. Schematics of failure dynamics and responses of (a) Kevlar and (b) S-glass fibers during cut resistance testing.

Figure 7 shows the SEMs of the surface damage of the Kevlar and S-glass fibers after cut resistance testing. Figure 8 is the failure progression inferred from the SEMs of the two fibers. The blade pressed into the Kevlar deforming (crushing) the fiber at the point of incident. The blade cut between halfway to three quarter through the fiber until there is interfibril splitting created by the fibrils of the Kevlar fiber. The fibrils are too strong to be cut to because of increasing transverse compression, the fibrils finally give way due to tension instead of cutting. The blade pressed into the S-glass but no deformation could be observed. Instead, the blade pressed a dent into the S-glass and with increasing transverse compression, the S-glass fiber broke with brittle failure. With S-glass, a smooth cut surface is seen where the blade enters into the fiber. A rough, brittle fracture zone is seen where the S-glass fiber breaks because of tension.
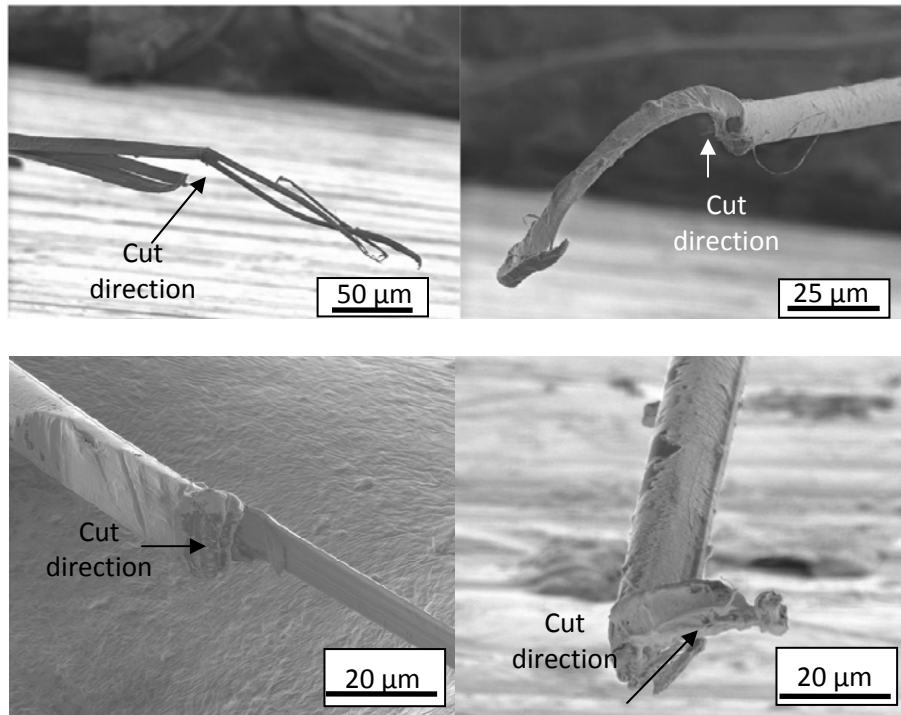
Figure 9. SEMs of (top) Kevlar after 45° longitudinal incidence cut resistance testing (0-45) and (bottom) Kevlar after cut resistance testing at 45° transverse incidence (45-0).

(a)   (b)
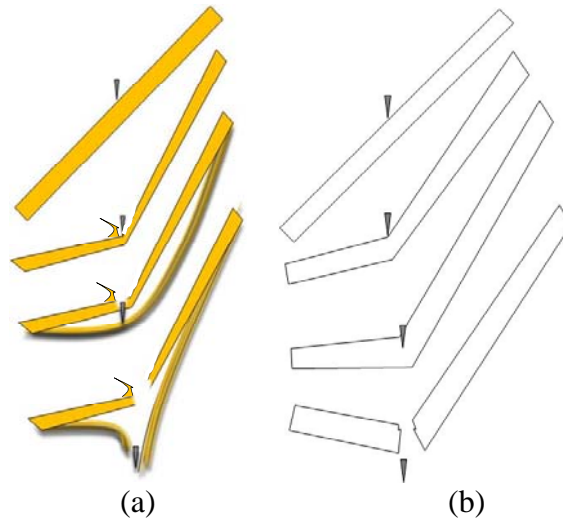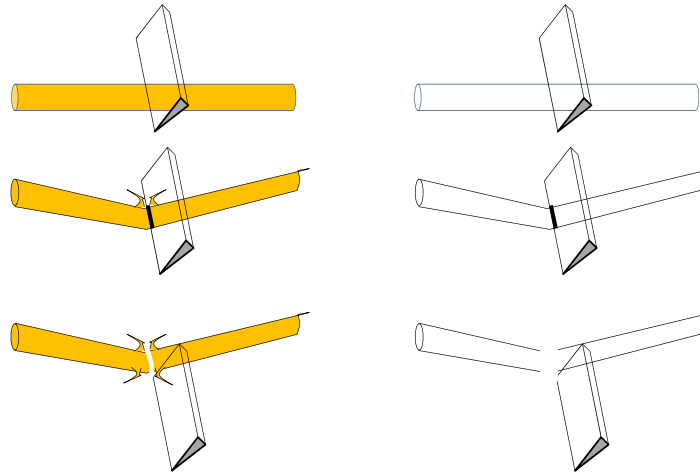
Figure 10. Schematic of failure dynamics and cut response of (a) Kevlar and (b) S-glass fibers after 45° longitudinal cut testing (0-45).

Figures 9 shows the SEMs of the damaged areas of the tested fibers and Fig. 10 shows the damage progression of the Kevlar and S-glass fibers at 45° longitudinal cut resistance testing. The blade shears away a layer of the Kevlar shell as it moves down the 45° fiber. The blade then

encompasses a fibril bundle that has to be broken through with tension. This is easily accomplished because of the new reduced cross-sectional area left after the shearing away of the Kevlar layer. More branching of the fibrils are seen in the SEMs of the damaged Kevlar at 45°. With S-glass, the blade makes a similar indentation into the fiber as with normal incidence. There is not much deformation, if any, due to transverse compression. The fiber breaks with brittle failure.

Figure 11. Schematic of failure dynamics and cut response of (a) Kevlar and (b) S-glass fibers after 45° transverse cut testing (45-0).

Figure 11 is the damage progression of the Kevlar and S-glass fiber during 45° transverse cut resistance testing. With Kevlar, the blade shears away material on both sides of the blade as the fiber is being cut. The fiber actually moves up the blade, which creates extra shear. At the conclusion of testing, the outer circumferential layer of the Kevlar fiber has been sheared away (as seen in the SEM). With S-glass, there is no shearing of layers. The blade simply cuts through the S-glass fiber.

IV.   Discussion

There is a good amount of deformation seen in ductile (organic fibers). There is very little deformation seen in brittle (inorganic fibers). We see shearing of ductile shell. There is no sort of fiber shearing for brittle fiber. There are well defined brittle and smooth cut surfaces for brittle fiber but no well defined cut surfaces for ductile fiber.

Because of processing parameters, the outer circumference of the Kevlar fiber is hard and crystalline. The regions become more amorphous and softer as the regions come closer to the center. Hard structures call fibrils that have diameters around 30-50 nm exist in the outer shell of the Kevlar fiber (Singletary, 2000). S-glass is a completely amorphous and isotropic fiber. S-glass fiber has a higher hardness than Kevlar fiber. Maximum cut resistance occurs at Kevlar surface. Cut resistance is highest at normal incidence because blade has to break through hard fibril circumference. As angle increases, the circumference is sheared away instead of broken through (less force for shearing away). This explains the pattern for ductile/organic fiber cut

resistance. With S-glass, the pattern rises instead of decreases. As the angle increases for S-glass, the blade has to go through more material. In turn, this creates a higher cut resistance.
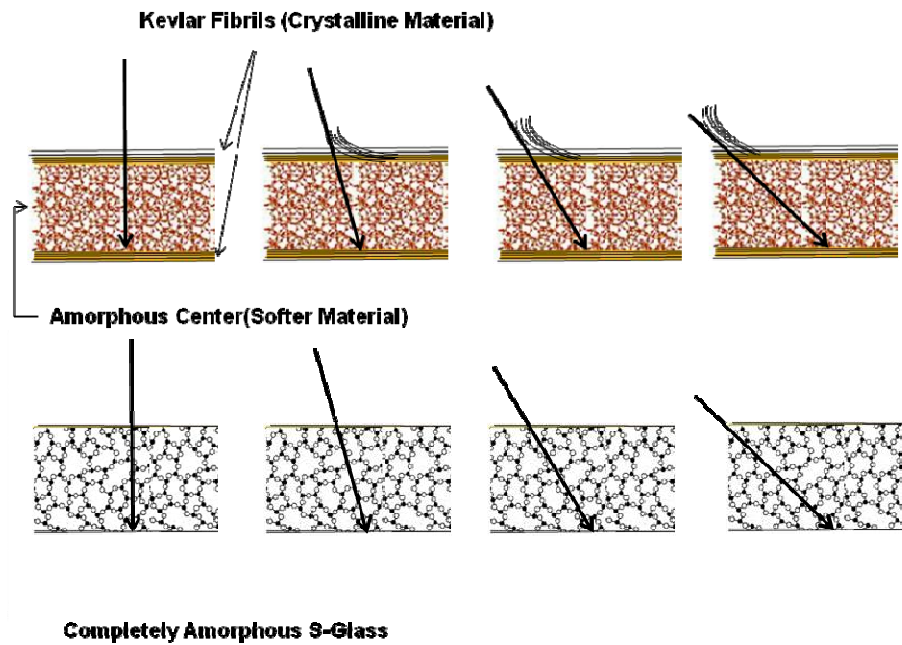

Figure 12. Model used to explain cut resistance of organic and inorganic fibers.

Fiber structure and fiber hardness are the material properties predict cut resistance
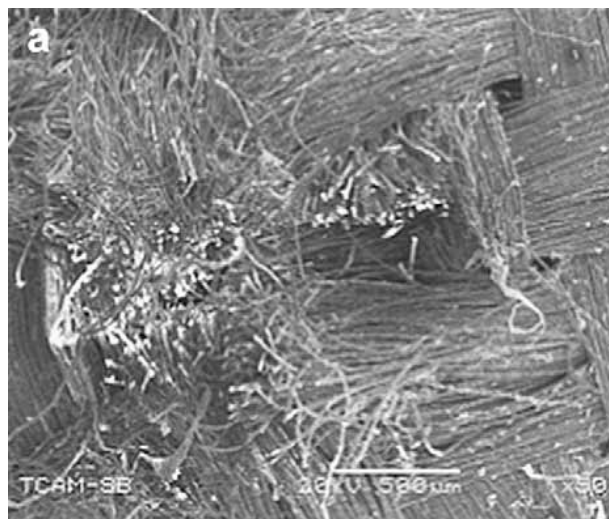
V.   Conclusions

Figure XX. Kevlar fabric that has been tested for S2 knife resistance.

Single filaments of Kevlar fabric have similar damage of single Kevlar fibers (at normal incidence). S-glass has a higher denier, strain to failure, density, and tensile strength than Kevlar fiber. Kevlar has not proven to be an acceptable material for stab armor. From the cut resistance tests in this work, S-glass fiber would be a more acceptable material for stab armor. However, from these tests (single fiber cut resistance tests), we cannot conclude that S-glass would make a suitable material for stab armor. Stab armor has many other parameters that determines its stab resistance (i.e. weave tightness and fiber/mechanism friction, compactness of fabric layers, areal density, etc.). Therefore, actual stab resistance testing, would have to be performed on S-glass armor.

References

Cheng, M. and T. Weerasooriya. 2004. Experimental investigation of the transverse mechanical properties of a single Kevlar KM-2 fiber. *International Journal of Solids and Structures* 41: 6215-6232.

Decker, M.J., C. J. Halbach, C.H. Nam, N.J. Wagner, and E.D. Wetzel. 2007. Stab resistance of shear thickening fluid (STF)-treated fabrics. *Composite Science and Technology* 67 nos. 3-4: 565-579.

Duan, Y., M. Keefe, T. A. Bogetti, and B. Powers. 2006. Finite element modeling of transverse impact on a ballistic fabric. *International Journal of Mechanical Sciences* v48 pgs. 33-43.

Erlich, D. C., D. A. Shockey, and J. W. Simons. 2003. Slow Penetration of Ballistic Fabrics. *Textile Research Journal* 73 no. 2: 179-184.

Forster, A. L., J. W. Chin, and M. Gundlach. 2006. Effect of bending and mechanical damage on the physical properties of poly(p-phenylene-2,6-benzobisoxazole)(PBO) fiber. *Abstracts of Papers of the American Chemical Society*, v231: pg. 274.

Hearle, J. W. S., P. Grosberg, and S. Backer. 1969. Structural Mechanics of Fibers, Yarns, and Fabrics v1.

Knoff, W., August 7-9, 1992. The Effect of Moisture and Heat Treatment on the Lateral Compressive Properties of Poly(p-phenylene terephthalamide) Fibers. Basic Properties of Fibers and Fiber Assemblies, Performance and Design of New Fibrous Materials: *Proceedings of the 21st Textile Research Symposium*, Fuji Kyouiku Kenshusho (Fuji

Educational Training Center), Susono City, Shizuoka, Fibrous Materials Research Group, Kyoto University and The Textile Machinery Society of Japan.

Liu, Q., D. Tasis, M. Prato, and H. D. Wagner. 2007. Tensile Mechanics of Electrospun Multiwalled Nanotube/Poly(methyl methacrylate) Nanofibers. *Advanced Materials* v19 pgs. 1228-1233

Mayo, J., Eric D. Wetzel, Mahesh V. Hosur and Shaik Jeelani 2009. Stab and Puncture Characterization of Thermoplastic Impregnated Aramid Fabrics. <u>International Journal of Impact Engineering</u>.

Nascimento, E. M. and C. M. Lepeinski. 2006. Mechanical Properties of Optical Glass Fibers Damaged by Nanoindentation after Water Aging. Journal of Non-Crystalline Solids. 352 no. 32-35: 3556-3560.

Rhorer, R., J. Chin, A. Forster, W. Chen, B. Song, X. Nie. Aging Effects on the Dynamic Tensile Response of Fibers. An Official Contribution of the National Institute of Standards and Technology.

Shin, H. S., D. C. Erlich, and D. A. Shockey. 2003. Test for measuring cut resistance of yarns. *Journal of Materials Science* 38: 3603-3610.

Shin, H. S., D. C. Erlich, Simons, J. W., and D. A. Shockey. 2006. Cut Resistance of High Strength Yarns. *Textile Research Journal* 76 no. 8: 607-613.

Singletary, J., H. Davis, M. K. Ramasubramanian, W. Knoff, and M. Toney. 2000. The transverse compression of PPTA fibers: Part I: Single fiber transverse compression testing. *Journal of Materials Science*. 35 pgs. 573-581.

Walker, A., C. Nicol, and E. K. J. Chadwick. 2004. Evaluation of test regimes for stab-resistant body armor. *Proc. Instn. Mech. Engrs., Part L (Journal of Materials:Design and Applications)* 218 no. L4: 355-361.

Sonochemical synthesis and rheological properties of shear thickening silica dispersions

Tarig A. Hassan, Vijaya K. Rangari *, Shaik Jeelani

Materials Science and Engineering, Tuskegee University, Tuskegee, AL 36088, USA

ARTICLE INFO

ABSTRACT

A sonochemical method has been developed to synthesize shear thickening fluid. This shear thickening fluid (STF) is composed of hard silicon dioxide nanoparticles and polyethylene glycol (PEG) liquid polymer. The combination of flow-able and hard components at a particular composition, results a material with remarkable rheological properties that is suitable for liquid body armor applications. In the present study nine types of STF's have been synthesized with two different types of silica nanoparticles (15 nm and 200 nm) and polyethylene glycol at various weight fractions using a high intensity ultrasonic irradiation. The resultant STF samples were tested for their rheological and thermal properties. The advantages and disadvantages of this process have been discussed.

1. Introduction

Shear thickening is a non-Newtonian flow behavior and defined in the British Standard Rheological Nomenclature as the increase of viscosity with increase in shear rate. This is distinguished from rheopexy which is defined as the increase of viscosity with time while the shear rate in constant [1]. Dilatancy is another term used to describe shear thickening, however, it has been avoided since it usually implies an increase in the volume on deformation, which is not considered in this case [2]. The shear thickening trend can take place in concentrated colloidal suspensions that have been shown to exhibit reversible shear thickening resulting in large, sometimes discontinuous, increases in viscosity above a critical shear rate. In order to explain this behavior, two theories of shear thickening phenomenon were reported: the order–disorder transition [3–7] and the "hydrocluster" mechanism [8–13]. This transition from a flowing liquid to a solid-like material occurs due to the formation and percolation of shear induced transient aggregates, or "hydroclusters", that dramatically increase the viscosity of the fluid. Rheological, rheo-optics and flow-SANS experiments have been demonstrated in support of the hydrocluster mechanism of shear thickening phenomenon [14,15] in addition to computer simulations [16]. It was reported in the literature that shear thickening has been observed for a wide variety of suspensions such as clay–water [17], calcium carbonate–water [18], polystyrene spheres in silicon oil [19], iron particles in carbon tetrachloride

[20], titanium dioxide-resin [21], silica-poly propylene glycol [22] and silica-ethylene glycol [23].

Many researchers have reported the synthesis of materials that show shear thickening behavior. Raghavan and Khan stated that suspensions of fumed silica in polypropylene glycol exhibit shear thickening under steady shear and "strain-thickening" under oscillatory shear. He also explained the combination of shear and strain thickening behavior through a clustering mechanism which attributes the thickening phenomena to the presence of temporary, flow-induced clusters. These clusters are being generated by the action of hydrodynamic forces on silica aggregates [22]. Each suspension was made in 60 ml batch by adding the liquid polymer to ~14 nm spherical silica particles and mixed in a blender for approximately 1 min and placed under vacuum for 12 h to get rid of air bubbles. The samples concentrations were varied from 3% to 10% weight basis.

Lately Lee et al. [23] reported the applications of STF in liquid body armor fabrication. They also studied the ballistic impact characteristics of Kevlar woven fabrics impregnated with a colloidal shear thickening fluid. The STF was prepared from 466 nm spherical colloidal silica particles and ethylene glycol. The synthesis procedure started with 3 h of centrifugation for the colloidal solution at 3900 rpm to separate the silica particles from the aqueous-based supernatant. The silica sediment was then crushed using a spatula and re-suspended in ethylene glycol using a vortex mixer. This process was repeated four times in order to minimize the amount of residual aqueous supernatant present within the samples. Ballistic impact results of Kevlar fabrics impregnated with this STF sample showed significant enhancements in ballistic penetration resistance of the STF impregnated fabrics compared to neat Kevlar due to the addition of STF without any loss in material

---

* Corresponding author. Tel.: +1 334 724 4875; fax: +1 334 724 4224.
E-mail address: rangariv@tuskegee.edu (V.K. Rangari).

flexibility. They have also prepared the STF from solvent exchange method. In this method colloidal silica was heated to evaporate water from colloidal solution and the evaporated amount of water was replaced with an equivalent amount of ethylene glycol. This process continued until all the water was replaced with 57% or 62% of ethylene glycol by volume. The rheological measurements of these samples also showed a shear thickening behavior [24,25].

Recently high-power ultrasound irradiation has been extensively used in the dispersion of nanoparticles in liquids [26,27] and it is also considered as one of the efficient techniques to disperse nanoparticles into materials [28,29]. Intense ultrasound waves traveling in liquids generate growing cavities. When the cavity attains a critical size it implodes, generating extreme conditions of intense heat and tremendous pressure that provide an unusual chemical environment for chemical reactions. The formation, growth, and implosive collapse of bubbles in a liquid irradiated with ultrasound are the physical phenomenon responsible for most of the sonochemistry. Ultrasound is produced in liquids by means of piezoelectric or magnetostrictive materials: materials that expand or contract when they are placed in electromagnetic fields. Exposing such materials to a field alternating at an ultrasonic frequency produces ultrasound [30–34].

In the present investigation, we have used a high intensity ultrasonic irradiation technique for synthesis of STF. PEG is used as suspending liquid phase because of its non-toxicity, thermal stability, easy to handle and easily available in bulk quantities which make it useful for bulk production. In this technique we have also used ethanol as a solvent because its sonochemical effects have been well studied [35,36] and also it is used as a solvent in the impregnation process of STF on Kevlar and nylon fabric for body armor applications.

2. Experimental work

2.1. Materials

Colloidal silica and dry powder silica nanoparticles have been used for this study. The dry powder silica nanoparticles are spherical in shape and ∼15 nm in size. These nanoparticles were purchased from Nanostructured and Amorphous Materials, Inc., Los Alamos, NM. The 200 nm spherical colloidal silica solution (MP-1040 40% concentration of silica nanoparticles) was purchased from Nissan Chemicals, Japan. PEG-200 and ethyl alcohol were purchased from Sigma–Aldrich Chemicals, St. Louis, MO.

2.2. Synthesis of shear thickening fluid

Different STF samples were prepared using different weight fraction of silica nanoparticles in PEG/ethanol by sonochemical technique. Known weight percentages of PEG and silica nanoparticles (dry powder or colloidal silica solution) were mixed in an excess amount of ethanol (40:60 STF:ethanol ratio was used) (one and half times more than STF) for colloidal silica solution no ethanol was used. The reaction mixture was irradiated with high intensity ultrasonic horn (Ti-horn, 20 kHz, 100 W/cm^2 at 50% amplitude) for 5 h and the reaction temperature was maintained using a chiller at 10 °C. The solvent (water or ethanol) was later removed from the reaction mixture via an evaporation process by heating at about 100 °C. The concentrations of as-prepared STF samples (sample (A)–sample(I)) are presented in Table 1.

For comparison purposes STF sample (I) was synthesized using mechanical mixing method.

In this method a known weight percentage of silica powder and PEG were mixed for 10 min at room temperature using a THINKY hybrid mixer ARE-250.

2.3. Characterization

2.3.1. Rheological measurements

Rheological studies were performed for all as-prepared STF samples to investigate the effect of shear rate increase on the viscosity. These tests were carried out using a TA Instrument Rheometer-AR2000 at room temperature, 0 °C and 40 °C. All the test were carried out using a peltier plate and a cone plate of size 40 mm and 2° angles in a steady state flow mode and shear ramp rate of 0–125 s^{-1}.

2.3.2. Thermal analysis

Thermogravimetric analyses (TGA) experiments were conducted to estimate the weight ratios of silica and polyethylene glycol in as-prepared STF samples. TGA samples were prepared by adding a few drops of as-prepared STF samples (10–20 mg) to a known weight of alumina crucible. TGA experiments were carried out using a Mettler Toledo TGA/SDTA 851 from room temperature to 800 °C at heating rate of 5 °C/min under nitrogen atmosphere.

2.3.3. Scanning electron microscopy (SEM)

SEM studies were carried out using a JEOL JSM 5800 scanning electron microscope. The SEM samples were prepared by uniformly spreading the as-prepared STF samples on a double-sided carbon tape and coated with gold/palladium to prevent charge buildup by the electron absorption.

2.3.4. Transmission electron microscopy (TEM)

TEM investigation of as-received silica nanopowder and colloidal silica nanoparticles were carried out using a JOEL-2010 microscope. TEM samples were prepared by dispersion of nanoparticles in ethanol and a drop of solution was placed on a copper grid (carbon coated copper grid-200 mesh) then dried in air and used for TEM analysis.
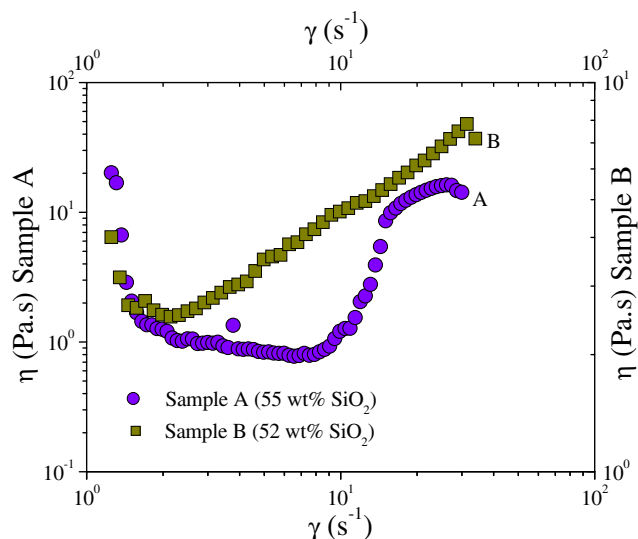
3. Results and discussion

The rheological properties of as-prepared STF samples were studied to understand shear thickening or shear thinning behavior rate at room temperature. Fig. 1A shows the viscosity of STF sample (A) as a function of the shear rate. STF sample (A) demonstrates shear thickening behavior in the range of 10–30/s shear rate and the sample viscosity increases from ∼2 Pa s to ∼17 Pa s. Fig. 1B (sample B), with a lower concentration of silica nanoparticles (52 wt%), shows a shear thickening effect in the range of ∼2–40/s shear rate and with increase in the viscosity from 2.5 Pa s to 8 Pa s before a reversible trend is seen. The rheological properties of STF samples (sample (A) and sample(B)) indicate that the increase of the weight fraction of the suspending phase (PEG) in the sample gives better shear thickening fluid as the samples become more viscous. Fig. 2C shows the rheological graph of sample (C) where the silica weight fraction was decreased to 42 wt % and the weight fraction of PEG was increased to 58 wt%. This Fig. 2C shows a significant shear thickening behavior with an increase in the viscosity from ∼10 Pa s to ∼270 Pa s between 7 and 20/s shear rates. The increased value of viscosity indicates that the sample exhibits an incredibly high shear thickening effect. Sample (D) contains a relatively larger amount of PEG (60 wt%) and shows a shear thickening behavior. These results are presented in Fig. 2D and the viscosity changes from ∼20 Pa s at 5/s shear rate to 410 Pa s at 12/s shear rate before a reversal trend is seen. Shear rate values for shear thickening transitions are lower than the results reported in similar studies [23]. These results clearly show that the sonochemical mixing before evaporation significantly improves the shear thickening effect. The rheological graph of STF sample (E)

Table 1
As-prepared STF samples.

No.	Synthesis technique	Sample	SiO$_2$ particles size (nm)	SiO$_2$ weight fraction (%)	PEG weight fraction (%)
1	Sonochemical method	A	15	55	45
2		B	15	52	48
3		C	15	42	58
4		D	15	40	60
5		E	15	38	62
6		F	200	52	48
7		G	200	48	52
8		H	200	40	60
9	Mechanical mixing method	I	15	40	60

Fig. 1. Rheology graph of STF Sample A and STF Sample B.
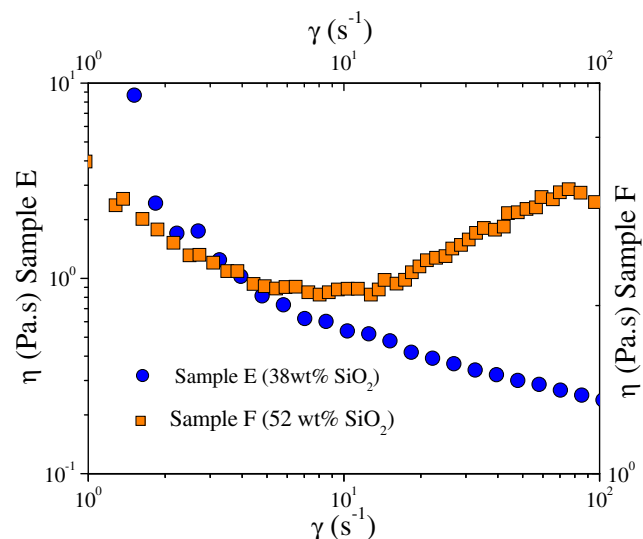
Fig. 3. Rheology graph of STF Sample E and STF Sample F.
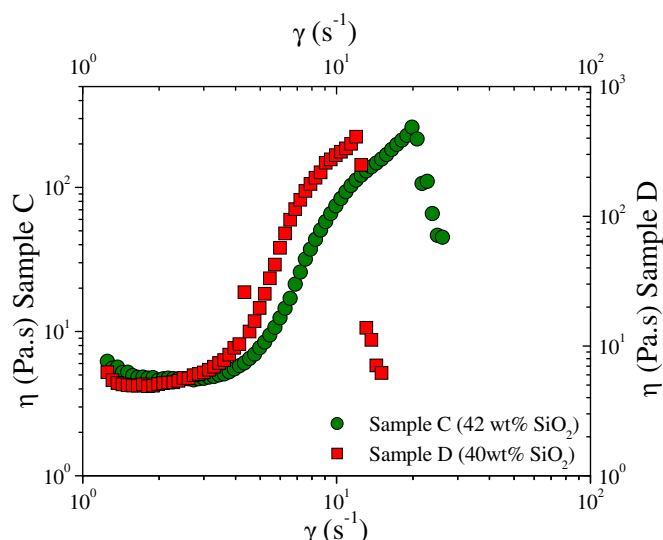
Fig. 2. Rheology graph of STF Sample C and STF Sample D.

is presented in Fig. 3E, and the STF sample (E) contains 62 wt% of PEG and 38 wt% of silica nanopowder. The rheological graph shows that the sample did not exhibit any shear thickening effect, instead, shear thinning behavior is noticeable at shear rate range of ~2–20/s. Among all as-prepared samples, sample (D) shows the best rheological properties. These results suggest that the optimal loading of silica nanoparticles (15 nm) by sonochemical method is 40 wt%.

To study the effect of particles sizes in preparation of STF, a colloidal silica solution (spherical 200 nm) was also used as a source of silica nanoparticles. The sample (F) was prepared using a 52 wt% of silica (200 nm) and 48 wt% of PEG and the rheological graph is presented in Fig. 3F. As seen in the graph the sample viscosity changed from 2 Pa s to around 3.3 Pa s, which is also very low compared to other samples. STF sample (G) contains 48 wt% silica and 52 wt% of PEG and the rheological graph is presented in Fig. 4G. Fig. 4G shows that the sample demonstrates a shear thinning behavior before it starts to exhibit a shear thickening behavior. The viscosity of the sample (G) increases from 4.5 Pa s to 7.5 Pa s, however the shear thickening effect is minimum. STF sample (H) was prepared from 40wt % of silica and 60wt % of PEG. Rheological test results for STF sample (H) are shown in Fig. 4H and it clearly shows the signature of the shear thickening effect and viscosity changes from 2.5 Pa s at shear rate of 3/s to 17 Pa s at about 18.5/s shear rate before a reversal trend is seen. The rheological properties for STF samples (sample (F), sample (G) and sample (H)) confirm that the optimum weight fraction of colloidal silica nanoparticles is 40% to demonstrate better shear thickening behavior. The sudden increase in the viscosity of as-prepared silica dispersions and the shear thickening transition are due to microstructural changes in the fluid along with the hydrocluster mechanism where the formation of particles clusters increases the hydrodynamic stress in the shear thickening fluid that leads to the dramatic increase in the viscosity. From the rheological graphs discussed previously, it is clear that the as-prepared STF samples containing 40 wt% of silica and 60 wt% of PEG shown enhanced shear thickening effect.
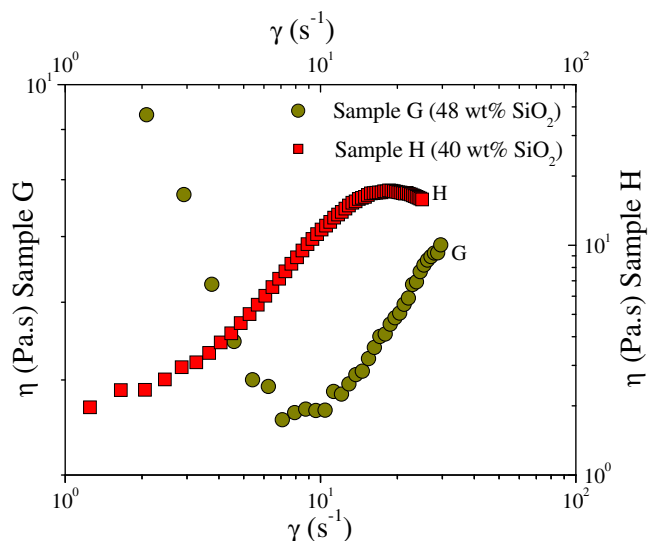
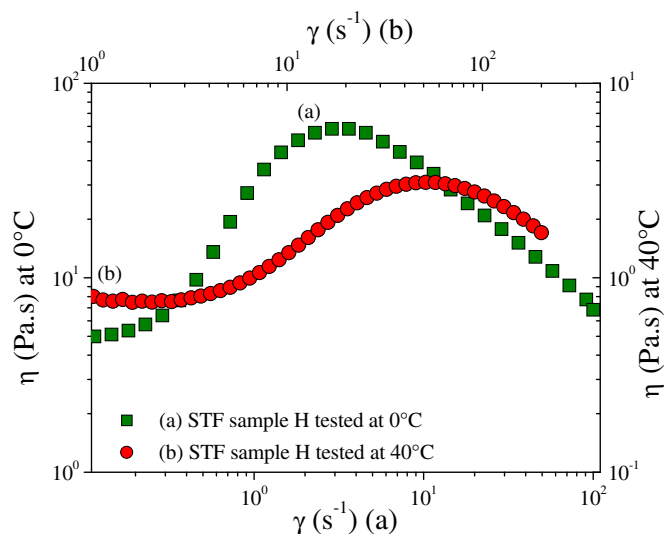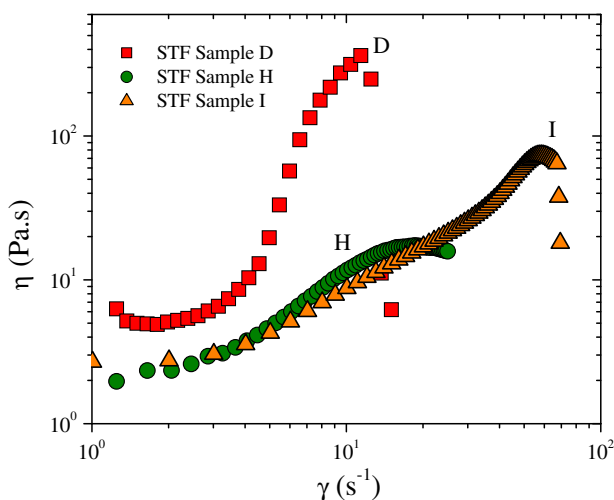**Fig. 4.** Rheology graph of STF Sample G and STF Sample H.

Fig. 5. Rheology graph of STF Samples D, H and I.

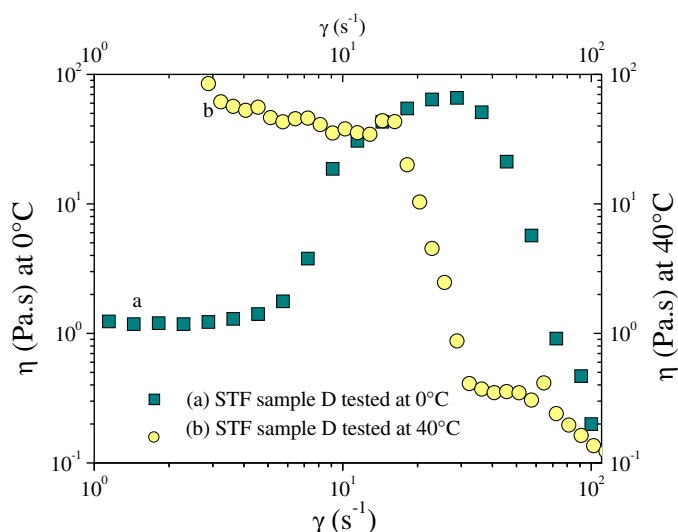**Fig. 6.** Rheology graph of STF sample D tested at (a) 0 °C and (b) 40 °C.

Fig. 7. Rheology graph of STF sample H tested at (a) 0 °C and (b) 40 °C.
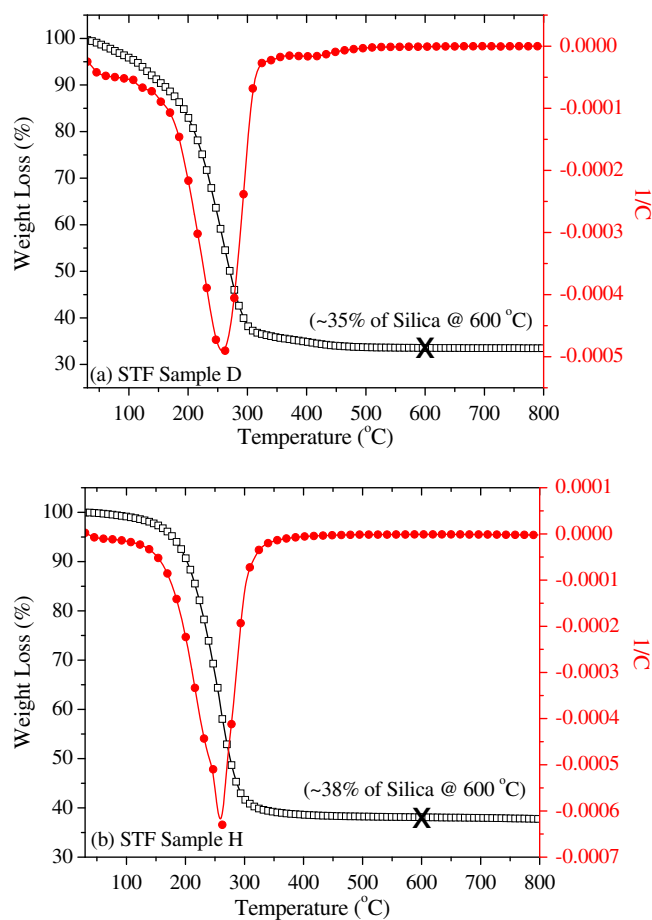

Fig. 8. TGA graphs for (a) STF sample D and (b) STF Sample H.

STF sample (I) was prepared using the same weight fractions (40 wt% of dry silica nanoparticles and 60 wt% of PEG) as in case of sample (D) and sample (H) for comparison purpose. The sample (I) is prepared using a simple mixing for 10 min instead of ultrasonic irradiation. The as-prepared homogeneous fluid was characterized for its rheological properties and shown in Fig. 5I. These results show a shear thickening behavior at shear rate range of 2–79/s with an increase in the viscosity from ~1 Pa s to ~57 Pa s.
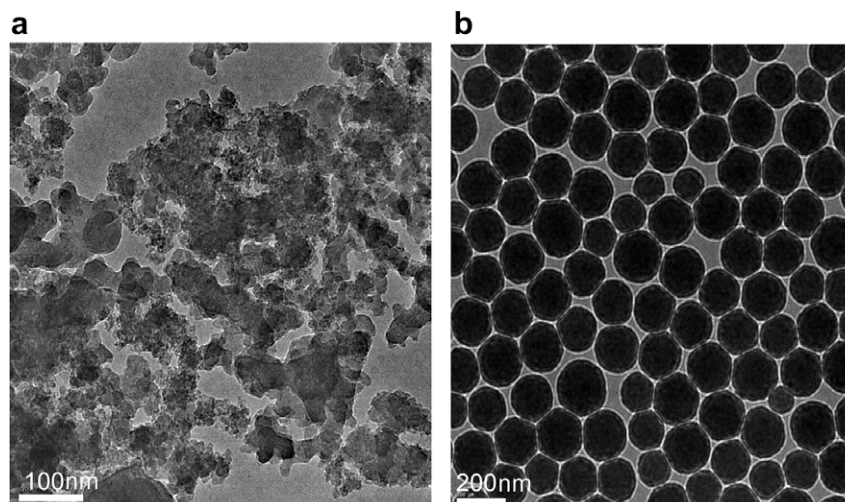
Fig. 9. TEM micrographs for (a) Silica nanoparticles (b) colloidal silica solution.
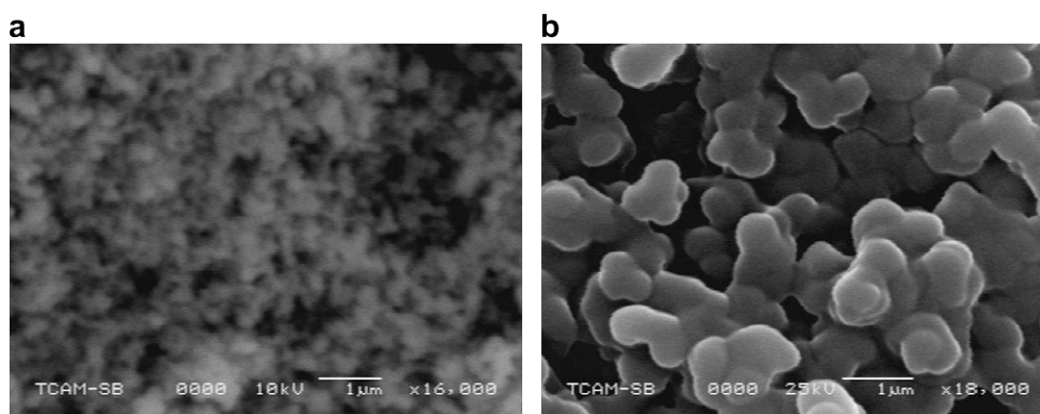
Fig. 10. SEM micrographs for (a) STF sample D and (b) STF Sample H.

Fig. 5 shows a comparison of rheological properties of STF samples prepared from 40 wt% of silica and 60 wt% of PEG with three different syntheses techniques. As shown in the Fig. 5, it is clear that the STF samples (sample (D) and sample (H)) exhibit shear thickening behavior at lower values of shear rate as compared to samples (I) prepared by simple mixing. Sample (D) has a superior shear thickening behavior as compared to other as-prepared STF samples prepared at same weight fractions of silica and PEG. These results prove that the sonochemical method is an effective synthesis technique for preparation of shear thickening fluid for liquid body armor applications.

The temperature effect on STF samples (samples (D) and sample (H)) were studied by measuring the viscosity changes at 0 °C and 40 °C. Fig. 6a depicts the rheology graph of sample (D) tested at 0 °C. These results show that the sample exhibits a shear thickening behavior at higher shear rate (7/s) as compared to the sample (D) tested at room temperature. It is also noteworthy to mention that the highest value for the sample (D) viscosity at 0 °C is ~66 Pa s which is much less than the maximum viscosity (410 Pa s) value at room temperature. When the temperature increased to 40 °C, the rheology test results show that the sample (D) exhibit shear thinning for a broad range of shear rate (3–30/s) as shown in Fig. 6b. This behavior can be explained as the temperature increases the sample viscosity decreases with the increase of shear rate, then the sample become thinner and have more scattered data for its viscosity until the viscosity become zero Pa s [37,38].

Sample (H) was also tested for its rheological measurements at 0 °C and 40 °C shown in Fig. 7a and b. These results show shear thickening behavior at 0 °C at a shear rate range between 0.3 and 3.5/s and with increase in the viscosity from 6 to 60 Pa s. These results are consistence with the results observed for STF sample (D). Similarly when the sample (H) tested at 40 °C it demonstrated a shear thickening behavior at shear rate 3–50/s. However, the increase in the viscosity is inferior to the sample tested at room temperature. These rheological results at high temperatures clearly suggest that the high temperatures have negative effects on shear thickening fluids as compared to the rheological properties at room temperature.

The actual weight percentages of silica and PEG in STF samples (sample (D) and sample (H)) were estimated using TGA experiments. The TGA graph for STF sample (D) presented in Fig. 8a shows residual weight percentage of 35% of silica at 600 °C. The 5 wt% difference in the weight percentages of added silica (40%) and remaining residual silica (35%) can be explained by the loss of silica nanoparticles during the preparation and TGA experimental error. The TGA graph for sample (H) is presented in Fig. 8b and the residual weight percentage of silica estimated is ~38 wt%. The 2 wt% difference from the added 40 wt% of silica is within the error margin of the instrument and it is acceptable. These results show that there is no loss of silica during the sonochemical synthesis process. Also the graphs show no weight loss at lower temperatures, confirming that the samples do not contain any remaining

solvents and they are pure STF. These TGA results also suggest that the smaller powder (15 nm) nanoparticles show more errors in weight fraction calculations as compared to the larger (200 nm) colloidal particles.

TEM micrographs of as-received silica nanoparticles and colloidal silica solution are shown in Fig. 9a and b, respectively. The as-received silica nanoparticles are spherical in shape and the particles sizes measured from Fig. 9a are ∼5–15 nm agglomerates. Fig. 9b shows the TEM image of as-received colloidal silica solution and the particles are highly spherical in shape and mono dispersed. No agglomerates were observed and the particles size measured ∼200 nm.

To further study the dispersion of silica nanoparticles in PEG, the SEM analyses were carried out on as-prepared STF samples. Fig. 10 shows the SEM micrographs of STF samples (sample (D) and sample (H)). Fig. 10 shows that the silica nanoparticles are well coated with PEG. Fig. 10a shows larger particle agglomerations as compared to Fig. 10b which is expected because of the large particles size differences in the starting materials and smaller nanoparticles are know to agglomerates more than the larger particles. These results are consistence with observed shear thickening behavior.

4. Conclusion

Efficient and one-pot sonochemical method has been developed to synthesize shear thickening silica dispersions. Unlike previous reports, here we have synthesized the shear thickening fluid using a dry silica nanopowder or colloidal silica solution. The main advantage of this synthesis technique compared to previous methods is that our method produces a better shear thickening transition at lower shear rate and drastically reduced the water content contamination. This sonochemical synthesis technique can also be used to synthesize larger quantities of STF samples for verity of applications including liquid body armor. The high temperature results suggest that these STFs loose its shear thickening behavior at high temperatures and more studies needs to be carried out to understand the temperature effect.

Acknowledgements

References

[1] H.A. Barnes, J. Rheol. 33 (1989) 329.
[2] J. Freundlich, J. Juliusberger, Trans. Faraday Soc. 31 (1935) 920.
[3] R.L. Hoffmann, Tran. Soc. Rheol. 16 (1972) 155.
[4] R.L. Hoffmann, J. Colloid Interf. Sci. 46 (1974) 491.
[5] R.L. Hoffmann, Sci. Technol. Polym. Colloids 2 (1983) 570.
[6] W. Boersma, J. Laven, H.N. Stein, J. Colloid Interf. Sci. 149 (1992) 10.
[7] H. Laun, H.M. Laun, R. Bung, S. Hess, W. Loose, O. Hess, K. Hahn, E. Hadicke, R. Hingmann, J. Rheol. 36 (1992) 743.
[8] L.M. Zhang, J.F. Zhou, P.S. Hui, Colloid Surf. Physicochem. Eng. Aspects 259 (2005) 189.
[9] J.W. Bender, N.J. Wagner, J. Rheol. 40 (1996) 899.
[10] T.N. Phung, J.F. Brady, G. Bossis, J. Fluid Mech. 313 (1996) 181.
[11] J. Melrose, J. van Vliet, R. Ball, Phys. Rev. Lett. 77 (1996) 4660.
[12] R.S. Farr, J.R. Melrose, R.C. Ball, Phys. Rev. 55 (1997) 7203.
[13] J.F. Brady, G. Bossis, Annu. Rev. Fluid Mech. 20 (1988) 111–157.
[14] J.W. Bender, N. Wagner, J. Colloid Inter. Sci. 172 (1995) 171.
[15] B.J. Maranzano, N. Wagner, J. Chem. Phys. 117 (2002) 10291.
[16] G. Bossis, J.F. Brady, J. Chem. Phys. 91 (1989) 1866.
[17] C.G. Albert, TAPPI 34 (1951) 453.
[18] B. Alince, P. Lepoutre, TAPPI 06 (1983) 57.
[19] S.D. Choi, Ph.D. thesis, Ann Arbor, MI, 1983.
[20] E.J.W. Verwey, J.H. de Boer, Rec. Trav. Chim. 57 (1939) 383.
[21] Z. Andreja, L. Romano, Z. Miha, TAPPI 30 (1997) 67.
[22] S.R. Raghavan, S. Khan, J. Colloid Inter. Sci. 185 (1997) 57.
[23] S. Lee, E. Wetzel, N. Wagner, J. Mater. Sci. 38 (2003) 2825.
[24] R. Egres Jr., M. Decker, C. Halbach, S. Lee, J. Kirkwood, K. Kirkwood, N. Wagner, Army Sci. Conf. (2004).
[25] S. Lee, E. Wetzel, R. Egres Jr., N. Wagner, Army Sci. Conf. (2002).
[26] C. Sauter, M.A. Emin, H.P. Schuchmann, S. Tavman, Ultrason. Sonochem. 15 (2008) 517.
[27] M. Toan, N. Tsing, T. Tsung, H. Chang, J. Vac. Sci. Technol., B 27 (2009) 1586.
[28] M.H. Choi, I.J. Chung, D.J. Lee, Chem. Mater. 12 (2000) 2977.
[29] I.G. Eskin, Ultrason. Sonochem. 8 (2001) 319.
[30] K. Suslick, Sci. Am. (1989).
[31] K. Suslick, Modem Synth. Methods 4 (1986) l.
[32] P. Boudjouk, J. Chem. Educ. 63 (1986) 427.
[33] K. Suslick, B. Edward, Flint Nature 330 (1987) 553.
[34] K. Suslick, VCH Publishers, Inc., 1988.
[35] L.A. Pérez-Maqueda, A. Duran, J.L. Pérez-Rodríguez, Appl. Clay Sci. 28 (2005) 245.
[36] F. Franco, J.A. Cecila, L.A. Pérez-Maqueda, J.L. Pérez-Rodríguez, C.S. Gomes, Appl. Clay Sci. 35 (2007) 119.
[37] S.X. Ma, S.L. Cooper, Macromolecules 34 (2001) 3294.
[38] G.N. Choi, I.M. Krieger, J. Colloid Interf. Sci. 113 (1986) 101.

# Enhancement of Knife Resistance and Interface Shear Stress

Hassan Mahfuz, DeAnna Sewell and Mujib R. Khan

In our previous work with the addition of Gluta we were able to enhance spike resistance of both Kevlar and Spectra based armors almost by a factor of 10 to 230 J-cm^2/g. Correspondingly, improvement in knife performance was just minimal. The system was made of SiO$_2$+Silane+Gluta reinforced with Spectra. This system will be considered as the reference system for this report. Although knife performance slightly improved with the use of Spectra, the energy level for zero layer penetration remained very low - within 6 J-cm^2/g. A rigorous attempt was undertaken to improve knife resistance using different chemical routes. The idea was to slow down the shearing of fabric by inclusion of nanoparticles into the matrix as well as to the fiber surface. Knife would encounter more frictional resistances cutting through a strongly bonded particle-polymer-fabric system and hence dissipate more energy. Micro-droplet tests were also conducted to determine interface shear stress and associated frictional resistance between the fiber and the matrix.

Enhancing Knife Resistance

A) Introduction of Various other Nanoparticles:

In an attempt to replace silica (SiO2), other nanoparticles such as calcium carbonate (CaCO$_3$), carbon nanotubes (CNT), and titanium dioxide (TiO$_2$) were used with identical concentration of silica. Results were somewhat mixed; CNT reinforcement increased the spike resistance for zero layer penetration to 150 J-cm^2/g compared to 10 J-cm^2/g of the reference STF-based armor. Values for other two nanoparticles; CaCO$_3$ and TiO$_2$ fell below at 90 and 110 J-cm^2/g, respectively. The results are shown in Fig.1. Although CNT showed good improvement, the results were lower than what was achieved earlier with silica. Subsequent knife tests did not show any change in knife performance.
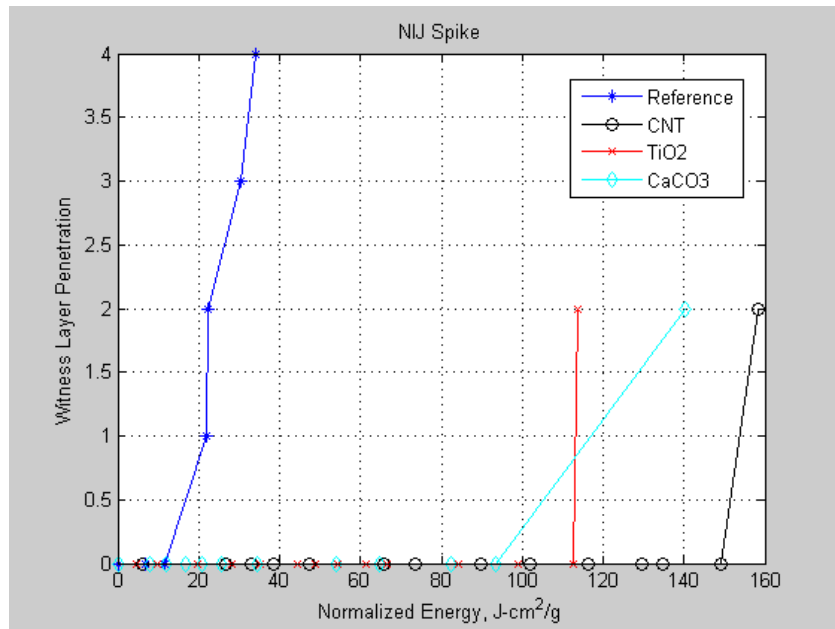
Fig.1: NIJ spike tests with various nanoparticles

B) Introduction of Styrene:

Styrene is the simplest molecule that contains an unsaturated group covalently linked to an aromatic ring and therefore represents a model candidate to be added with Silane-Gluta armor system for enhanced bonding. Since initially Spectra provided better knife performance, various weight percentage of styrene was added to the silane-Gluta system. After several trials, 50 wt% of styrene was found to be the optimum concentration. That is - styrene was 50wt% of the total polymer (silane + Gluta + Styrene). Any higher concentration above 50 wt% did not improve knife performance. Results from NIJ knife tests are shown in Fig. 2. It is observed that energy for zero layer penetration has increased from 6 $J-cm^2/g$ to 14 $J-cm^2/g$ – about 133% improvement. Energy levels for 1-4 layer penetrations were also higher as seen in Fig. 2 suggesting styrene to be an effective reinforcement for better knife performance.
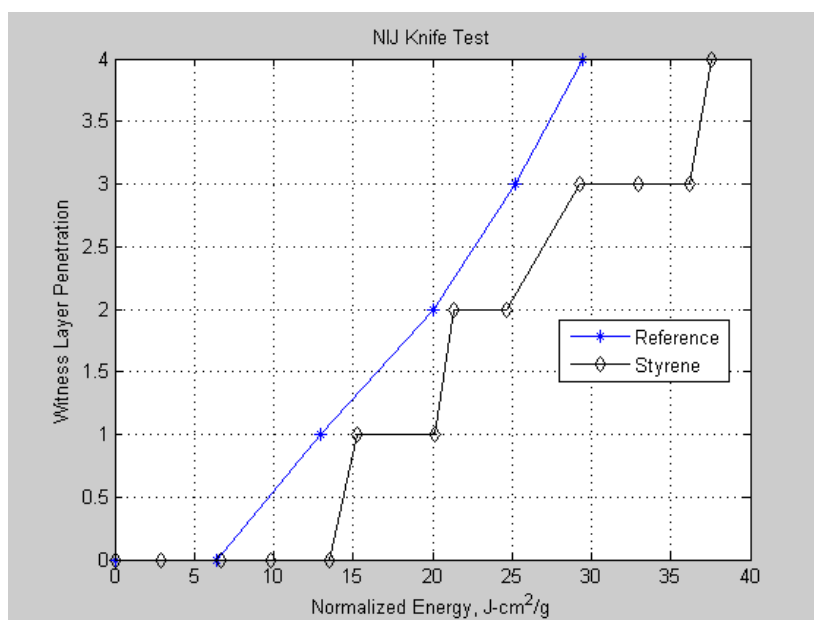

Fig. 2: NIJ Knife tests with styrene reinforcement

C) Use of POSS (polyhedral oligomeric silsesquioxane)

POSS is a nanostructured organic-inorganic hybrid polymer with a cubic structure having eight silicon atoms at the core and linked to 12 oxygen atoms. The advantage of using POSS is that these silicon atoms can be linked to a substituent that can be almost any chemical group known in organic chemistry. Chemically bonded POSS with thermoset or thermoplastic polymers either enhances or reinforces the mechanical and thermal properties of the neat material system. POSS is available commercially (Hybrid Plastics) with a multitude of functional groups. Since POSS is more like a silica molecule (1-2 nm in size) than a nanoparticle, our intention was to replace SiO_2 nanoparticles that we have used so far. Three types of POSS were used in the investigation. The types were identified according to their functional groups; trisilanol, CAO299X, and CAO300X. The last two categories were carboxylic acid based and had an aromatic ring structure attached to their reactive group. The procedure to use POSS was identical to that of SiO_2 since all three categories of POSS were soluble in ethanol. Results from NIJ knife tests are shown in Fig. 3. It is observed that knife resistance with CAO300X system is around 10 $J-cm^2/g$ for zero layer penetration. However this value is lower than 14 $J-cm^2/g$ observed earlier with styrene. It is to be noted that we were able to procure only a small

quantity of CA300X POSS as the supplier had only a limited stock. This prevented us to have multiple soaking of Spectra with POSS reinforced silane. We strongly believe that multiple soaking with POSS, knife resistance could go beyond that of styrene.
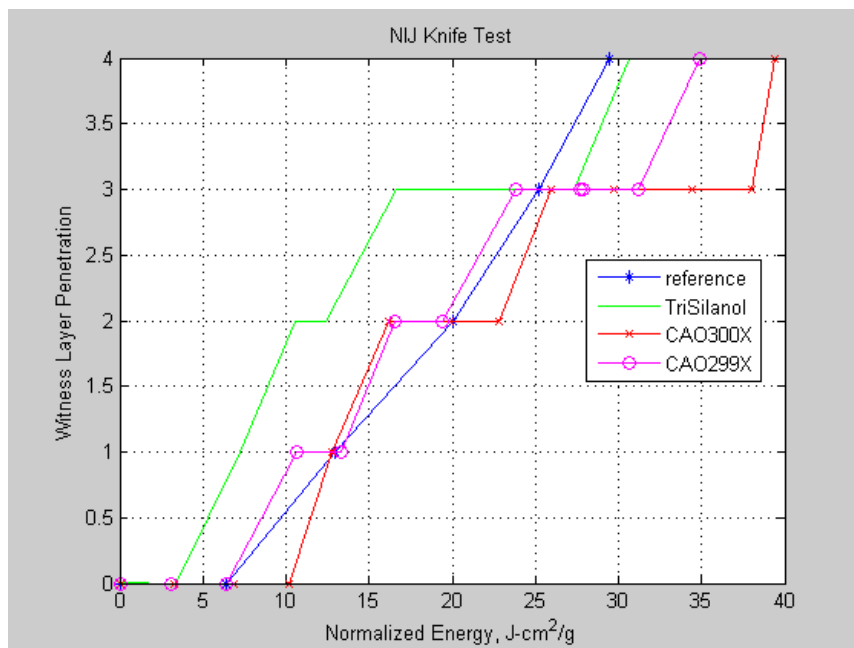

Fig. 3: NIJ knife tests with POSS reinforcement

D) Multiple Soaks with the Reference Solution

The reference solution here is the original SiO_2+Silane+Gluta solution that was used to soak Spectra fibers. To increase the amount of particles adhering to the fiber surface, multiple soaking strategy were taken. After each soak, fabrics were dried and soaked again in a fresh solution, and then dried again. This continued for 2-3 times and the materials were ready for NUJ knife tests. Results are shown in Fig.4. As expected, triple soaking helped improve knife resistance to 20 J-cm^2/g for zero layer penetration – by far the best performance we have seen so far. Soaking beyond three times resulted in excess silica in the panel and thus lowered the energy level.
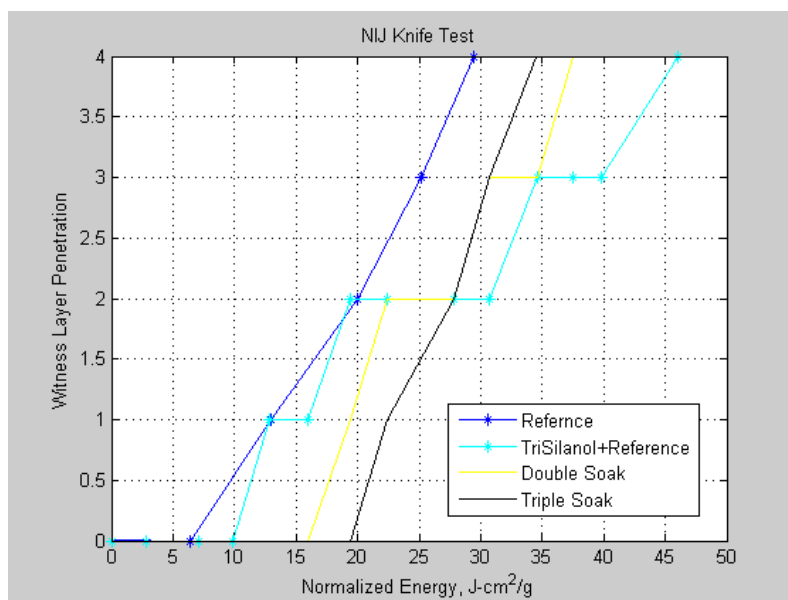
Fig. 4: NIJ Knife tests with multiple soaks

Micro-Droplet Tests:

It was clear from the current knife tests as well from spike tests conducted during previous years that a good amount of impact energy was absorbed by friction between fiber and the surrounding particle-polymer mixture. This friction arises as the fibers tend to dynamically slide during impact. Micro-droplet tests were conducted to assess the interface shear stress and associated energies. The most challenging task was to prepare specimens for micro-droplet tests since the matrix viscosity changed with the addition of silica and Gluta.

A set up was made with flat plate with two raised ends (parallel to each other) and the fibers were held tight for droplet application. A droplet applicator was made by using a regular toothpick with a fiber taped onto it. The applicator was dragged through the particle-polymer mixture, and applied to the fiber in one steady stroke. Droplets were then cured in an oven in horizontal position. The viscosity of silane-silica-Gluta mixture was carefully controlled by drying the mixture after sonication. Drying time varied depending on the amount of ethanol present in the solution. Droplets were around 150-200 μm in size as shown in Fig. 5. After curing, the droplets were cut off the plate with a fiber length of about 12.5 mm having droplet in the middle. They were then glued to a capillary tube at one end and a hook glued to the other end of the tube to hang the sample. Measurements were then taken for the following: droplet length (*l*), fiber diameter (*d*), and the length from the capillary tube to the tip of the droplet. Measurements were taken through a microscope.

Micro-droplet specimens were taken to University of Delaware and tests were performed there. The test set up consisted of a load cell, two light sources, two cameras (one horizontal and one vertical) with video monitors, two parallel blades, and a motor controller to move the specimen up and down. The test set up is shown in Fig. 6. The distance between the blades is moved manually, but viewed by the vertical camera. The motorized movement and application of load were controlled by a custom LabView program. A sample load displacement curve obtained from the tests is shown in Fig. 7.
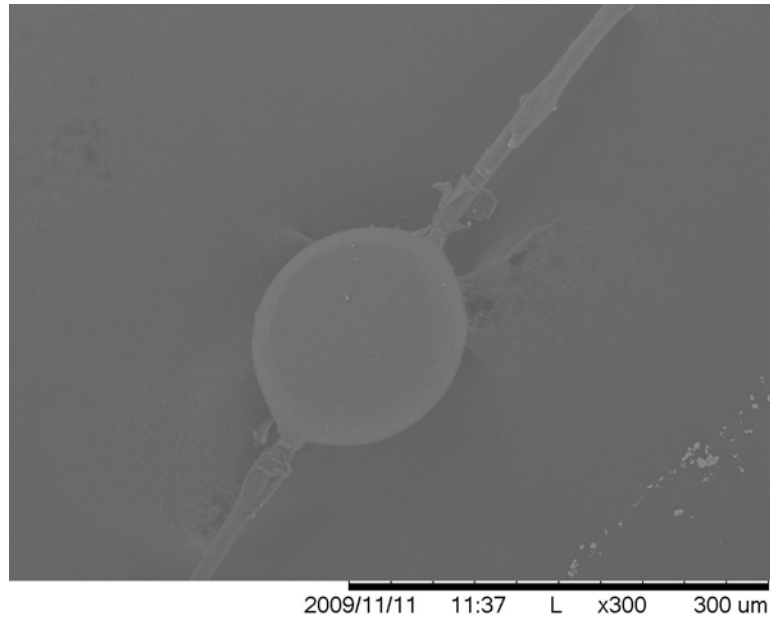
4

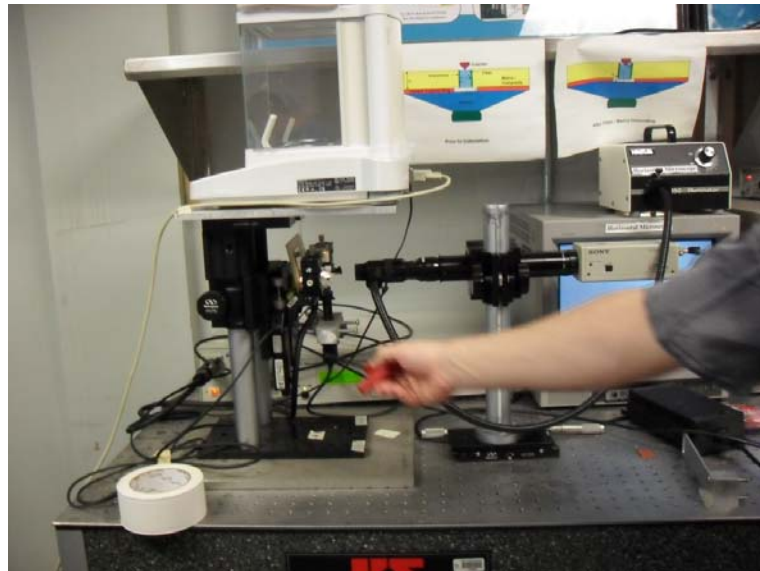Fig. 5: Microdroplet with embedded fiber

Fig. 6: Micro droplet test set up

The figure indicates a very small force compared to conventional fiber/matrix debonding force. However, we observe a much greater energy absorption in dynamic and static sliding region due to a large amount of friction. This behavior is similar to strain hardening behavior of materials but caused by friction between fiber and particle-polymer mixture in this case. We believe such high friction is responsible to absorb a large amount of energy during spike and knife tests.
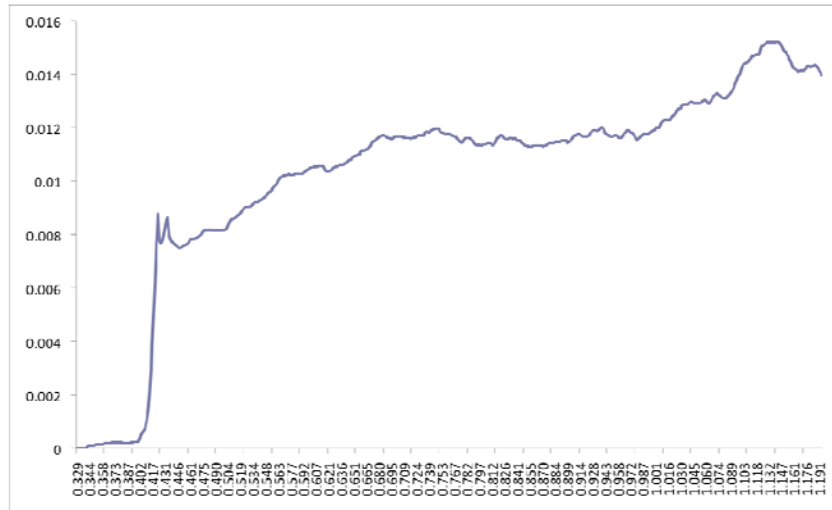
Fig. 7: Load vs. displacement curve from micro droplet test

Summary:

It has been shown that knife resistance of Kevlar is extremely weak compared to that of Spectra. Energy absorption by Spectra with regular solution of silane+silica+Gluta is still low but can be substantially increased by addition of styrene and POSS to the solution. Especially, multiple soaking up to three times was very effective – it enhanced knife resistance from 6 J-cm^2/g to 20 J-cm^2/g. Micro droplet tests were performed in collaboration with University of Delaware and it was demonstrated that friction at the fiber/matrix interface was responsible for absorption of most of the energy during spike or knife penetration.

ORIGINAL CONTRIBUTION

Investigating the transient response of a shear thickening fluid using the split Hopkinson pressure bar technique

**Amanda S. Lim · Sergey L. Lopatnikov ·
Norman J. Wagner · John W. Gillespie Jr.**

Abstract The split Hopkinson pressure bar (SHPB) technique is implemented to evaluate the transient response of a colloidal suspension exhibiting shear thickening at strain rates and timescales never before explored in a laboratory instrument. These suspensions are shown to exhibit a discontinuous transition from fluid-like (shear thinning) to solid-like (shear thickening) behavior when evaluated using rotational rheometry. The effect of loading rate on this transition time is studied for a particle volume fraction of 0.54 using the SHPB technique. It is shown that the time required for transition to occur decreases logarithmically with loading rate. From these results, we conclude that transition is not triggered by a characteristic shear rate, but rather a critical shear strain is required. Results from SHPB experiments performed up to Peclet numbers of order 10^7 are presented and discussed for 0.50, 0.52, and 0.54 particle volume fraction suspensions.

Keywords Shear thickening · Colloidal dispersion · Squeeze flow · High strain rate · Impact

A. S. Lim · J. W. Gillespie Jr. (✉)
Center for Composite Materials,
Department of Materials Science and Engineering,
University of Delaware, Newark, DE 19716, USA
e-mail: gillespi@udel.edu

S. L. Lopatnikov · J. W. Gillespie Jr.
Center for Composite Materials,
Department of Civil and Environmental Engineering,
University of Delaware, Newark, DE 19716, USA

N. J. Wagner
Center for Composite Materials,
Department of Chemical Engineering,
University of Delaware, Newark, DE 19716, USA

Introduction

The focus of this study is on monodisperse suspensions of colloidal particles, which have been shown to transition rapidly from a fluid-like (Newtonian or shear-thinning) to solid-like state under an increasing applied shear load (Barnes 1989); the micromechanics of shear thickening behavior was first explored over three decades ago (Hoffman 1972).

Shear thickening suspensions appear in many applications, such as paints, cement, and abrasive cleaners (Larson 1999; see also, for example, a recent workshop by Coussot and Wagner 2009), where shear thickening is often undesirable and limits the application. On the other hand and more specific to this research, shear thickening hard-sphere colloidal suspensions have found applications in a variety of fields, including impact resistance (Lee et al. 2003; Tan et al. 2005; Decker et al. 2007) and vibration mitigation (Laun et al. 1991), specifically in composite sandwich structures (Fischer et al. 2006), automotive dampers (Helber et al. 1990), and padding for hip protectors (Robinovitch et al. 1995). As many of these applications are dynamic by nature, understanding the response of shear thickening suspensions under dynamic loading, especially at very high rates, is of importance. However, to date, studies of the dynamics of shear thickening have been limited to timescales typically accessible in commercial rheometers, which is on the order of 10 ms, and at shear rates under 10^5 (Bender and Wagner 1996; O'Brien and Mackay 2000; Lee and Wagner 2003).

From a dynamic standpoint, the time required for this transition to occur and the factors affecting this are critical for many applications, such as in ballistic protection. This time will depend on the microstructural

rearrangement of the particles necessary for the shear thickening response. Historically, shear thickening was believed to be a result of particle rearrangement from an ordered, layered state to a disordered state; this is known as the order-to-disorder transition (ODT) theory (Hoffman 1972; Barnes 1989; Boersma et al. 1990). This transition was considered to be shear rate dependent; at sufficiently high rates of shear, the shear stress between layers is "sufficient to overcome the forces holding the sphere in layers" (Hoffman 1974). Since then, several researchers have demonstrated that, although shear thickening may accompany an order disorder transition, the ODT is neither necessary nor sufficient in itself to cause shear thickening (Laun et al. 1992).

Stokesian Dynamics simulations of Brady and Bossis later demonstrated the onset of transition as the point at which the applied shear forces are balanced by short-range hydrodynamic lubrication forces acting between particles (Brady and Bossis 1988). At this point, the particles form dynamic aggregates known as *hydroclusters* (Bender and Wagner 1996; Vermant and Solomon 2005), which percolate and jam, resulting in a discontinuous increase in viscosity (Maranzano and Wagner 2002). The onset of shear thickening has been shown to scale with shear stress as opposed to shear rate (Bender and Wagner 1996; Maranzano and Wagner 2001a, b).

Hydroclusters have been observed through rheo-optical experiments (D'Haene et al. 1993; Bender and Wagner 1995), stress-jump rheological measurements (Kaffashi et al. 1997; O'Brien and Mackay 2000) and neutron scattering methods (Laun et al. 1992; Bender and Wagner 1996). Maranzano and Wagner further expand on these studies by performing in situ small angle neutron scattering (SANS) experiments, known as Rheo-SANS (Maranzano and Wagner 2002). These results confirm the simulation predictions that shear thickening is a consequence of hydrocluster formation driven by lubrication hydrodynamics. Kalman and Wagner also performed flow-ultra small angle neutron scattering (flow-USANS) experiments (Kalman and Wagner 2009), observing that hydroclusters take the form of transient, compact clusters with a broad size distribution.

Some efforts have been made to understand the *dynamic* behavior of a shear thickening suspension. Laun et al. observed that a critical shear rate was required for thickening at low frequencies while a minimum shear strain was necessary at high frequencies (Laun et al. 1991). Lee and Wagner perform oscillatory shear measurements on silica particle suspensions and also demonstrated that the critical strain required for thickening to occur scales inversely with frequency. How-

ever, the apparent minimum strain required at higher frequencies was determined to be a consequence of wall slip, and strain amplitudes as low as 10% or less were sufficient to induce shear thickening at high enough frequencies (Lee and Wagner 2003). In brief, the same magnitude of applied shear stress was necessary to induce shear thickening in oscillatory shear as required for steady shear and no minimum displacement was found to limit this behavior within the frequency and shear rate range explored. Note that these measurements were performed in dynamic oscillatory shear under "steady state" conditions where the sample has reached a steady oscillatory response. It is not intuitively obvious how this behavior will translate to other non-steady flows, such as those encountered in some proposed applications of shear thickening fluids.

To better understand the dynamic response of a concentrated colloidal suspension at very high shear rates and under transient, start up flows, it is necessary to develop an experimental method capable of measuring the transient response while eliminating the problem of wall slip. The aim of this study is to measure the transient response of a shear thickening fluid at high rates ($>10^5$ s^{-1}) and stresses (>30 MPa) using the experimental procedure demonstrated in (Lim et al. 2008a, b). From these results, it will be possible to identify the time and strain required for the shear thickening transition to occur and to evaluate the effect of loading rate on this process.

The split Hopkinson pressure bar (SHPB) technique can achieve high stresses and deformation rates in a transient squeeze flow experiment. In addition, the SHPB is used to load the fluid under squeezing flow; this compressive loading minimizes the problem of wall slip, which can occur in rotational rheometers especially for high viscosity samples (Lee and Wagner 2003). Although the flow field is not simple shear, there is prior evidence that shear thickening suspensions can be studied in similar flow types. Laun et al. evaluated shear thickening colloidal suspensions and found that the neutron-scattering patterns obtained under Poiseuille flow "can also be correlated to the various transitions of the viscosity function," meaning that it is possible to capture the transition under the various shear rates applied in Poiseuille flow (Laun et al. 1991). Finally, with a sampling rate of 5 MHz (0.2 μs timestep) the SHPB technique is able to measure the transient response of the fluid at frequencies orders of magnitude faster than ever before.

While the current study uses the SHPB as a dynamic squeeze flow experiment, there is precedence for using the SHPB to evaluate the response of fluids under pure shear (Clyens et al. 1982; Ogawa 2003) and pure

compression (Kenner 1980; Hoglund and Larsson 1997; Åhrström et al. 2002) loading. The squeeze flow SHPB configuration has been validated for Newtonian fluids (Lim et al. 2008a, b) and an analysis is performed to demonstrate the accuracy of the results presented in this paper.
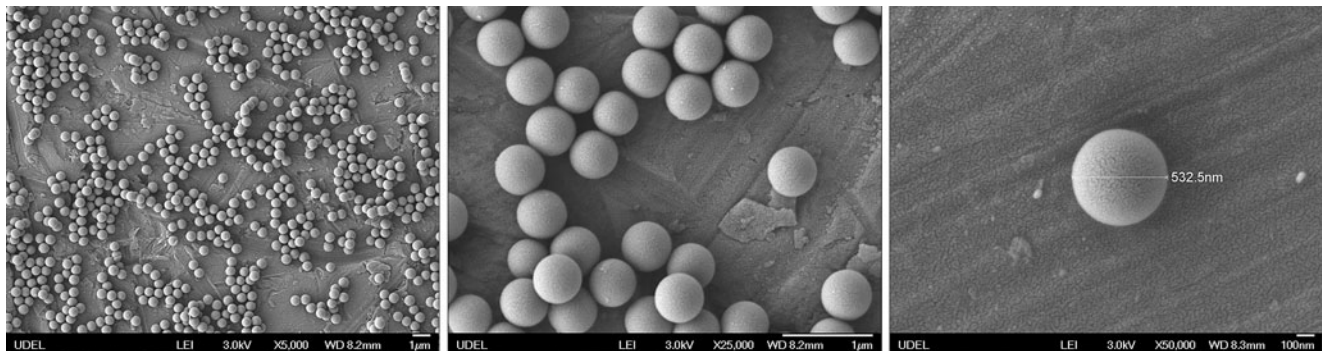
Materials and methods

Suspension preparation

The hard-sphere colloidal suspensions (referred to as shear thickening fluids, STF) evaluated in this study consist of 50%, 52%, and 54% volume fraction (ϕ) silica particles and have been the subject of earlier investigations (Kalman and Wagner 2009). The silica particles (Fig. 1) are nearly monodisperse with a hydrodynamic diameter of 520 nm with less than 10% polydispersity as reported previously. These particles were oven dried and suspended in polyethylene glycol 200 (Alfa Aesar) through a combination of hand mixing and roll mixing for 72 h.
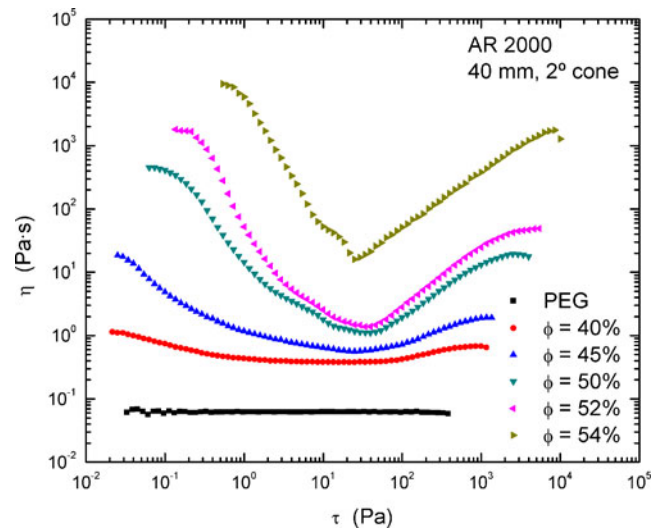
Densities (ρ) of 1.95 g/cc and 1.127 g/cc are reported by the manufacturers for the silica particles and polyethylene glycol 200, respectively. A sound velocity (c) of 1,650 m/s ($\rho = 1{,}120.5$ kg/m^3, $K = 3.05$ GPa) is reported for low molecular weight polyethylene glycols (Sasahara et al. 1998). For silica glasses, a sound velocity of 5,869 m/s is reported (Lynch 1980). To determine the density of the suspension or shear thickening fluid, a rule of ideal mixtures is used (Eq. 1).

$$\rho_{\text{STF}} = \phi_s \rho_{\text{silica}} + (1 - \phi_s)\, \rho_{\text{PEG}} \tag{1}$$

This yields a suspension density of 1.57 g/cc. These material properties will be used in later calculations in the subsection on specimen design.


Fig. 2 Steady state shear viscosity of the colloidal dispersions at varying volume fractions and the suspending medium (PEG)

Shear rheology

The steady state shear viscosity of these STFs is plotted along with that for the suspending medium, PEG 200 in Fig. 2. This was measured using an AR-2000 rotational rheometer in the steady-state shear sweep mode using a 40 mm 2° cone and plate with Peltier temperature control at 25°C. These STFs exhibit a shear thinning regime, followed by a strong shear thickening response at relatively low shear rates (1–200 s^{-1}). Note that the point of shear thickening occurs around 3–4 Pa for the most concentrated samples (Fig. 2), and that this behavior is reversible (the data are both ascending and descending curves superimposed). In contrast, the PEG 200 is essentially Newtonian over this range of shear rates.

At lower volume fractions ($\phi < 40\%$), the suspension exhibits only comparatively weak shear thinning and thickening (Bender and Wagner 1996). As the fo-

Fig. 1 Silica particles at increasing magnifications

Fig. 3 Split Hopkinson pressure bar experimental apparatus
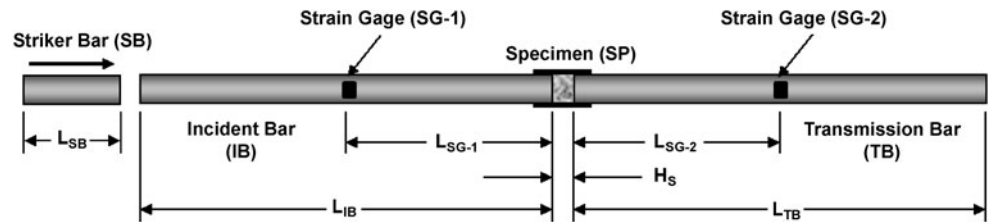
cus of this study is the transitional thickening response of these materials, lower concentrations were not evaluated.

Split Hopkinson pressure bar

The high stress/shear strain rate response of these materials was evaluated using the split Hopkinson pressure bar technique (Grey III 2000; Gama 2004), which has been adapted to evaluate Newtonian fluids under fast squeezing flow (Lim et al. 2009). In this previous work, the SHPB technique is proven to achieve viscosity measurements predicted using a Newtonian squeeze flow model which was developed by Kuzma (1967) to account for inertia. The experimental apparatus is shown in Fig. 3. Due to the large number of articles describing this experimental technique (in particular please note Gama et al. (2004)), this section will be kept fairly brief.

During testing, the striker bar is fired out of a gas gun through a 1-m long tube before impacting the end of the incident bar. All bars are aluminum 6061 with a diameter of 0.0191 m (0.75 in.). A pulse shaper (EPDM rubber, 1/4″ diameter, 1/32″ thick) is placed at this interface which deforms slower than the bar,

resulting in a near-triangular loading pulse (ε_I) shown in Fig. 5. At the IB-SP interface, a fraction of this pulse is reflected (ε_R) back through the incident bar and the rest is transmitted (ε_T) through the transmission bar, depending on the acoustic impedance ($z = \rho c$) of the specimen and bars. These pulses are measured using twin strain gages which are mounted at the center of each bar and configured in a rosette formation designed to omit radial strain. From these pulses ($\varepsilon_I, \varepsilon_R,$ and ε_T), the applied loading rate ($\dot{U}$) and force (F) acting on the fluid specimen can be calculated (Kolsky 1949; Gama et al. 2004). The experimental parameters are summarized in Table 1.

The specimen coordinate system is defined in Fig. 4, where U_1 is the incident bar end displacement and U_2 is the transmission bar end displacement. The strain rate applied to the specimen is determined by subtracting the motion of the incident and transmission bar ends (Eq. 2). Similarly, the average stress at each timestep is calculated by averaging the stress in each of the bars (Eq. 3). In this expression, A_B and A_S represent the cross-sectional area of the bar and specimen, respectively, which are equal in these experiments. In this way, the applied compressional strain (integral of compressional strain rate), compressional strain rate, and compressional stress can be determined without

Table 1 SHPB experimental parameters

Parameter	Symbol	STF
Incident bar length	L_{IB}	1.83 m (6′)
Transmission bar length	L_{TB}	1.83 m (6′)
Incident bar diameter	D_{IB}	0.0191 m (1″)
Transmission bar diameter	D_{TB}	0.0191 m (1″)
IB strain gage distance from specimen	L_{SG-1}	0.915 m (3′)
TB strain gage distance from specimen	L_{SG-2}	0.915 m (3′)
Incident bar elastic modulus	E_{IB}	65.4 GPa
Transmission bar elastic modulus	E_{TB}	65.6 GPa
Density	ρ	2,700 kg/m^3
Measured sound velocity (IB)	$C_{0,IB}$	4,920 m/s
Measured sound velocity (TB)	$C_{0,TB}$	4,930 m/s
Striker bar diameter	D_{SB}	0.0191 m (3/4″)
Striker bar length	L_{SB}	0.102 m (4″)
Specimen thickness	H_S	0.00055 m
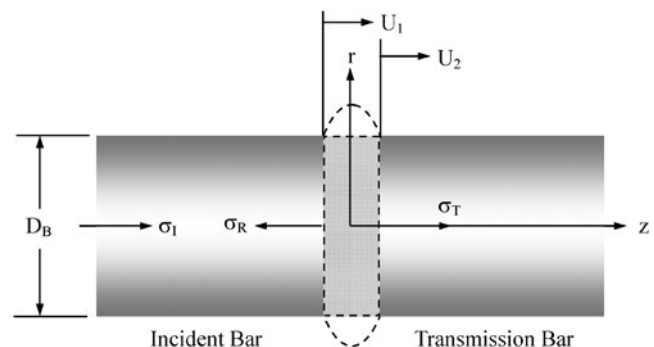
Fig. 4 Diagram of the specimen coordinate system (Lim et al. 2009)

requiring any knowledge of the material properties of the specimen.

$$\dot{\varepsilon} = \frac{C_{0,IB}\left(-\varepsilon_I + \varepsilon_R\right) + C_{0,TB}\varepsilon_T}{H_S} \quad (2)$$

$$\sigma = \frac{A_B E_B}{2A_s}\left(\varepsilon_I + \varepsilon_R + \varepsilon_T\right) \quad (3)$$

Thus, the compressional stresses, strain rates, and strains are reported here as "engineering" values, namely with reference to the initial sample cross-sectional area (A_S) and thickness (H_S), respectively. This is traditional in the SHPB method (Gama et al. 2004) as well as often employed in polymer squeeze flow testing.

During testing, the suspension is placed at the interface between the incident and transmission bars. The specimen is then covered by a flexible band, which prevents loss of material due to gravity while allowing the specimen to expand radially. The pressure developed by the band has been measured previously by Lim et al. (2009) and was found to be two orders of magnitude lower than pressures associated with the Hopkinson bar experiments performed in this research. Therefore, this band has a negligible effect on measurements made during testing. Experiments are conducted at an average temperature of $22.4 \pm 0.4°C$. For each experiment, a new specimen is used and the temperature before and after testing is measured.

To demonstrate consistency between experiments, two test results are compared in Fig. 5. The incident bar strain gage signal is plotted for each test with the incident (negative/compressive) and reflected (positive/tensile) pulses marked. The incident pulses are nearly identical (test 2 has a peak stress within 5% of test 1), indicating that these experiments were performed under the same conditions. The reflected pulses are also nearly identical; if experiments were not reproducible, the reflected pulse would vary between the two.

Specimen design

Thin specimens (0.55 mm) are used in order to achieve a strong transmitted signal. These specimens are 1,000 times larger than the average particle diameter, ensuring that homogeneous suspension properties are being probed. The specimen radius is kept equal to that of the incident and transmission bars in order to ensure that there is no dispersion due to reflections off the bar ends (Gama 2004).

A specimen may be considered to be in force equilibrium after an initial *ringing up* period (Gray III 2000), which is a function of the material properties and geometry. This is often discussed in terms of the specimen thickness and sound velocity; in fact, a typical estimate is $4t_0$, "where t_0 is the transit time for the leading edge of the pulse traveling through the specimen." (Ravichandran and Subhash 1994; Li and Lambros 1999). A rough estimate of the ringing up time for our material can be calculated with the understanding that, when dealing with a fluid, more complex processes will contribute to equilibrium (Lim et al. 2009). The sound velocity of the suspension is bound by the sound velocity of bulk silica and that of the solvent ($c_0 = 1{,}650–5{,}869$ m/s). A specimen thickness of 0.55 mm yields a ringing up period of 0.37–1.33 µs.

This ringing up time may also be determined experimentally using the homogenization ratio, $R(t)$ (Ravichandran and Subhash 1994), where σ_{IB} and σ_{TB} are the axial stresses at the IB and TB ends of the specimen (Eq. 4).

$$R(t) = \left| \frac{\sigma_{IB} - \sigma_{TB}}{(\sigma_{IB} + \sigma_{TB})/2} \right| \quad (4)$$

This ratio is plotted in Fig. 6 for a typical suspension specimen. The ringing up period is considered complete when the variation between the incident and transmission bar stresses drops below 10%. For the experiment plotted in Fig. 6, this occurs within 50 µs. That this time is larger than predictions based on model elastic materials (which consider only sound travel time) is reasonable given that the rheological behavior of the suspension is viscoelastic. It will be shown that
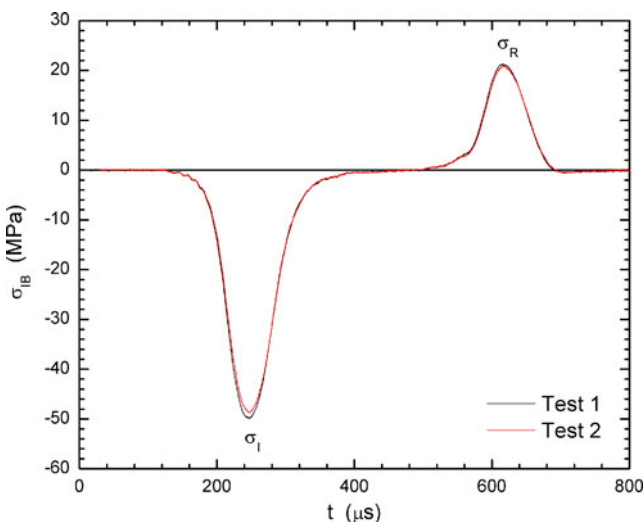
Fig. 5 Incident bar strain gage signals for two experiments performed under identical conditions
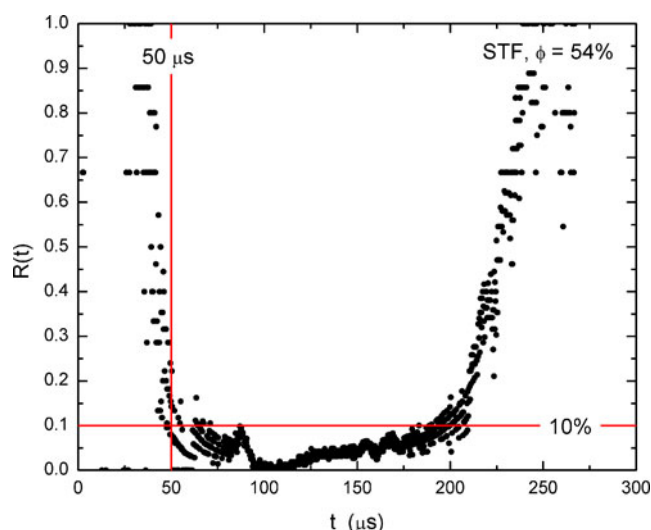
Fig. 6 Ringing up period for a 54 vol.% STF

measurements pertaining to transition time are taken after ringing up is 90% complete.

Experiments have been performed on the 54% silica suspension in order to assess the effect of specimen thickness (Lim et al. 2009). It was found that, at this concentration, specimen thickness did not have an effect on the stress–strain–strain rate behavior of the suspension.

Experiment

During testing, the impact from the striker bar generates a transient stress wave, which exhibits Gaussian-like behavior (Fig. 5), ramping from zero up to a maximum rate of 12,200 s^{-1} for the highest pressures used. The resulting axial motion of the incident bar causes the suspension to undergo axial compression. As this occurs, the specimen expands radially, hence the previously made analogy to squeezing flow is appropriate. Applying the kinematics of steady squeeze flow and under the assumption of Newtonian fluid behavior, this strain rate corresponds to a maximum wall shear rate for a specimen of radius R, (Eq. 5) of 1.27×10^6 s^{-1} at the radial edge of the sample (Lim et al. 2009).

$$\dot{\gamma} \approx \frac{6R}{H_S} \dot{\varepsilon} \tag{5}$$

This may be better stated as a maximum Péclet number of $\sim 10^7$ (Eq. 6), which describes the relative importance of convection over diffusion (Hiemenz and Rajagopalan 1997). At these extremely high Pe values, hydrodynamic interactions in the suspension are

expected to dominate Brownian motion, and shear thickening should be evident. Here, η_c is the solvent viscosity, a is the particle radius, k_B is the Boltzmann constant, and T is the experimental temperature.

$$Pe = \frac{6\pi \eta_c a^3 \dot{\gamma}}{k_B T} \tag{6}$$

Results

Figures 7 and 8 present the results from 20 SHPB tests performed on the 54% volume fraction silica-based suspension at varying impact velocities obtained by varying the gas gun pressure. The curves are labeled with the maximum strain rate achieved during each experiment as a means of differentiating between tests, since the Hopkinson bar does not provide a constant rate experiment. In Fig. 9, the loading and unloading of the specimen is depicted in terms of the axial stress acting on the sample as a function of the instantaneous axial strain. Note that these are calculated directly (Eqs. 2 and 3) from the measured pulses at the two strain gages and the calculation does not involve any assumptions of material properties or flow kinematics in the sample. From Fig. 9, it is clear that the material stiffens nonlinearly under loading, and higher stresses are generated for higher strain rates during loading, although there is some scatter in the data. This curve represents the complete loading and unloading of the STF, which undergoes a large amount of hysteresis as the sample undergoes squeeze flow out of the gap between the bars. At the lowest impact velocities (maximum strain rate of 1,800 s^{-1}) the sample loads rapidly and gradually reaches a maximum stress at strains below 10%. As the sample is highly viscous, even in the shear thickened state, releasing the axial stress leads to a rapid drop in strain with negligible recovered strain. Any significant recovered strain would be an indication of elastic behavior.

Figure 8 shows only the loading portion of the curve as a function of the instantaneous axial strain rate during the course of the test. The 's-shaped' curve in Fig. 8 appears as a result of deceleration during loading; this is not due to the shape of the loading pulse, which is nearly Gaussian. Rather, this occurs as a result of a change in the specimen material properties, such as would be qualitatively expected for a sample showing shear thinning followed by shear thickening. In this representation, the data vary systematically at lower strain rates, but due to the change in profile observed in

Fig. 7 Stress-strain data for
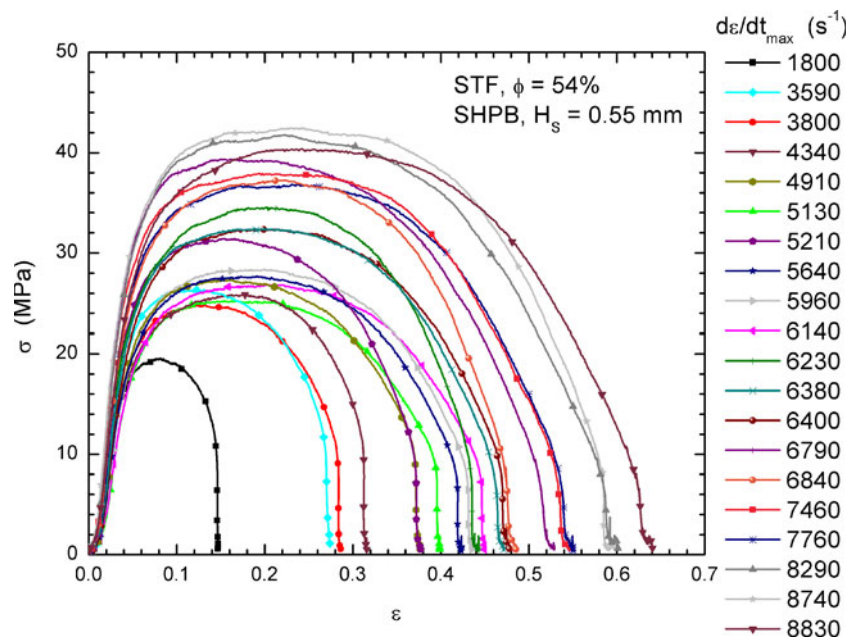the 54 vol.% suspension
obtained via SHPB technique

Fig. 7, are not obviously ordered at higher strain rates. These two representations of the data indicate that both strain rate and strain affect the state of stress of the sample.

To help better understand the specimen's response, Fig. 9 compares the SHPB results for a 54 vol.% suspension with the model calculations for a Newtonian fluid specimen with a viscosity of 15 Pa s under the same test conditions. The calculations use the quasi-static squeeze flow model, which accounts for radial inertia (Kuzma 1967). During loading, the STF undergoes an initial period of deformation marked by an increase in stress with strain rate. At stresses above 2 MPa, the bars decelerate, indicating substantial stiffening within the specimen. After this point (∼5 MPa), the STF continues to deform under loading with high resistance. Unloading leads to a higher stress during deceleration with substantial hysteresis. The sample has a much higher stress at the lower shear rates during deceleration. This is in contrast to the Newtonian fluid, which undergoes near linear loading and unloading, with no evidence of stiffening. Behavior of the 0.50 and 0.52 volume fraction silica suspensions is presented and discussed in the Appendix.
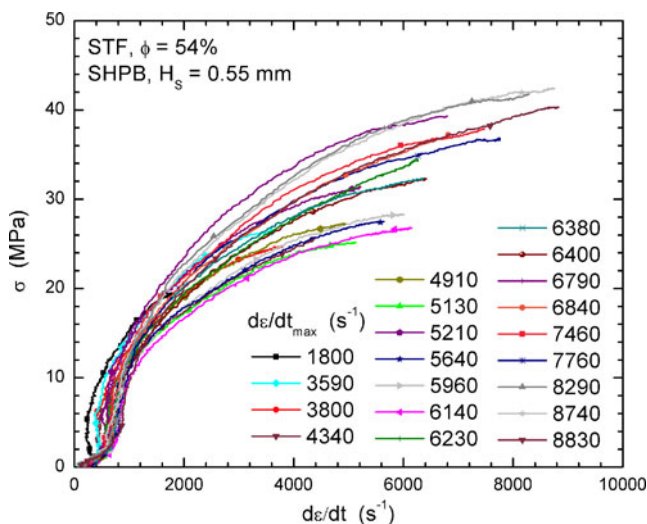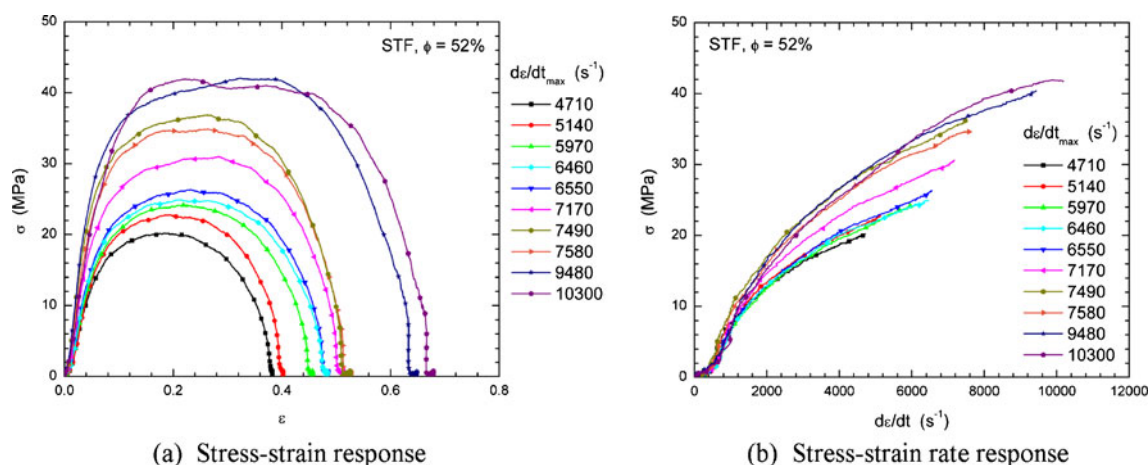

Fig. 8 Loading portion of the stress–strain rate data obtained via SHPB technique
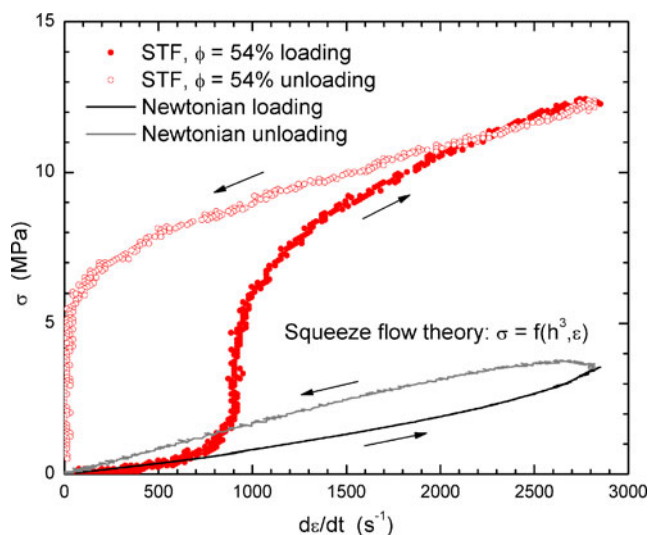
Fig. 9 Comparison of results for a 54% STF with calculations for a 15 Pa s Newtonian fluid

Fig. 10 Mechanical response of a 52 vol.% STF tested via SHPB technique

Analysis

Defining the transition

As stated previously, a shear thickening suspension is expected to form transient structures, so called "hydroclusters" during shear thickening, which results in a dramatic increase in both sample stiffness and dissipation. For the most highly concentrated suspension, the shear rheology shows a nearly discontinuous increase in stress at a nearly constant shear rate (Fig. 2). This rapid increase in stiffness is hypothesized to arise from hydrocluster formation sufficient to result in a bridging of the specimen gap, leading to "jamming".

In the Hopkinson bar experiments, this behavior causes a significant decrease in compression rate during loading. While this is seen to occur in Fig. 8, this can be more quantitatively described using a plot of the specimen compression acceleration where $\ddot{U}$ is calculated

by taking the time derivative of the compression rate (Fig. 10). It should be noted that, here, compression acceleration is plotted as positive. In this plot, markers have been inserted to show the onset and completion of the period of deceleration.

That this behavior is consistent with a change in material properties of the specimen and is not an artifact of the experimental method is made clear when examining the loading pulse, which is near-Gaussian in shape. Using this information, we can then state that this is the region during which jamming occurs and the onset and end of deceleration are considered to define the period of transition. In Fig. 9, this period coincides with the point of inflection on the stress–strain rate plot. This is followed by a period in which stress increases drastically without an increase in deformation rate (Fig. 9).

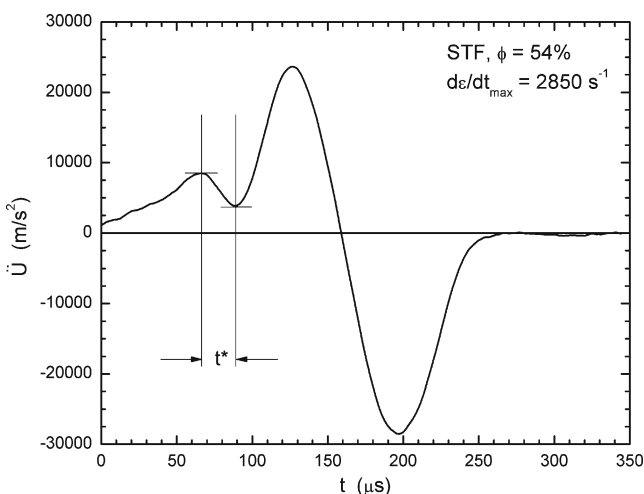The transition times for 36 experiments on the 54 vol.% suspension are plotted as a function of the
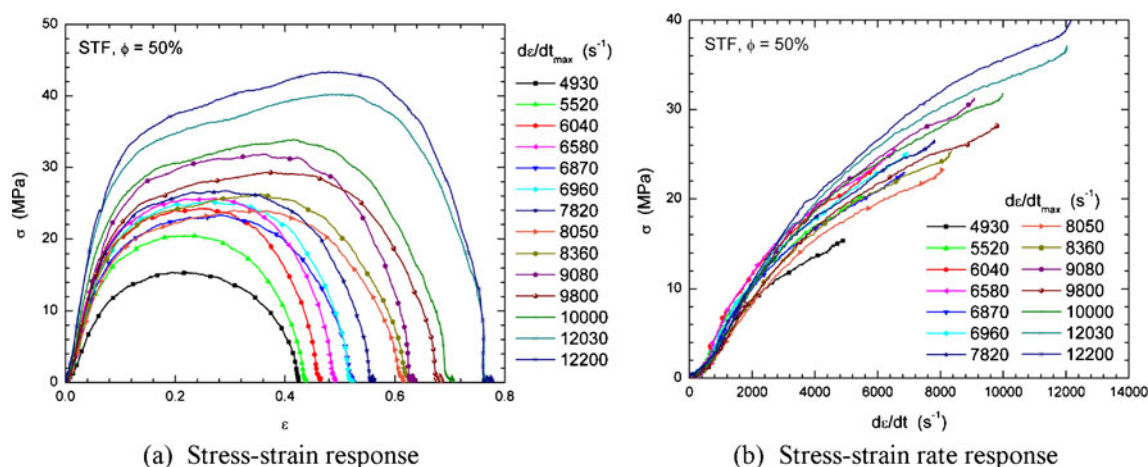
Fig. 11 Mechanical response of a 50 vol.% STF tested via SHPB technique

maximum strain rate of each test (Fig. 11). The transition time decreases with increasing strain rate and ranges from 50 to 20 μs. From this plot, it is evident that the transition time decreases exponentially with the maximum compressive strain rate.
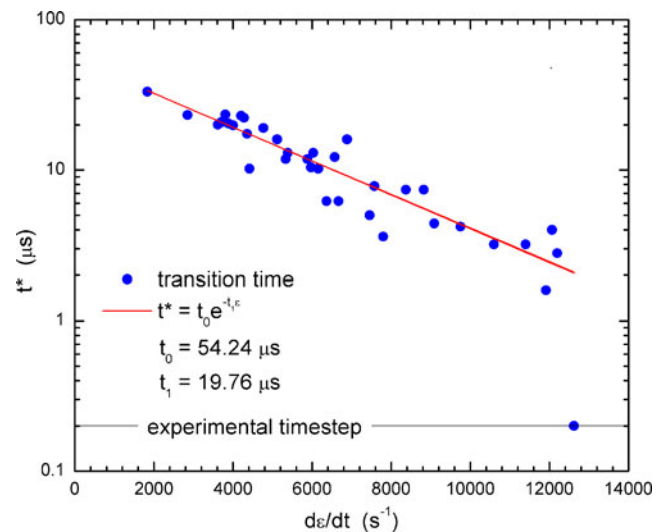
Concentration effect

The effect of colloid concentration on the mechanical response of a hard-sphere suspension can be observed by comparing samples at similar conditions. In Fig. 12, the incident bar strain gage signal has been plotted for 50, 52, and 54 vol.% suspension. The incident wave is negative since the loading is compressive while the reflected tensile wave is positive. These experiments all have very similar loading pulses, hence it is appropriate to directly compare them. As expected, the highest concentration suspension exhibits higher stiffness and lower hysteresis than the other two concentrations (Fig. 13a). Interestingly, the suspensions appear to undergo similar loading behavior prior to stiffening (Fig. 13b), but the discontinuous shear thickening sample (54%) exhibits a much sharper rise in stress at the transition than the continuous shear thickening samples of lower volume fraction. That the transition, defined as a decrease in compressive acceleration, appears to begin at approximately the same stress for each sample is consistent with the observations of the steady state rheology in Fig. 2.

The fact that these facets of the mechanical behavior of the STF suspensions can be captured here demonstrates the applicability of the SHPB experimental technique for complex fluid evaluation. It is possible to ob-


Fig. 13 Transition time for 36 SHPB experiments as a function of strain rate

serve the changes in material response which can occur with a change as small as 2% volume silica, similar to that observed in a rotational rheometer (Fig. 2).

Discussion

Transition

The results in Fig. 11 indicate that the time required for a STF to transition decreases logarithmically with loading rate. This indicates that a specimen is able to transition to the shear thickened state faster at higher compression rates. This alone is an interesting conclusion, but does not address the issue of whether

Fig. 12 Acceleration of a 54% silica specimen plotted against time. The plot includes both loading and unloading responses. The time for shear thickening is defined by the indicated transition points
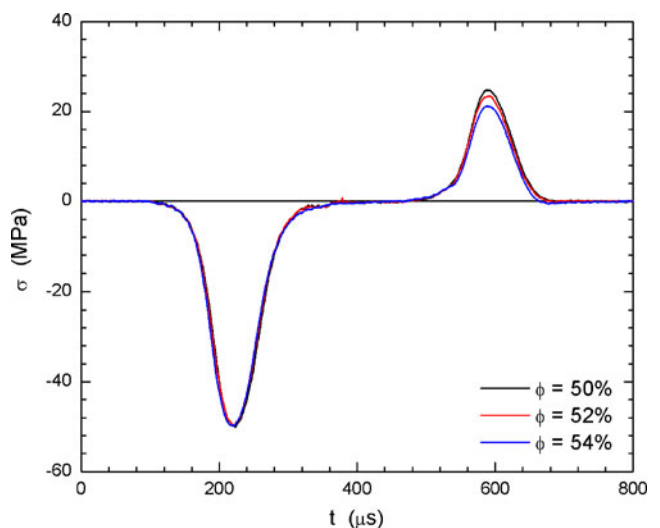
Fig. 14 Incident stress pulses for SHPB experiments on 50, 52 and 54 particle vol.% STFs

Fig. 15 Mechanical responses for 50, 52 and 54 vol.% particle suspensions (same as above)

(a) Stress-strain response
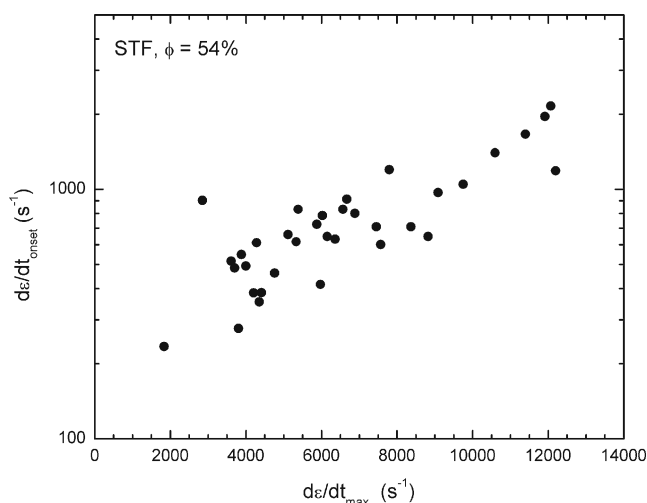
(b) Stress-strain rate response
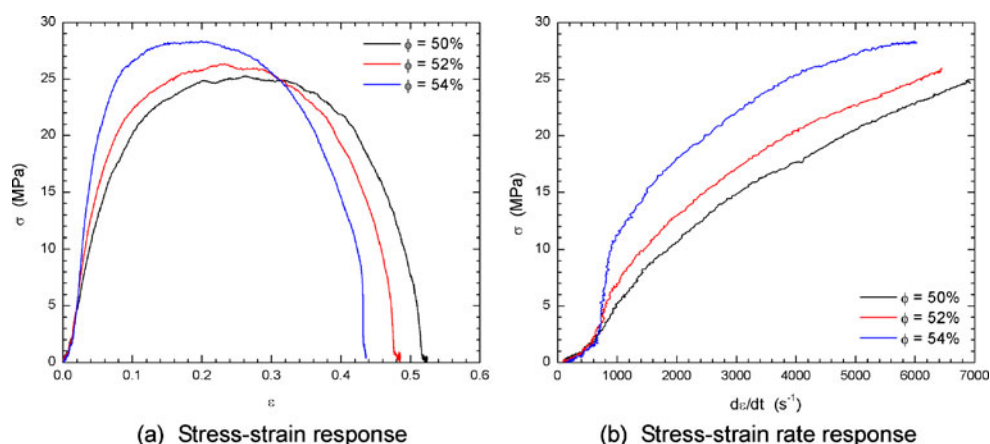
transition is triggered by the application of a critical strain, a critical stress, or is brought on by a critical loading rate or some combination of the above.

To address the issue of whether the shear thickening transition is brought on by strain, strain rate, or stress, we examine the effect of loading rate on the critical compressive strain rate (Fig. 14) compressive strain (Fig. 15), and compressive stress (Fig. 16) at the onset of transition. Toward this end, the critical strain rate, strain, and stress are plotted for every experiment performed on the 54% suspension as a function of compressive strain rate. In Fig. 15, the compressive strain within the suspension at the onset of transition is plotted for each experiment as a function of the maximum compressive strain rate achieved.

The only variable which appears constant through the range of compressive strain rates evaluated is the total compressive strain at the onset of transition. Note that this value of compressive strain corresponds to a maximum wall shear strain of order 10% under the

assumption of squeeze flow at constant viscosity (Lim et al. 2009). Earlier work by Lee and Wagner (2003) demonstrated that reports of a critical minimum shear strain for shear thickening under LAOS experiments were a result of slip at the tool–sample interface and that the critical strain amplitude decreased with increasing frequency. The highest frequencies probed were on the order of 10 Hz, which correspond to substantially lower rates than the characteristic rates explored here. That the experiments show an approximate critical shear strain on the order of the lowest critical strains observed at the highest frequencies in the previous work is not surprising as some relative particle displacement is required to form the hydroclusters, which should be independent of rate at sufficiently high Peclet numbers where Brownian motion no longer plays a role in determining the particle microstructure. These experiments appear to be probing this terminal regime and suggest a characteristic minimum shear strain is necessary for shear thickening.

Conclusions

The transient response of a STF loaded under squeezing flow has been studied. It has been found that the shear thickening transition is evident in the compressive response under squeeze flow. The resultant compressive stress–strain rate curves also show a similar trend with particle volume fraction whereby the transition becomes more extreme, and even apparently discontinuous, with increasing particle volume fraction. For the most concentrated sample, which is discontinuously shear thickening, the transition time decreases logarithmically with the compressive rate of loading. Analysis of the data shows that there is an apparent minimum compressive strain of order 1–2% required for the transition. Under the assumption of no wall

Fig. 16 Compressive strain rate at the onset of thickening vs. maximum compressive strain rate for the 54 vol.% STF

slip, this demonstrates that there is a minimum strain required for shear thickening at high Peclet numbers. These results are particularly important for engineering STFs for applications where high rates are applied or short durations are experienced. Further work is required for reduction of the SHPB measurements to material properties as was done previously for Newtonian fluids. For these highly nonlinear fluids, this requires a robust constitutive model and/or independent measurements of the kinematics in the sample during deformation, which is the subject of ongoing research.

Appendix

Examining the results for the lower concentration suspensions ($\phi = 0.50$ and 0.52, Figs. 17 and 18), it is
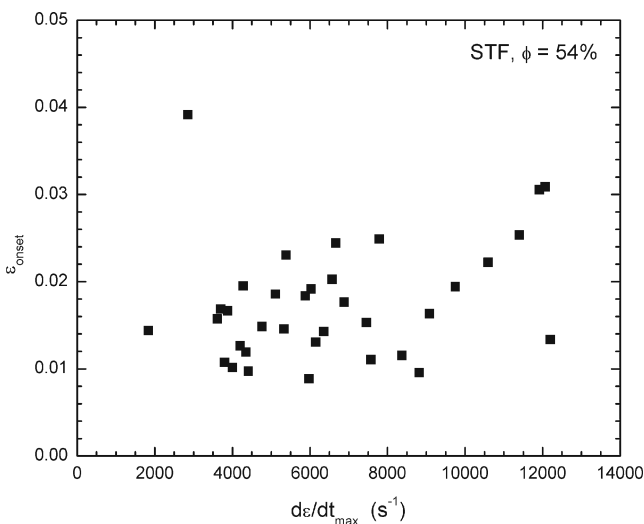
Fig. 17 Compressive strain at the onset of thickening vs. maximum compressive strain rate for the 54 vol.% STF
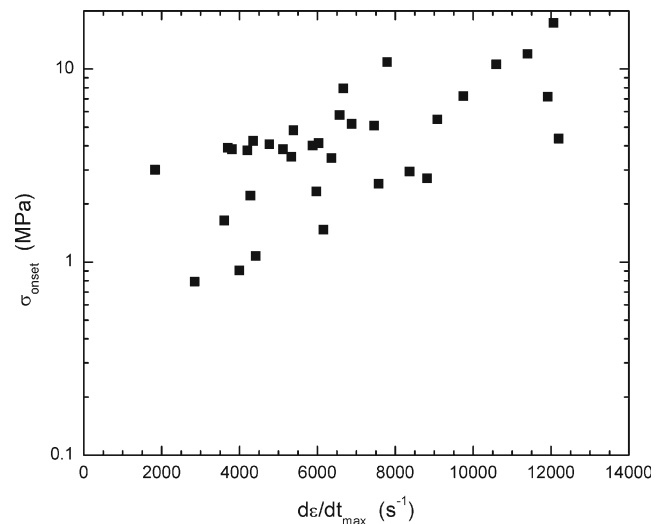
Fig. 18 Compressive stress at the onset of thickening vs. maximum compressive strain rate for the 54 vol.% STF

observed that these materials experience a weaker loading transition as compared to the more concentrated suspension. However, nonlinear behavior similar to the 0.54 volume fraction suspension is still evident. In Figs. 17 and 18, it can be noted that there is less stiffness in the post-transition material as the highest stresses achieved are generally lower for comparable strain rates.

Due to this lack of discontinuous behavior on the stress–strain rate plot, determining the transition time, as well as the strain at the onset of transition, is very difficult for the case of the 0.50 volume fraction silica suspension. In the case of the 0.52 silica suspension, it is possible to identify the strain at the onset of transition by analyzing the acceleration behavior during loading as seen in Fig. 10. While a decrease in acceleration does not typically occur for this volume fraction, a comparison of the strain at the point of inflection in the acceleration vs. time plot for these experiments has shown that strain at the onset of transition corresponds well with that for the 0.54 silica suspension.

References

Åhrström B, Lindqvist S, Höglund E, Sundin K (2002) Modified split Hopkinson pressure bar method for determination of the dilatation–pressure relationship of lubricants used in elastohydrodynamic lubrication. Proc Inst Mech Eng, Part J J Eng Tribol 216(J2):63–73

Barnes HA (1989) Shear-thickening ("dilatancy") in suspensions of Nonaggregating solid particles dispersed in Newtonian liquids. J Rheol 33(2):329–366

Bender JW, Wagner NJ (1995) Optical measurement of the contributions of colloidal forces to the rheology of concentrated suspensions. J Colloid Interface Sci 172:171–184

Bender JW, Wagner NJ (1996) Reversible shear thickening in monodisperse and bidisperse colloidal dispersions. J Rheol 40(5):899–916

Boersma WH, Laven J, Stein HN (1990) Shear thickening (dilatancy) in concentrated dispersions. AIChE J 36(3):321–332

Brady JF, Bossis G (1988) Stokesian dynamics. Annu Rev Fluid Mech 20:111–157

Clyens S, Evans C, Johnson K (1982) Measurement of the viscosity of supercooled liquids at high shear rates with a Hopkinson torsion bar. Proc R Soc Lond A 381:195–214

Coussot P, Wagner NJ (2009) The future of suspension rheophysics: comments on the 2008 workshop. Rheol Acta 48(8):827–829

D'Haene P, Mewis J, Fuller GG (1993) Scattering dichroism measurements of flow-induced structure of a shear thickening suspension. J Colloid Interface Sci 156:350–358

Decker MJ, Halbach CJ, Nam CH, Wagner NJ, Wetzel ED (2007) Stab resistance of shear thickening fluid (STF)-treated fabrics. Compos Sci Technol 67:565–578

Fischer C, Braun SA, Bourban P-E, Michaud V, Plummer CJG, Månson J-AE (2006) Dynamic properties of sandwich structures with integrated shear-thickening fluids. Smart Mater Struct 15:1467–1475. doi:10.1088/0964-1726/15/5/036

Gama BA (2004) Split Hopkinson pressure bar technique: experiments, analyses and applications. Dissertation, University of Delaware

Gama BA, Lopatnikov SL, Gillespie JW Jr (2004) Hopkinson bar experimental technique: a critical review. Appl Mech Rev 57(4):223–250

Grey GT III (2000) Classic split-Hopkinson pressure bar testing. In: ASM handbook 8 mechanical testing and evaluation, pp 488–496

Helber R, Doncker F, Bung R (1990) Vibration attenuation by passive stiffness switching mounts. J Sound Vib 138(1):47–57

Hiemenz PC, Rajagopalan R (1997) Principles of colloid and surface chemistry, 3rd edn. Marcel Dekker, Inc., New York

Hoffman RL (1972) Discontinuous and dilatant viscosity behavior in concentrated suspensions. I. Observation of a flow instability. Trans Soc Rheol 16(1):155–173

Hoffman RL (1974) Discontinuous and dilatant viscosity behavior in concentrated suspensions. II. Theory and experimental tests. J Colloid Interface Sci 46(3):491–506

Hoglund E, Larsson R (1997) Modeling non-steady EHL with focus on lubricant density. Elastohydrodynamics 32:511–521

Kaffashi B, O'Brien VT, Mackay ME, Underwood SM (1997) Elastic-like and viscous-like components of the shear viscosity for nearly hard sphere, Brownian suspensions. J Colloid Interface Sci 187:22–28

Kalman DP, Wagner NJ (2009) Microstructure of shear-thickening concentrated suspensions determined by flow-USANS. Rheol Acta 48(8):897–908

Kenner VH (1980) The fluid Hopkinson bar. Exp Mech 20(7):226–232

Kolsky H (1949) An investigation of the mechanical properties of materials at very high rates of loading. Proc Phys Soc 62(II-B):676–700

Kuzma D (1967) Fluid inertia effects in squeeze films. Appl Sci Res 18:15–20

Larson RG (1999) The structure and rheology of complex fluids. Oxford University Press, Inc., New York

Laun HM, Bung R, Schmidt F (1991) Rheology of extremely shear thickening polymer dispersions (passively viscosity switching fluids). J Rheol 35(6):999–1034

Laun HM, Bung R, Hess S, Loose W, Hess O, Hahn K, Hädicke E, Hingmann R, Schimdt F, Linder P (1992) Rheological and small angle neutron scattering investigation of shear-induced particle structures of concentrated polymer dispersions submitted to plane Poiseuille and Couette flow. J Rheol 36(4):743–787

Lee YS, Wagner NJ (2003) Dynamic properties of shear thickening colloidal suspensions. Rheol Acta 42:199–208. doi:10.1007/s00397-002-0290-7

Lee YS, Wetzel ED, Wagner NJ (2003) The ballistic impact characteristics of Kevlar woven fabrics impregnated with a colloidal shear thickening fluid. J Mater Sci 38:2825–2833

Li Z, Lambros J (1999) Determination of the dynamic response of brittle composites by the use of the split Hopkinson pressure bar. Compos Sci Technol 59:1097–1107

Lim AS, Gama BA, Gillespie JW Jr (2008a) Implementing the split-Hopkinson pressure bar technique for shear thickening fluid evaluation. In: Proceedings of the society of rheology, Monterey, CA

Lim AS, Lopatnikov SL, Gillespie JW Jr (2008b) Implementing the split-Hopkinson pressure bar technique for viscous fluid evaluation. In: Proceedings of the society for experimental mechanics, Orlando, FL

Lim AS, Lopatnikov SL, Gillespie JW Jr (2009) Development of the split-Hopkinson pressure bar technique for viscous fluid characterization. Polym Test 28:891–900. doi:10.1016/j.polymertesting.2009.08.002

Lynch CT (ed) (1980) CRC Handbook of materials science, vol 1. CRC Press, Cleveland

Maranzano BJ, Wagner NJ (2001a) The effects of interparticle interactions and particle size on reversible shear thickening: hard-sphere colloidal dispersions. J Rheol 45(5):1205–1222

Maranzano BJ, Wagner NJ (2001b) The effects of particle-size on reversible shear thickening of concentrated colloidal dispersions. J Chem Phys 114(23):10514–10527

Maranzano BJ, Wagner NJ (2002) Flow-small angle neutron scattering measurements of colloidal dispersion microstructure evolution through the shear thickening transition. J Chem Phys 117(22):10291–10302. doi:10.1063/1.1519253

O'Brien VT, Mackay ME (2000) Stress components and shear thickening of concentrated hard sphere suspensions. Langmuir 16:7931–7938. doi:10.1021/la000050h

Ogawa K (2003) Dynamic behavior of viscous fluid at high rate of shear using through bar method. J Phys IV France 110:435–440

Ravichandran G, Subhash G (1994) Evaluation of ceramic specimen geometries used in split Hopkinson pressure bar. DYMAT J I:193–210

Robinovitch SN, Hayes WC, McMahon TA (1995) Energy-shunting hip padding system attenuates femoral impact force in a simulated fall. J Biochem Eng 117:409–413

Sasahara K, Sakurai M, Nitta K (1998) Volume and compressibility changes for short poly(ethylene glycol)-water system at various temperatures. Colloid Polym Sci 276(7):643–647

Tan VBC, Tay TE, Teo WK (2005) Strengthening fabric armour with silica colloidal suspensions. Int J Solids Struct 42:1561–1576

Vermant J, Solomon MJ (2005) Flow-induced structure in colloidal suspensions. J Phys Condens Matter 17:R187–R216. doi:10.1088/0953-8984/17/4/R02

Mechanical Behavior of Silica Nanoparticle-Impregnated Kevlar Fabrics

Zhaoxu Dong, James M. Manimala and C. T. Sun*

School of Aeronautics and Astronautics, Purdue University,

West Lafayette, IN 47907-2045, USA

Abstract

This study presents the development of a constitutive model for in-plane mechanical behavior of five styles of plain woven Kevlar fabrics impregnated with silica nanoparticles. The neat fabrics differed in fiber type, yarn count, denier, weave tightness and strength. 4, 8, 16 and 24% by weight of nanoparticles were added to enhance the mechanical properties of the fabric. It was found that fabrics impregnated with nanoparticles exhibit significant improvement in shear stiffness and a slight increase in tensile stiffness along the yarn directions over their neat counterparts. A constitutive model was developed to characterize the nonlinear anisotropic properties of nanoparticle-impregnated fabrics undergoing large shear deformation. The constitutive model parameters were determined based on uniaxial (along yarn directions) and 45° off-axis tension tests. This constitutive model was incorporated in the commercial FEA software ABAQUS through a user-defined material subroutine to simulate various load cases.

Keywords: Kevlar fabric, soft armor, nanoparticle, constitutive model

1. Introduction

Kevlar[®] fiber is a high modulus, high strength and low density para-aramid synthetic fiber. In comparison to high strength steel, Kevlar has much better strength to weight ratio. It is a good candidate for use as a soft body protection material. The fibers are tightly woven into fabrics and multiple layers of fabrics are used in many soft body armors. The primary goal of soft armor design is to reduce the weight while maintaining the protection level. Hence, weight and performance are the two major criteria that must be balanced in selecting soft body armors.

---

*Corresponding author. Tel.: +1-765-494-5130; Fax: +1-765-494-0307.

E-mail address: sun@purdue.edu (C. T. Sun).

The mechanical behavior of Kevlar fabrics under uniaxial tensile loading has been extensively studied previously. Raftenberg and Mulkern (2002) performed uniaxial tension tests on Kevlar KM2 yarn and fabric to obtain stress versus displacement curves. They also obtained bilinear, exponential and quartic least square error fits to the data. The shear response of E-glass fabrics of various weave styles was studied by Mohammed et al. (2000) using picture frame tests. The locking angle was determined for each type of weave. A material model based on the theory of elasticity including the effect of fiber inextensibility was applied to analyze the experimental data and a microstructural analysis was done to predict the shear locking angle. Peng et al. (2004) address the issue of comparing fabric shear test data obtained from different testing methods. It was found that the normalization method to be employed depended on the experimental configuration of the test. Lomov et al. (2006) investigated the factors affecting the validity of data obtained from picture frame tests on glass/PP woven fabrics. They also report that yarn pretension caused difference in the shear resistance measured for the fabric. Controlling the pretension in the yarn during sample preparation and standardizing testing procedures were recommended to obtain more accurate shear response using the picture frame test. Harrison et al. (2004), Lebrun et al. (2003) and Milani et al. (2009) have done comparative studies on the evaluation of the in-plane shear behavior of fabrics using the bias extension and the picture frame tests.

Researchers have been continuously looking for ways to lighten body armors without compromising on performance. One way is to create stronger and lighter fibers by producing new materials and processes. Another method is to tailor the structure and composition of existing fabrics to achieve better performance. Lee et al. (2003) reported a significant enhancement in ballistic performance of Kevlar woven fabrics when impregnated with a shear thickening fluid (STF). The STF used was a colloid of ethylene glycol and highly concentrated silica nanoparticles. The viscosity of the STF increases significantly above a critical shear rate. This novel STF-fabric material offers good ballistic resistance and flexibility. However, the enhancement mechanisms and the exact role of STF in strengthening the fabric are still not well understood. Egres et al. (2004) demonstrated that STF Kevlar fabrics offered better stab resistance properties than neat Kevlar by restricting the yarn mobility. Tan et al. (2005) impregnated Twaron® fabrics with a water based silica colloid. Improvement in ballistic

resistance was observed, and they attributed it to the increase in projectile-fabric and inter-yarn friction.

Many different approaches like simplified orthogonal pin-jointed bars to model yarns, unit cell based models, equivalent homogenized continuum models and detailed 3D models incorporating individual yarns and weave patterns with contact definitions have been used to analyze and model woven fabric material behavior. King et al. (2005) developed a continuum constitutive model for woven fabrics in which the fabric yarn structural configuration is related to the macroscopic deformation through an energy minimization method. Lin et al. (2009) developed a finite element model to predict the shear force versus shear angle response of a plain woven fabric. The fabric was modeled at the yarn scale by assuming yarn behavior to be that of a 3D orthotropic solid. In a recent study by Grujicic et al. (2009), a meso-scale (yarn level) unit cell was developed and its properties were used to model plain woven Kevlar 129 fabric as a continuum surface via a user-defined material subroutine in ABAQUS. The properties of the unit cell were obtained from contact forces and shear response of a solid FEM model of cross yarns in a single unit cell.

In the present study, dry silica nanoparticles were used to reinforce Kevlar fabrics. Unlike the STF-fabric material, these nanoparticle-fabric composites do not contain any fluid and thus minimizes the weight added to neat fabrics. Uniaxial and 45° off-axis tension tests were done to evaluate the in-plane mechanical properties of the fabrics using an MTS servo-hydraulic load frame. It was found that the nanoparticles significantly increased the in-plane shear stiffness, while only slightly influenced the tension behavior along yarn directions. All the tested fabrics exhibited highly nonlinear behavior in shear deformation and large relative rotations between cross yarns. A constitutive model was developed using a method similar to the classical laminated plate theory in conjunction with the incremental deformation approach to characterize the nonlinear anisotropic properties of nanoparticle-impregnated fabrics undergoing large deformation. This model was incorporated in the commercial FEA software ABAQUS via a user-defined material (UMAT) subroutine to simulate the mechanical response of Kevlar fabrics. Validation of the model was done by comparing the numerical results to experimental load displacement curves for a 30° off-axis tension test and static indentation tests. The simulations agree well with the experimental results until the onset of failure.

2. Experimental Methods

2.1 Material preparation

Five styles of Kevlar fabrics from Hexcel® were studied. The fabric specifications given by the manufacturer are listed in Table 1. These fabrics differ in fiber type, yarn size, yarn count, weave tightness, thickness, strength and weight. All the styles were, however, plain woven fabrics. Figure 1 shows the weave texture of these fabrics. K779 style has a fine, tight weave; K310 and K706 have medium weaves; K720 and K745 are thick and heavy styles with coarse and loose yarns. The fabric properties are sensitive to ultraviolet radiation and moisture absorption. Hence the fabric rolls were stored in a closed dry container and the samples were oven dried to remove ambient moisture prior to testing.

Plain woven fabrics have two orthogonal yarn directions (warp and weft) in the undeformed configuration (Figure 3a). Although the fabric is balanced and has the same yarn count in the warp and weft directions, their strengths are different. It is therefore necessary to identify them. If the selvage is still on the fabric, the yarns that are parallel to the selvage are the warp yarns (Figure 3a). Alternatively, the warp and weft yarns can be distinguished by their waviness. Due to the weaving process, the warp yarns have more waviness than the weft yarn. Figure 3b shows an extracted warp and weft yarn from K720 style fabric.

A water-based silica nanoparticle colloid (Snowtex® ST-ZL) marketed by Nissan Chemical was used to impregnate nanoparticles into the fabric. According to the manufacturer's specifications, the silica particle size was 70~100 nm and the particle concentration was 40~41% by weight. To impregnate the silica nanoparticles into the fabric, a square piece of fabric of dimensions 150x150 mm was cut from the bulk fabric roll. The weight of the fabric was measured and recorded using an OHAUS® analytical balance. It was then soaked into the silica colloid and the percentage by weight of the solution added to the fabric was controlled. The soaked piece was oven dried at 80°C for 30 minutes to remove the water leaving silica nanoparticles adhered to the fabric. The final nanoparticle weight additions to the neat fabrics are controlled to be 4, 8, 16 and 24%. The resulting nanoparticle impregnated fabric remained quite flexible albeit not as much as the neat fabric. Figure 2 shows the SEM image of K706 with 24 wt% of silica nanoparticles. Samples were imaged with an FEI Nova nanoSEM field emission scanning electron microscope. The image was obtained using back-scatter detector in low

vacuum mode. The image reveals that silica nanoparticles did not form a uniform coating on the fabric surface but accumulated in the space between fibers. Abrading the surface of the treated fabric dislodges only the particles adhering to the surface but the particles in the inter-fiber spaces remain undisturbed.

2.2 Uniaxial tension tests

To evaluate the yarn direction stiffness of the fabrics, quasistatic uniaxial tension tests were performed on the neat and nanoparticle impregnated fabrics. The fabrics (single layer) with different wt% additions of nanoparticles were tested in both the warp and the weft directions. In order to prepare the specimens for the test, the neat and treated fabrics were cut into a rectangular piece of 25.4 mm in width and 150 mm in length along the yarn directions. Hard end tabs were bonded using epoxy adhesive to both ends leaving a gage length of 102 mm between the tabs. Figure 4(a) shows the dimensions of the final specimen. A 100 KN MTS load frame was used in this test. The crosshead speed was set to 0.1 mm/second. The specimen was aligned and gripped using hydraulic grips during the test. No slippage at the grips was noticed during testing.

2.3 Off-axis tension tests

Picture frame tests are widely used to evaluate the in-plane shear properties of woven fabrics (Mohammed et al. (2000), Peng et al. (2004) and Lomov et al. (2006)). The stress field in the picture frame is usually assumed to be uniform. When shear deformation is small, the fabric does not wrinkle and the uniform stress assumption is reasonable. However, the fabric wrinkles under large shear deformations. This results in nonuniform stress distributions and the accuracy of the test result is not guaranteed.

In view of the foregoing, we employed a 45° off-axis tension (bias extension) test to determine the fabric shear property. The specimen size was the same as that used in the uniaxial tension tests. Figures 4(b) and 4(c) show the initial and deformed configurations. The yarn orientation angle (α) is the acute angle made by the warp direction yarn with the short (25 mm) edge of the specimen as shown in the Figure 4(b). The specimens were cut such that this angle was 45° in the undeformed state. As the warp and weft directions in the fabric are orthogonal to each other initially, this test has a symmetric configuration with respect to both yarn directions. The specimens were tabbed and tested with same experimental setup as the uniaxial tension tests. No slippage at the grips was noticed during testing.

The uniaxial and the 45° off axis tension tests are used to obtain the material parameters for the constitutive model. In order to validate the model, one of the load cases used was a 30° off axis tension test. The test was done using K706 fabric style with the same specimen dimensions and test conditions as for the 45° off axis tension tests.

2.4 Indentation test

Under a transverse ballistic impact, the major mode of deformation in Kevlar fabrics is the out-of-plane displacement. Static indentation tests display certain correlations especially with regard to deformed profile, yarn pull-out behavior and indentor-yarn diameter size effects to the behavior of the fabric during ballistic impact. However, in ballistic tests, dynamic phenomena such as strain rate dependence and wave propagation effects become evident. To evaluate the accuracy of the proposed constitutive model, a static indentation test was done. The indentation test setup and specimen dimensions are schematically shown in Figure 5. A single layer of K706 Kevlar fabric with a yarn orientation angle of 45° was wrapped and clamped without slack between the grips of the test fixture such that two opposite edges are fixed and the other two edges are free. A hemispherical indentor of diameter 14 mm was pushed against the fabric at a crosshead speed of 0.1 mm/second using an MTS load frame and the load versus displacement response was recorded. No slippage at the gripped edges was noticed until onset of failure. Figure 6 shows an indentation test in progress.

3. Experimental Results

3.1 Uniaxial tension tests

The uniaxial tension tests for the fabrics show two distinct regimes in the load displacement plots. In the initial loading phase the fabric has a linear behavior with low modulus. The axial strain occurs during this phase primarily because of the uncrimping of the axial yarns in the woven fabric. In the absence of any applied transverse tension, the actual phenomenon is one of crimp interchange whereby the axial yarns get straightened while the transverse yarns take up additional crimp. However, once the axial yarns become uncrimped, the transverse yarns remain in position and no pullout is noticed. In the later loading phase the axial yarns undergo elongation with a relatively higher modulus. The yarn elongation response is also linear until the fabric fails by the breakage of axial yarns. The failure location depends on the location of any local defects but occurs at a definite load and is obtained consistently in repeated tests. The

6

uniaxial response is thus markedly bilinear. The results show that, in general, the weft yarns are stronger than the warp yarns and also display a stiffer response. The addition of nanoparticles to the fabrics seems to increase the uniaxial strength and stiffness only slightly as evidenced by the plots presented in Figure 7. Nonetheless, there are a few observations of interest that present themselves.

Firstly, as the deformation progresses, it is noticed that the width of the specimen remains more or less unchanged. Unlike a homogenous solid, the deformation in fabrics is largely governed by interaction between yarns at the cross over points in the weave. But once the crimp interchange process is complete after the initial loading phase, no transverse yarn pull out is noticed, which indicates that the width of the specimen (distance between outer most axial yarns) remains the same as the initial width of the specimen. This was noted to be the case for all the specimens tested and thus an assumption of negligible lateral contraction is made for the fabric loaded in uniaxial tension.

As the crimp interchange process reduces the yarn waviness in the axial direction while increasing it in the transverse direction, the variation of the overall thickness of the fabric is very small. Variability in the load sensed by individual axial yarns is reduced by ensuring high precision in the specimen fabrication process and alignment and gripping procedure for the test. However one of the factors affecting the scatter in the failure location (apart from any local defects) may be the slight difference in pretension induced due to errors in the aforesaid procedures. Owing to the existence of these conditions in the fabric during the uniaxial tension test, it is reasonable to assume a state of uniform axial stress and strain field. Hence, engineering stress versus strain can be reported using the initial specimen dimensions, which are presented in Figure 7. The thickness of woven fabrics is measured using ASTM D1777-96 standard. The thickness values as quoted by the manufacturer (Table 1) are used to calculate the fabric cross sectional area. The warp and weft fabric strengths as obtained from the tests (Table 2) differ from the manufacturer supplied values given in Table 1. The average difference between measured and supplied value is about 16%. As the manufacturer's test procedure is not supplied with the material data sheet, the variation in the measured strength values is attributed to difference in test methods and conditions. The axial mechanical properties of the fabric are obtained from the test results using a bilinear curve fit. The strength values assume significance only in the context of failure prediction which is not dealt with in the present study.

Secondly, a comparison of the load displacement curves for various styles of fabrics shows a slight departure from the typical trend for certain styles. In general it is noted that the weft direction has lower strains to complete uncrimping, higher moduli in both load regimes and greater strength. This is explained by the fact that the weft yarns are much less wavy than warp yarns and as a consequence are fully uncrimped at lower strain values. The bilinear transition strain for most neat and treated fabric styles is between 0.01 and 0.03. However, K310 and K779 styles are exceptions. Among the five styles of fabric tested, K779 and K310 have the finest and the second finest weave respectively. Both these fabrics are tightly woven with very close yarn spacing. The steep rise in the weft direction load displacement curves for K310 and K779 is due to their fine weave which causes the yarn to become fully uncrimped at very low strains. This is less evident in the warp direction because of its relatively higher waviness.

The mechanism by which the addition of nanoparticles increases the stiffness of the fabric is conjectured to be due to increase in the friction between the yarns. As the nanoparticles are embedded in the inter-yarn and inter-fiber spaces, they restrict the relative yarn mobility. This effect becomes more pronounced in the case of fine weave fabrics in comparison to coarse weave as the nanoparticles are lodged in very small gaps between the tightly woven yarns. In the case of the warp direction response for K779, because of the high waviness and fine weave, the initial resistance to applied strain is due to a combination of elongation of the yarns and uncrimping as the nanoparticles lock the yarns in place relative to each other. Once the frictional resistance due to the nanoparticles is overcome a short plateau phase is observed when the uncrimping process is completed and thereafter the yarns undergo axial elongation alone until failure. This could be the reason for the high dependence of the initial load displacement response of weft direction K779 fabric on the percentage weight addition of nanoparticles.

3.2 Off-axis tension tests

The mechanical behavior exhibited by neat and treated fabrics in a 45° off axis tension test offer numerous insights. The load displacement curves are highly nonlinear and the addition of nanoparticles to the fabric causes a significant increase in its shear rigidity and failure strength. Figure 8 presents the load versus displacement plots for five styles of Kevlar fabrics with different wt% additions of nanoparticles.

In an off axis tension test, the deformation of the fabric is dependent on the specimen dimensions, yarn orientation angle, yarn count in warp and weft directions and the nanoparticle

loading of the fabric. For balanced plain woven Kevlar fabrics with the same yarn count in warp and weft directions, a 45° off axis tension (bias extension) test produces a deformation that is symmetric about the longitudinal centerline of the specimen (Figure 4(c)). Distinct shear regions are observed in the specimen during deformation (Harrison et al. (2004), Lebrun et al. (2003)). The central region C as shown in Figure 9 has a pure shear deformation as the yarns experience only rotations relative to each other, while the region A remains undeformed and region B has a shear angle half that in region C. Due to the rotation of the yarns, region C displays large transverse contraction. The length of region C depends on the specimen dimensions and yarn count of the fabric. The load displacement curves show a steep rise after a critical value of displacement is reached in each case. This occurs because as the yarn rotations progress, a limiting angle is reached when adjacent yarns become compactly packed without any inter-yarn spacing. This angle is referred to as the locking angle for fabrics. After the locking angle is reached the shear rigidity of the fabric is driven by the compression of individual yarns in the transverse direction which causes a greater load to be sensed per unit displacement. In the post locking deformation, out of plane wrinkling of the fabrics occur. Failure initiation occurs thereafter by the slipping of the yarns at the interface between shear regions C and B. Unlike the uniaxial tension test, the failure does not occur at a well defined load but progresses gradually as weft and warp yarns slip over each other at cross over points. The oscillatory behavior in the curves at displacements close to failure is due to this phenomenon of yarn sliding at corners. The maximum load is sensed during the yarn sliding phase after which the curve falls rapidly as the two portions of the specimen separate. The failure location was always observed to be at either the upper or lower shear region interfaces. The addition of nanoparticles did not affect the location of failure. However, treated fabrics display a more definite failure load as the enhanced load carrying ability diminishes rapidly once the nanoparticles that lock the relative motion between adjacent yarns are dislodged. This reinforces the inference that the nanoparticles enhance the shear rigidity by increasing the inter-yarn and intra-yarn friction in woven fabrics.

The load displacement plots (Figure 8) demonstrate that substantial enhancement of shear rigidity and strength is achieved by the addition of nanoparticles to the fabric. The effect is greater for coarse weave fabrics which have low rigidity in the neat condition. K745 (the coarsest weave among the five styles) registers a failure load of nearly 26 times that of its neat strength with an addition of 24 % by weight of nanoparticles. In comparison, fine weave fabrics that have

9

higher inter yarn friction in the neat state due to their smaller yarn size and inter-yarn spacing, show lower sensitivity to the percentage of nanoparticles added. K779 for example, shows a proportional increase in stiffness with increase in the amount of nanoparticles added but the failure load remains more or less the same. It is surmised that the impregnation of nanoparticles in the fabric imparts an additional mechanism of frictional interaction between the yarns which acts in conjunction with the inherent inter-yarn friction present in neat fabrics. In the case of fine weave fabrics like K779, the effect of the neat fabric friction is predominant and hence the fabric shows lower increase in failure load with increase in nanoparticle addition. The fabric styles K310, K706 and K720 show varying degrees of increase in shear rigidity and failure loads. An important factor that influences the behavior of silica nanoparticle impregnated fabrics is the uniformity of the distribution of nanoparticles in the fabric. Although, the process is controlled to ensure that the nanoparticle colloid soaks the fabric evenly and remains undisturbed during the drying process, SEM images reveal that there is agglomeration of particles in inter-yarn spaces. Hence, to a certain extent, variability in the failure load of the fabric may be attributed to the non uniform distribution of nanoparticles in the fabric.

3.3 Indentation test

Indentation test was conducted for validation of the constitutive model. The deformation and failure of Kevlar fabrics in a static indentation test depends on the fabric style, indentor size and boundary conditions. As a 45° yarn orientation was used, large out of plane deformation occurs before failure initiation. Unlike the off axis tension test, the yarn rotations in the specimen are not uniform. The indentor load is initially small as the out of plane deformation is accommodated by uncrimping of yarns. Once the rotations of the yarns are close to the locking value, a steep rise in the indentor load is noticed. Further transverse displacement leads to the onset of failure by the sliding (unraveling) of yarns at cross over points at the corner of the clamped edges of the specimen.

4. Constitutive modeling

The uniaxial and off axis tension tests reveal that Kevlar fabrics have very high stiffness in both yarn directions, but a very low in-plane shear resistance. Addition of nanoparticles produces a substantial increase in shear rigidity while only a small increase is obtained in the axial stiffness. The tensile strains in yarn directions are small because of high stiffness in these directions.

However, an in-plane shear loading can cause very large changes in the angle between the warp and weft yarns due to their relative rotations. This behavior makes the modeling of the fabric as a homogenized continuum rather difficult. In addition, for nanoparticle impregnated fabrics, the effect of the nanoparticles on the mechanical behavior must be included in the constitutive equations.

To simplify this task, we adopt an incremental deformation approach in setting up the constitutive model in conjunction with a procedure that resembles the classical laminated plate theory. As the response of the fabrics is highly non linear, an incremental deformation approach is used. At every increment, the fabric deforms through the interaction of the warp and weft families of yarns. This interaction is simplified by modeling the warp and weft yarns as two separate plies in a composite laminate. Once the incremental constitutive equations are established, they can be implemented as a user defined subroutine in the commercial finite element code ABAQUS/ Standard to perform numerical simulations.

A set of coordinate systems are established as shown in Figure 10. The fabric is assumed to lie in the *x-y* plane with the warp and weft yarns initially assumed to be oriented at angles α and β respectively to the positive *x* direction of the global coordinate system *x-y*. An angle measured anticlockwise from the positive *x* direction is represented as positive and an angle measured clockwise is represented as negative. As the out of plane thickness of the fabric is very small compared to the specimen in-plane dimensions, an assumption of a state of plane stress is made. For plain woven fabrics the warp and weft directions are orthogonal to each other in the undeformed condition. As the fabric undergoes large shear deformations, the yarns rotate relative to each other and the angle between them in the deformed state *(θ)* can become much larger or smaller than 90°. Two local coordinate systems, *(x$_1$-x$_2$)$_\alpha$* and *(x$_1$-x$_2$)$_\beta$* are established for the warp and the weft layers respectively such that the x_1 direction is along the yarn direction in each layer.

At each incremental step, a single layer of Kevlar fabric of thickness *T* is modeled as the composite of two layers of unidirectional fibers. The effective mechanical properties of each layer are modeled as a two-dimensional orthotropic solid and the fabric is modeled as the laminate consisting of two fiber layers. Considering the warp layer, the incremental stress-strain relations for this layer are formulated in the local coordinate system as

$$\begin{Bmatrix} \Delta\sigma_{11} \\ \Delta\sigma_{22} \\ \Delta\sigma_{12} \end{Bmatrix} = \begin{bmatrix} \dfrac{E_1^\alpha}{1-v_{12}v_{21}} & \dfrac{v_{12}^\alpha E_2^\alpha}{1-v_{12}^\alpha v_{21}^\alpha} & 0 \\[2ex] \dfrac{v_{12}^\alpha E_2^\alpha}{1-v_{12}^\alpha v_{21}^\alpha} & \dfrac{E_2^\alpha}{1-v_{12}^\alpha v_{21}^\alpha} & 0 \\[2ex] 0 & 0 & G_{12}^\alpha \end{bmatrix} \begin{Bmatrix} \Delta\varepsilon_{11} \\ \Delta\varepsilon_{22} \\ \Delta\gamma_{12} \end{Bmatrix} \tag{1}$$

where the superscript α denotes the warp layer and E_1^α, E_2^α and v_{12}^α are the yarn direction modulus, transverse modulus and in-plane Poisson's ratio for the layer. The uniaxial tension tests show that for an applied tensile load in the yarn directions, the fabric structure does not have any overall contraction in the transverse direction. The yarns themselves (which are formed by bundles of fibers) may contract leading to an increase in the free space between yarns, but the overall transverse dimension of the specimen remains unchanged. Thus from a continuum perspective, the in-plane Poisson's ratio for a layer of unidirectional yarns (warp or weft) is negligible and is set to zero which simplifies equation (1) to

$$\begin{Bmatrix} \Delta\sigma_{11} \\ \Delta\sigma_{22} \\ \Delta\sigma_{12} \end{Bmatrix} = \begin{bmatrix} E_1^\alpha & 0 & 0 \\ 0 & E_2^\alpha & 0 \\ 0 & 0 & G_{12}^\alpha \end{bmatrix} \begin{Bmatrix} \Delta\varepsilon_{11} \\ \Delta\varepsilon_{22} \\ \Delta\gamma_{12} \end{Bmatrix} \tag{2}$$

The incremental stress-strain relations for the warp layer in the global coordinate system x-y can now be obtained using coordinate transformation as

$$\begin{Bmatrix} \Delta\sigma_{xx} \\ \Delta\sigma_{yy} \\ \Delta\sigma_{xy} \end{Bmatrix} = \begin{bmatrix} Q_{11}^\alpha & Q_{12}^\alpha & Q_{16}^\alpha \\ Q_{12}^\alpha & Q_{22}^\alpha & Q_{26}^\alpha \\ Q_{16}^\alpha & Q_{26}^\alpha & Q_{66}^\alpha \end{bmatrix} \begin{Bmatrix} \Delta\varepsilon_{xx} \\ \Delta\varepsilon_{yy} \\ \Delta\gamma_{xy} \end{Bmatrix} = \begin{bmatrix} Q^\alpha \end{bmatrix} \begin{Bmatrix} \Delta\varepsilon_{xx} \\ \Delta\varepsilon_{yy} \\ \Delta\gamma_{xy} \end{Bmatrix} \tag{3}$$

where the reduced stiffnesses for the warp layer, Q_{ij}^α are given by

$$\begin{aligned}
Q_{11}^\alpha &= E_1^\alpha \cos^4\alpha + 4G_{12}^\alpha \sin^2\alpha\cos^2\alpha + E_2^\alpha \sin^4\alpha \\
Q_{12}^\alpha &= \left(E_1^\alpha + E_2^\alpha - 4G_{12}^\alpha\right)\sin^2\alpha\cos^2\alpha \\
Q_{22}^\alpha &= E_1^\alpha \sin^4\alpha + 4G_{12}^\alpha \sin^2\alpha\cos^2\alpha + E_2^\alpha \cos^4\alpha \\
Q_{16}^\alpha &= \left(E_1^\alpha - 2G_{12}^\alpha\right)\sin\alpha\cos^3\alpha - \left(E_2^\alpha - 2G_{12}^\alpha\right)\sin^3\alpha\cos\alpha \\
Q_{26}^\alpha &= \left(E_1^\alpha - 2G_{12}^\alpha\right)\sin^3\alpha\cos\alpha - \left(E_2^\alpha - 2G_{12}^\alpha\right)\sin\alpha\cos^3\alpha \\
Q_{66}^\alpha &= \left(E_1^\alpha + E_2^\alpha - 2G_{12}^\alpha\right)\sin^2\alpha\cos^2\alpha + G_{12}^\alpha\left(\sin^4\alpha + \cos^4\alpha\right)
\end{aligned} \tag{4}$$

Similarly the incremental stress-strain relations in the global coordinate system for the weft layer are obtained as

$$\begin{Bmatrix} \Delta\sigma_{xx} \\ \Delta\sigma_{yy} \\ \Delta\sigma_{xy} \end{Bmatrix} = \begin{bmatrix} Q_{11}^{\beta} & Q_{12}^{\beta} & Q_{16}^{\beta} \\ Q_{12}^{\beta} & Q_{22}^{\beta} & Q_{26}^{\beta} \\ Q_{16}^{\beta} & Q_{26}^{\beta} & Q_{66}^{\beta} \end{bmatrix} \begin{Bmatrix} \Delta\varepsilon_{xx} \\ \Delta\varepsilon_{yy} \\ \Delta\gamma_{xy} \end{Bmatrix} = \begin{bmatrix} Q^{\beta} \end{bmatrix} \begin{Bmatrix} \Delta\varepsilon_{xx} \\ \Delta\varepsilon_{yy} \\ \Delta\gamma_{xy} \end{Bmatrix} \tag{5}$$

The superscript β denotes the weft layer and the reduced stiffnesses for the weft layer, $Q_{ij}{}^{\beta}$ are given by

$$Q_{11}^{\beta} = E_1^{\beta}\cos^4\beta + 4G_{12}^{\beta}\sin^2\beta\cos^2\beta + E_2^{\alpha}\sin^4\beta$$

$$Q_{12}^{\beta} = \left(E_1^{\beta} + E_2^{\beta} - 4G_{12}^{\beta}\right)\sin^2\beta\cos^2\beta$$

$$Q_{22}^{\beta} = E_1^{\beta}\sin^4\beta + 4G_{12}^{\beta}\sin^2\beta\cos^2\beta + E_2^{\beta}\cos^4\beta$$

$$Q_{16}^{\beta} = \left(E_1^{\beta} - 2G_{12}^{\beta}\right)\sin\beta\cos^3\beta - \left(E_2^{\beta} - 2G_{12}^{\beta}\right)\sin^3\beta\cos\beta \tag{6}$$

$$Q_{26}^{\beta} = \left(E_1^{\beta} - 2G_{12}^{\beta}\right)\sin^3\beta\cos\beta - \left(E_2^{\beta} - 2G_{12}^{\beta}\right)\sin\beta\cos^3\beta$$

$$Q_{66}^{\beta} = \left(E_1^{\beta} + E_2^{\beta} - 2G_{12}^{\beta}\right)\sin^2\beta\cos^2\beta + G_{12}^{\beta}\left(\sin^4\beta + \cos^4\beta\right)$$

The warp and weft layers exist in an interwoven state in the actual fabric and hence to simplify the formulation, we assume that both layers occupy the same space and have the same thickness *(T)* which is the thickness of one fabric layer. This thickness is set to be constant over the fabric undergoing large deformation. To be consistent, material properties for the warp and weft layers are defined using the thickness. Thus, the stiffness matrix for the fabric is obtained as

$$[Q] = \begin{bmatrix} Q^{\alpha} \end{bmatrix} + \begin{bmatrix} Q^{\beta} \end{bmatrix} \tag{7}$$

Equation (7) provides the stiffness matrix for a single layer of fabric which is dependent on a total of six unknown material parameters – three each for warp and weft yarn directions. For each layer, the moduli E_1, E_2 and G_{12} are calibrated from the uniaxial and off-axis tension tests. These moduli must reflect the variation in yarn spacing under large deformations due to relative rotation of warp and weft yarns. True strain and true stress are used in the ABAQUS incremental formulation. In the following discussion, neat Kevlar K706 style fabric will be used as an example to illustrate the procedure for obtaining the material parameters. The same procedure is followed for other styles of neat and treated fabrics.

The uniaxial tension tests in the warp and weft directions display a bilinear trend. Hence, a simple bilinear function was used to approximate the tangent longitudinal moduli $E_1{}^{\alpha}$ and $E_1{}^{\beta}$ in the warp and weft directions from these stress-strain curves. In the uniaxial tension tests, relative yarn rotations do not occur and thus the yarn spacing remains unchanged. However, when the fabric undergoes shear deformations, yarn rotations induce a change in the tangent longitudinal

moduli. In order to capture this effect, the approximate bilinear functions for the tangent longitudinal moduli are factored by a non-dimensional yarn spacing parameter which is defined as follows. Figure 11 shows the configuration of the yarns in the initial and deformed configurations. The yarn spacing parameters L_α and L_β for the warp and weft directions respectively are defined as the ratio between the yarn spacing in the deformed configuration *(l_α and l_β)* to the initial yarn spacing *($l_{\alpha o}$ and $l_{\beta o}$)*.

$$L_\alpha = \frac{l_\alpha}{l_{\alpha o}}$$

$$L_\beta = \frac{l_\beta}{l_{\beta o}} \tag{8}$$

The non-dimensional yarn spacing parameters are equal to 1 in the initial configuration. In the deformed configuration they are obtained from the geometry as a function of the yarn direction strains $\varepsilon_{11}{}^\alpha$ and $\varepsilon_{11}{}^\beta$ and the angle between the yarns *($\theta=\alpha-\beta$)* as

$$L_\alpha = \frac{l_\alpha}{l_{\alpha o}} = \left(1 + \varepsilon_{11}^\beta\right) \sin\theta$$

$$L_\beta = \frac{l_\beta}{l_{\beta o}} = (1 + \varepsilon_{11}^\alpha) \sin\theta \tag{9}$$

Initially, as the yarn direction strains are zero and the angle between the yarns is $\pi/2$, the values of L_α and L_β become 1, which is consistent with the definition of the yarn spacing parameters. Using the yarn spacing parameters, the tangent longitudinal moduli at each increment are approximated by

$$E_1^\alpha = \frac{1}{L_\alpha} \begin{cases} E_1^{\alpha 1}, \varepsilon_{11}^\alpha \leq \varepsilon_{11}^{\alpha 0} \\ E_1^{\alpha 2}, \varepsilon_{11}^\alpha > \varepsilon_{11}^{\alpha 0} \end{cases}$$

$$E_1^\beta = \frac{1}{L_\beta} \begin{cases} E_1^{\beta 1}, \varepsilon_{11}^\beta \leq \varepsilon_{11}^{\beta 0} \\ E_1^{\beta 2}, \varepsilon_{11}^\beta > \varepsilon_{11}^{\beta 0} \end{cases} \tag{10}$$

where the superscript '0' indicates the bilinear transition strain. For neat K706 style fabric, the values of the various constant material parameters in equation (10) are obtained from linear curve fits to the uncrimping and elongation regimes of the warp and weft direction stress-strain curves as

$$E_1^{\alpha 1} = 1.5 \text{ GPa}, E_1^{\alpha 2} = 22.0 \text{ GPa}, \varepsilon_{11}^{\alpha 0} = 0.025$$

$$E_1^{\beta 1} = 1.8 \text{ GPa}, E_1^{\beta 2} = 23.0 \text{ GPa}, \varepsilon_{11}^{\beta 0} = 0.016 \tag{11}$$

When the yarns undergo rotations due to shear deformations, the yarn spacing reduces. This

causes the yarn spacing parameter to decrease. Thus, the tangent longitudinal moduli which are inversely proportional to the yarn spacing parameters increase as the yarn spacing reduces. This reflects the phenomenon of increase in yarn direction moduli due to increase in friction between adjacent yarns as they become closely packed.

The transverse moduli and the shear modulus are estimated from the 45° off axis tension tests. The mechanism by which the fabric resists shear loads transitions from one predominantly due to rotation of yarns to one due to the transverse compression of adjacent yarns as the relative angle between the yarns approaches the locking angle. Hence, the shear rigidity is very low during the initial phase of the deformation. Once the locking angle is reached, the yarns become closely packed and further deformation is resisted by compression of yarns in the transverse direction and the occurrence of out of plane wrinkling. We introduce this effect into the constitutive relations by assuming that the shear modulus (which is attributed to the initial yarn rotations) to be constant and that the highly non linear behavior at higher displacements are caused by variation in the transverse moduli. The load-displacement curves for the 45° off axis tension test can be converted to an equivalent shear stress-shear angle curve using the kinematic relations for an equivalent picture frame test (Milani et al. (2009)). Comparisons show that both these curves have nearly the same slope at low values of displacement/ strain. Under these assumptions, the shear modulus is estimated from the initial slope of the load-displacement curves from off axis tension tests. The individual shear moduli for the warp and weft layers are indistinguishable. Both $G_{12}{}^\alpha$ and $G_{12}{}^\beta$ are assumed to be equal and to be the same as that of a single layer of fabric. For neat K706, the shear modulus is calculated from the initial slope of the curve as

$$G_{12}^\alpha = G_{12}^\beta = G_{12} = 0.4 \ MPa \tag{12}$$

The parameters $E_2{}^\alpha$ and $E_2{}^\beta$ are obtained from the load-displacement curves using a non linear fitting function which depends on the yarn spacing parameters. When the cross yarns undergo large rotation, the parallel yarns are packed together. The stresses in transverse direction prevent the parallel yarns from being too close to each other under large shear deformation. The tangent transverse moduli $E_2{}^\alpha$ and $E_2{}^\beta$ could be calculate from these transverse stresses. Since both $E_2{}^\alpha$ and $E_2{}^\beta$ attribute to prevent the further yarn rotation, we assume they are the same nonlinear function in terms of non-dimensional yarn spacing L_α and L_β. The form of the fitting

function is such that as the yarn spacing parameters tend towards a limiting value (L_{lock}), after which further yarn rotations cannot occur, the transverse moduli increase rapidly. The function and the constants E_2^0 and L_{lock} are found by means of a trial and error procedure using numerical simulations as

$$E_2^\alpha = \frac{E_2^0}{L_\alpha - L_{Lock}}, \quad E_2^\beta = \frac{E_2^0}{L_\beta - L_{Lock}}$$

$$E_2^0 = 2.3\ MPa, \quad L_{Lock} = 0.68 \tag{13}$$

Table 3 summarizes the material parameters estimated for five styles of neat and 24 wt% nanoparticle impregnated Kevlar fabrics. The mechanical properties of the five styles of fabrics are quite different. The material parameter G_{12} reflects the initial shear stiffness in the off-axis tension. Parameter E_2^0 provides the transverse stiffness which prevents the parallel yarns from being too close to each other. Both G_{12} and E_2^0 are directly related to the final shear rigidity under large deformation. Nanoparticles largely enhance the shear rigidity. Fabrics with nanoparticles have much larger values of both G_{12} and E_2^0.

5. Comparison of experimental and numerical results

The constitutive model was implemented as a user defined material sub routine (UMAT) in ABAQUS/ Standard. The rectangular fabric specimen was modeled using four noded plane stress shell elements. One edge was fixed and a prescribed displacement was applied to the opposite edge. Validation of the constitutive model is carried out by comparing the experimental result and the numerical simulation of the 30° off-axis tension test. Figure 12 shows the experimental load-displacement curves and the result of numerical simulations for 45° and 30° off axis tension tests using neat K706. Numerical simulations fit the experimental data very well until the onset of failure. Figure 13 shows the snapshot of deformed specimen at grip displacement of 18 mm. Only the upper half of the specimen is shown. The middle line which was horizontal before loading tilts gradually when grip moves. The simulated tilting angle is almost the same as the experimental one. Overall, the simulated specimen shape agrees well with the image taken from the experiments.

In the numerical simulation for the static indentation test, the indentor was modeled as a rigid body and a frictionless contact definition was given between the indentor and the fabric. The indentor load was measured from the out of plane reaction force. Comparison of the

experimental and numerical indentor load-displacement curves is presented in Figure 14. The numerical simulations fit the experimental data very well until failure of the fabric begins due to the slipping of yarns at the corners. Since this model does not account for damage, the simulation starts to deviate from the experimental results at large loads.

6. Conclusions

In-plane mechanical properties of five styles of Kevlar fabrics were investigated to show the difference between the neat fabric and the silica nanoparticle impregnated fabrics. The nanoparticles impart substantial increase to the in-plane shear rigidity. When off-axis load is applied, nanoparticle impregnated fabrics sustained higher failure loads. SEM images reveal that the nanoparticles are lodged in the inter-yarn and inter-fiber spaces in the fabric. This increases the friction between adjacent and cross yarns thereby augmenting the fabric's resistance to applied loads.

A two dimensional homogenized continuum constitutive model was developed to characterize the nonlinear anisotropic material properties of the neat and nanoparticle impregnated fabrics under large shear deformation. The material parameters required in this model were obtained from uniaxial tension and 45° off-axis tension tests. The constitutive model was interfaced with the commercial finite element code ABAQUS via a user defined material subroutine (UMAT). Validation of the model was done by simulating a 30° off-axis tension test and a static indentation test. The simulated load-displacement curves were found to agree very well with the experimental data. This model can be used to predict the load deflection behavior of neat and nanoparticle impregnated plain woven Kevlar fabrics with good accuracy.

Acknowledgement

References

R.G. Egres Jr., Y.S. Lee, J.E. Kirkwood, K.M. Kirkwood, E.D. Wetzel, N.J. Wagner, "Protective fabrics utilizing shear thickening fluids", *Proceedings of the Industrial Fabrics Association International (IFAI) 4th International Conference on Safety and Protective Fabrics*, Pittsburgh, PA, USA, October 27-29, 2004.

M. Grujicic, W. C. Bell, G. Arakere, T. He and B. A. Cheeseman, "A meso-scale unit-cell based material model for the single-ply flexible-fabric armor*", Materials and Design*, **30** (2009), 3690-3704.

P. Harrison, M.J. Clifford and A.C. Long, **"**Shear characterisation of viscous woven textile composites: a comparison between picture frame and bias extension experiments", *Composite Science and Technology*, **64** (2004), 1453–1465.

M.J. King, P. Jearanaisilawong, S. Socrate, "A continuum constitutive model for the mechanical behavior of woven fabrics", *International Journal of Solids and Structures*, **42** (2005), 3867-3896.

G. Lebrun, M.N. Bureau and J. Denault, "Evaluation of bias-extension and picture-frame test methods for the measurement of intraply shear properties of PP/glass commingled fabrics", *Composite Structures,* **61** (2003), 341–352.

Y.S. Lee, E.D. Wetzel and N.J. Wagner, "The ballistic impact characteristics of Kevlar woven fabrics impregnated with a colloidal shear thickening fluid", *Journal of Materials Science*, **38** (2003), 2825-2833.

H. Lin, M.J. Clifford, A.C. Long and M. Sherburn, "Finite element modeling of fabric shear", *Modelling and Simulation in Materials Science and Engineering*, **17** (2009).

S.V. Lomov, A. Willems, I. Verpoest, Y. Zhu, M. Barburski and Tz. Stoilova, "Picture frame test of woven composite reinforcements with a full-field strain registration", *Textile Research Journal*, **76**:3 (2006), p243-252.

A.S. Milani, J.A. Nemes, G. Lebrun and M.N. Bureau, "A Comparative analysis of a modified picture frame test for characterization of woven fabrics", *Polymer Composites*, (2009).

U. Mohammed, C. Lekakou, L. Dong and M.G. Bader, "Shear deformation and micromechanics of woven fabrics", *Composites: Part A*, **31** (2000), 299-308.

X.Q. Peng, J. Cao, J. Chen, P. Xue, D.S. Lussier, L. Liu, "Experimental and numerical analysis on normalization of picture frame tests for composite materials", *Composites Science and*

Technology, **64** (2004), 11-21.

M.N. Raftenberg and T.J. Mulkern, "Quasi-Static uniaxial tension characteristics of plain-woven Kevlar KM2 fabric", *Army Research Laboratory-Technical Report-2891*, (2002).

V.B.C. Tan, T.E. Tay and W.K. Teo, "Strengthening fabric armour with silica colloidal suspensions", *International Journal of Solids and Structures*, **42**:5-6 (2005), 1561-1576.

Caption of Tables

Table 1: Manufacturer's product data of five styles of plain woven Kevlar fabrics

Table 2: Neat fabric weights and strengths measured in this study

Table 3: Material parameters for five styles of neat and 24 wt% nanoparticle impregnated Kevlar fabrics

Table 1: Manufacturer's product data of five styles of plain woven Kevlar fabrics

Fabric style	K310	K706	K720	K745	K779
Fiber type	Comfort	KM-2	129	29	159
Fiber modulus (GPa)	87.0	80.0	99.7	73.0	97.2
Yarn size (Denier)	400	600	1420	3000	200
Weight (g/m^2)	122	180	258	475	132
Warp count (Yarns/in)	35.5	34	20	17	70
Weft count (Yarns/in)	35.5	34	20	17	70
Warp Strength (lbs/in)	530	775	978	1600	385
Weft Strength (lbs/in)	530	880	992	1800	530
Thickness (mm)	0.18	0.23	0.36	0.61	0.18

Table 2: Neat fabric weights and strengths measured in this study

Fabric style	K310	K706	K720	K745	K779
Weight (g/m^2)	127	178	254	435	127
Warp Strength (lbs/in)	630	760	1220	1770	390
Weft Strength (lbs/in)	730	970	1290	1910	670

Table 3: Material parameters for five styles of neat and 24 wt% nanoparticle impregnated Kevlar fabrics

Styles	K310		K706		K720		K745		K779	
NPs (wt%)	0	24	0	24	0	24	0	24	0	24
$E_1^{\alpha 1}$ (GPa)	0.7	1.8	1.5	3.0	1.0	3.0	0.3	2.0	0.7	1.7
$E_1^{\alpha 2}$ (GPa)	20.0	20.0	22.0	22.0	22.5	22.5	16.0	16.0	17.0	17.0
$\varepsilon_{11}^{\alpha 0}$	0.028	0.03	0.025	0.027	0.018	0.020	0.034	0.037	0.093	0.099
$E_1^{\beta 1}$ (GPa)	6.0	6.0	1.8	3.0	1.0	2.5	0.5	1.5	7.0	14.0
$E_1^{\beta 2}$ (GPa)	23.5	23.5	22.0	22.0	26.0	26.0	18.0	18.0	22.5	22.5
$\varepsilon_{11}^{\beta 0}$	0.003	0.003	0.016	0.017	0.014	0.015	0.019	0.02	0.005	0.01
G_{12} (MPa)	0.01	0.6	0.4	1.5	0.15	1.5	0.07	1.7	0.15	9.0
E_2^0 (MPa)	0.5	3.2	2.3	7.5	0.45	5.0	0.5	11.0	3.0	9.5
L_{Lock}	0.70	0.75	0.68	0.73	0.60	0.75	0.67	0.77	0.88	0.93

Caption of Figures

Figure 1: Optical images of five styles of plain woven Kevlar fabrics. (The image size for all the fabrics are 6.4 x 6.4 mm. The true color of the fabrics was bright yellow. They were post-processed to black and white format to enhance the contrast.)

Figure 2: SEM image of K706 fabric with 24 wt% silica nanoparticles

Figure 3: Identifying warp and weft yarns in the fabric – Warp yarns are wavier than weft yarns

Figure 4: Diagram of tension test specimen: (a) Uniaxial tension, (b) Off axis tension (initial configuration) and (c) Off axis tension (deformed configuration)

Figure 5: Schematic diagram of static indentation test
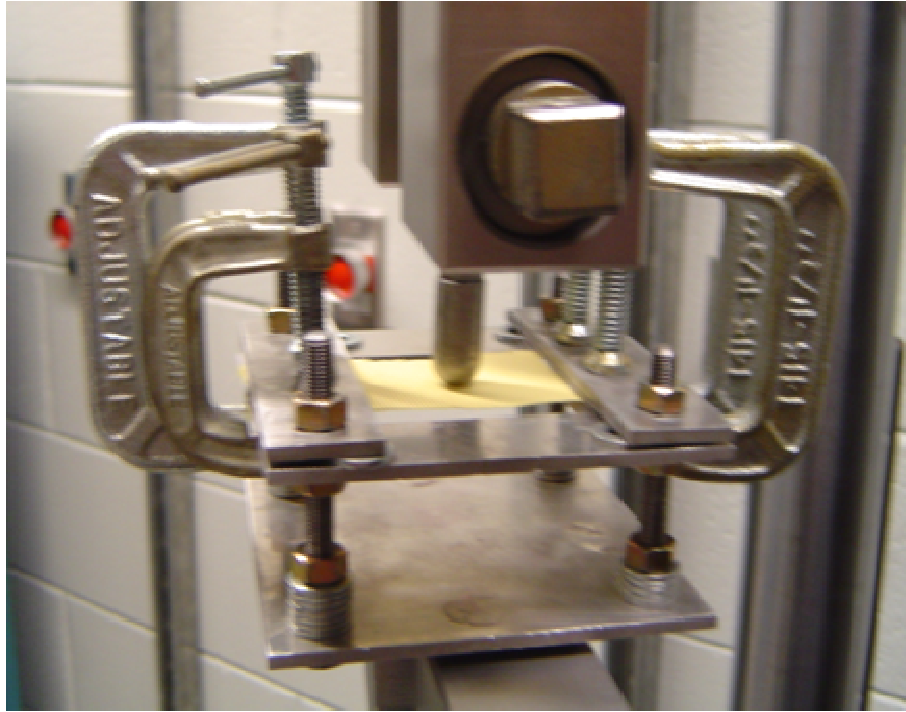
Figure 6: Indentation test on neat K706

Figure 7: Engineering stress versus strain curves from uniaxial tension tests for five styles of Kevlar fabrics with different wt% of nanoparticle addition

Figure 8: Load versus displacement curves from 45° off axis tension tests for five styles of Kevlar fabrics with different wt% addition of nanoparticles

Figure 9: Shear regions in a 45° off axis tension test – schematic diagram and actual deformation.

Figure 10: Coordinate systems

Figure 11: Yarn spacing parameters – initial and deformed configurations

Figure 12: Experimental and numerical load-displacement curves for a (a) 45° and (b) 30° off axis tension test using neat K706 style fabric

Figure 13: A snapshot of the deformation in a 30° off axis tension test using neat K706 style fabric at a grip displacement of 18mm – (a) experimental and (b) simulations

Figure 14: Comparison of the experimental and numerical load versus displacement curves from a static indentation test on 45° neat K706 style fabric
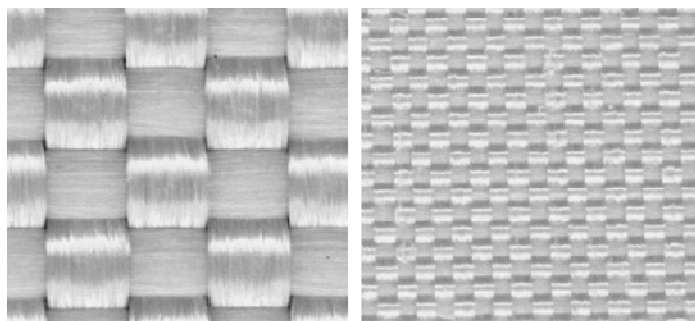
K310   K706   K720

K745   K779

Figure 1: Optical images of five styles of plain woven Kevlar fabrics.

(The image size for all the fabrics are 6.4 x 6.4 mm. The true color of the fabrics was bright

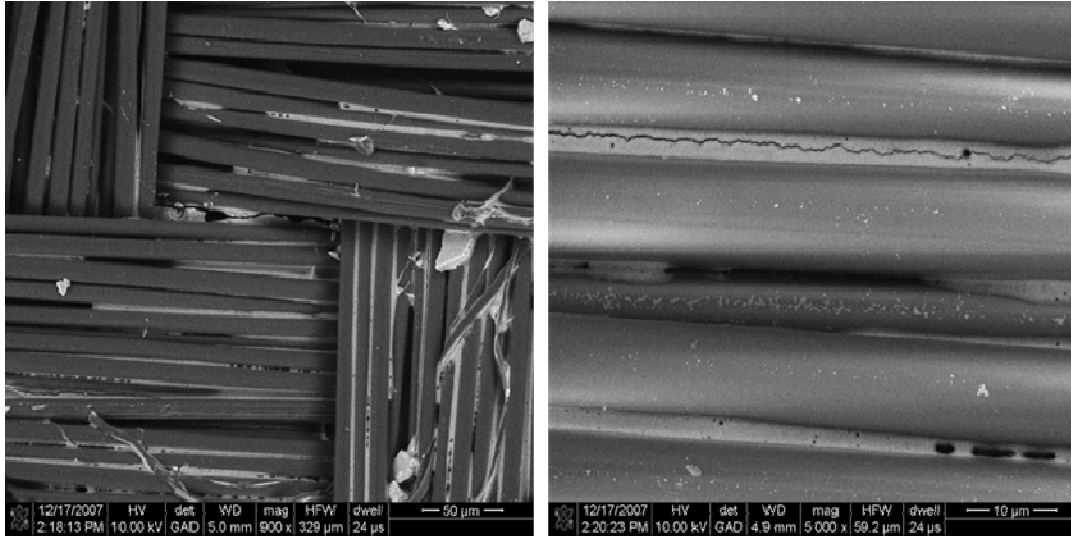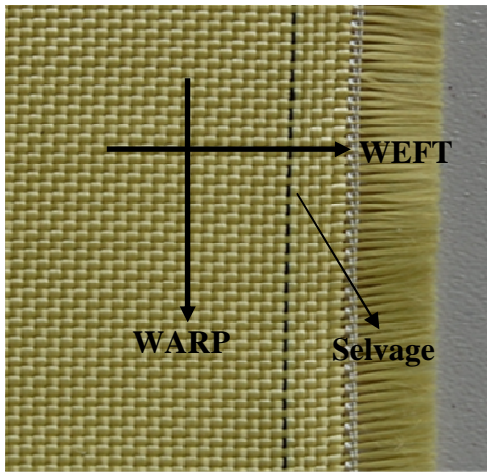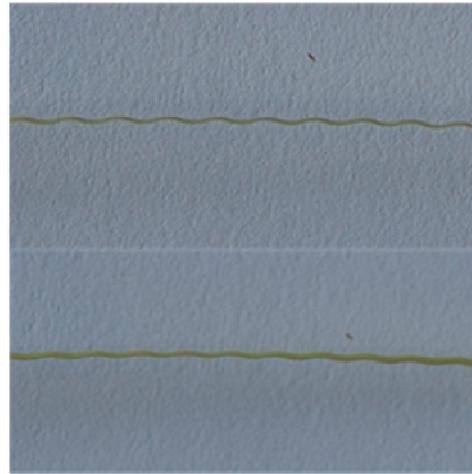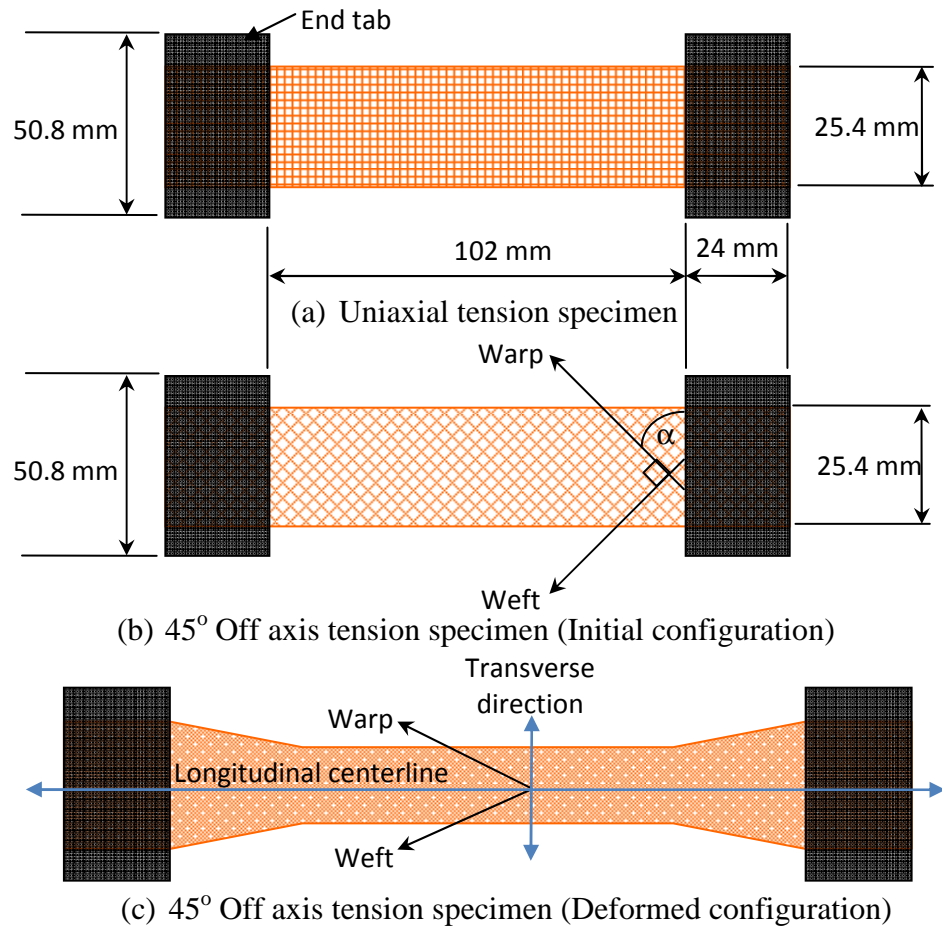yellow. They were post-processed to black and white format to enhance the contrast.)

Figure 2: SEM image of K706 fabric with 24 wt% silica nanoparticles

(a) Selvage on K720   (b) Warp (above) and weft yarns (K720)

Figure 3: Identifying warp and weft yarns in the fabric – Warp yarns are wavier than weft yarns

(a) Uniaxial tension specimen

(b) 45° Off axis tension specimen (Initial configuration)

(c) 45° Off axis tension specimen (Deformed configuration)

Figure 4: Diagram of tension test specimen: (a) Uniaxial tension, (b) Off axis tension (initial configuration) and (c) Off axis tension (deformed configuration)

SIDE VIEW

TOP VIEW

Figure 5: Schematic diagram of static indentation test
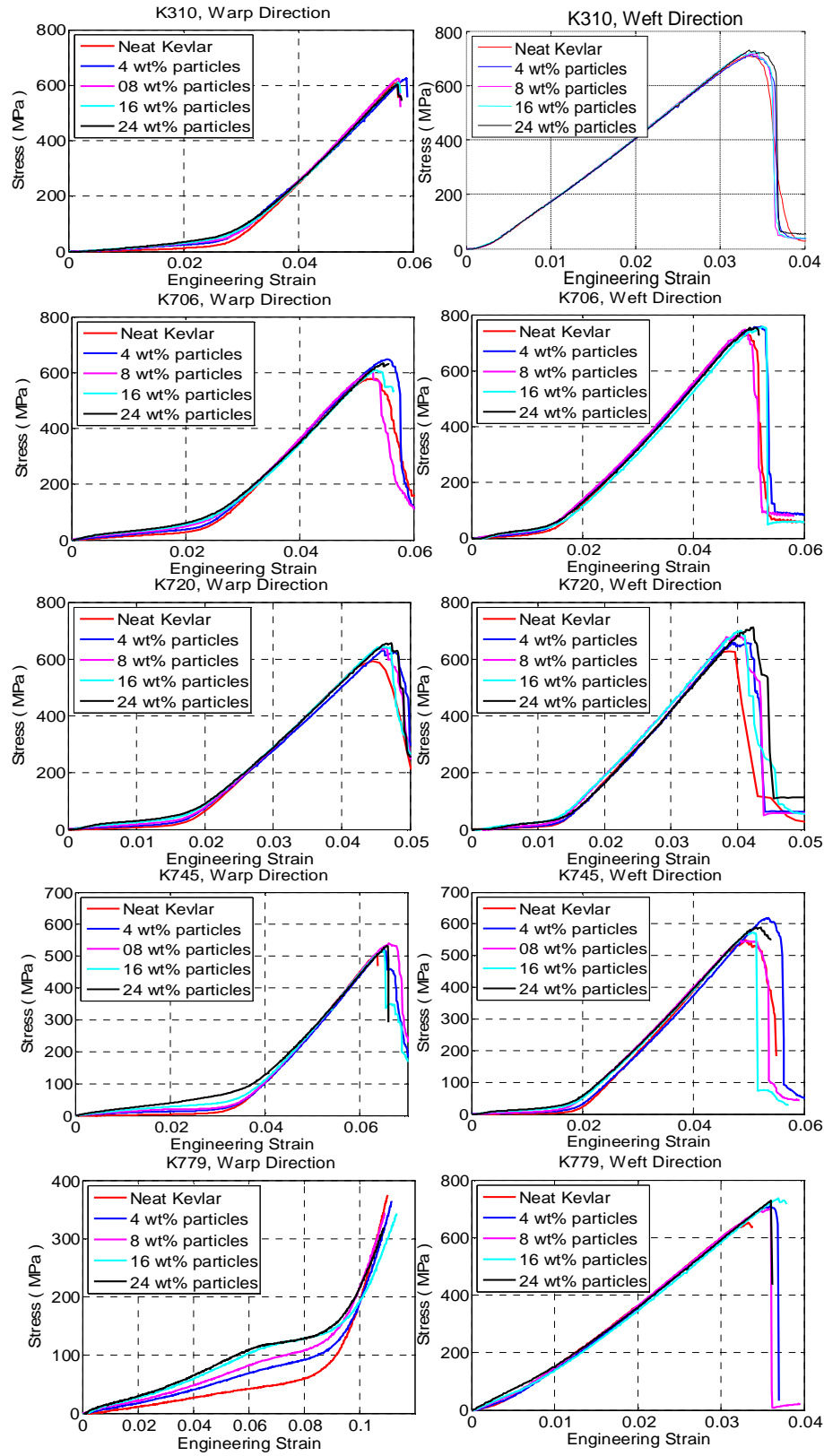
Figure 6: Indentation test on neat K706

Figure 7: Engineering stress versus strain curves from uniaxial tension tests for five styles of
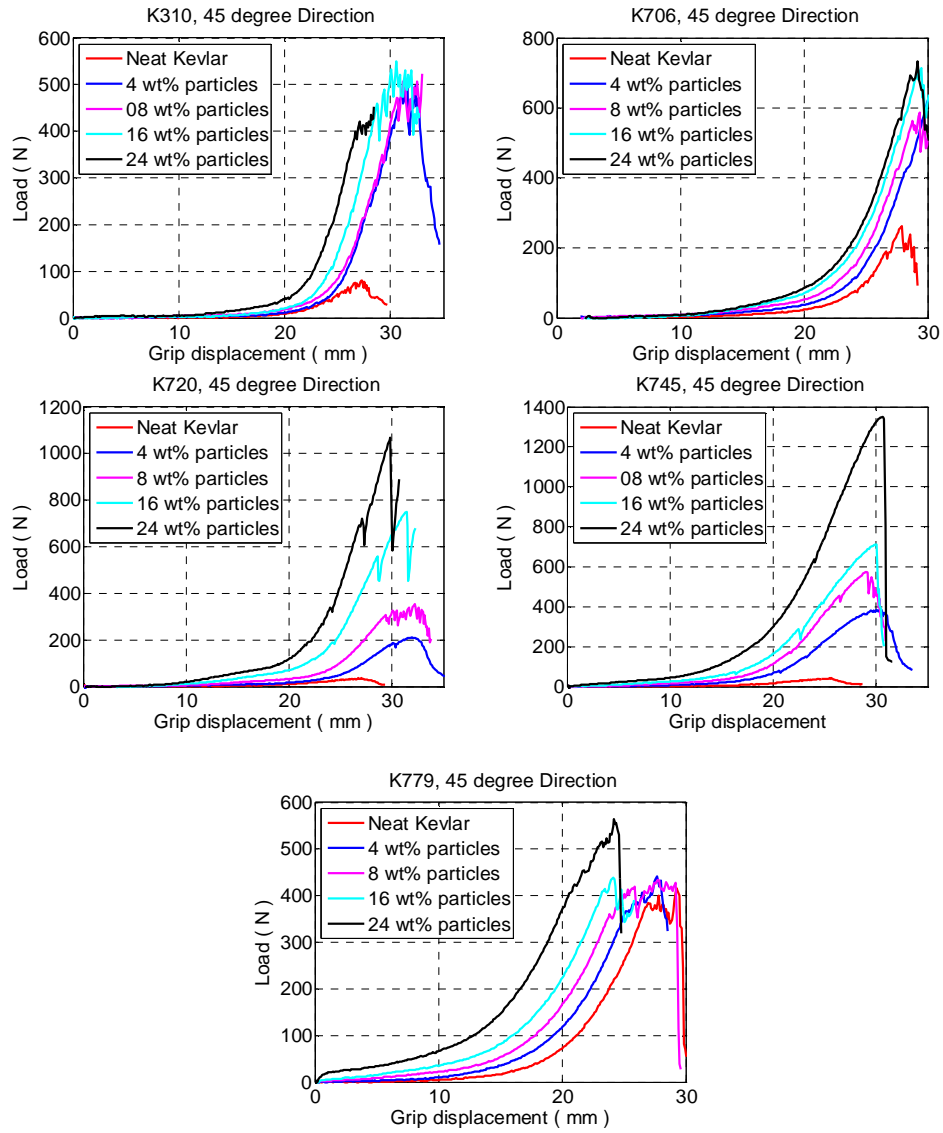Kevlar fabrics with different wt% of nanoparticle addition

Figure 8: Load versus displacement curves from 45° off axis tension tests for five styles of Kevlar fabrics with different wt% addition of nanoparticles
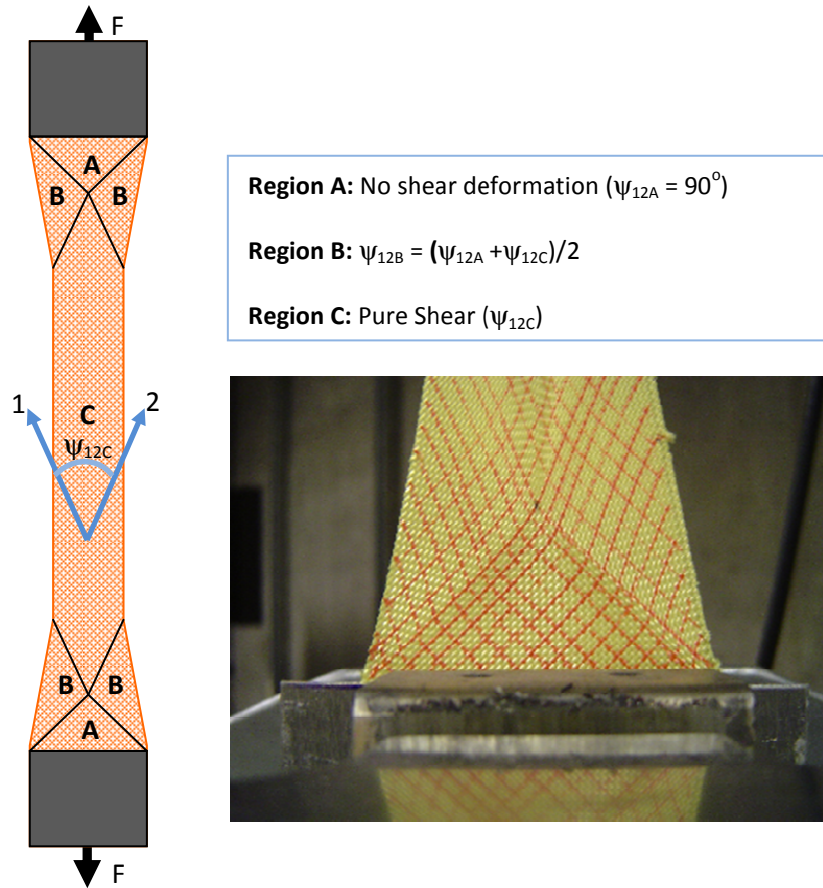
Region A: No shear deformation ($\psi_{12A} = 90^{o}$)

Region B: $\psi_{12B} = (\psi_{12A} + \psi_{12C})/2$

Region C: Pure Shear (ψ_{12C})

Figure 9: Shear regions in a 45° off axis tension test – schematic diagram and actual deformation

(a) Global coordinate system (x-y) and yarn orientations

(b) Local coordinate system (x_1-x_2) for the warp layer

Figure 10: Coordinate systems

Weft direction

Warp direction

$l_{\alpha o}$

$l_{\beta o}$

Weft direction

Warp direction

l_{α}

l_{β}

$$L_{\alpha o} = \frac{l_{\alpha}}{l_{\alpha o}} = 1$$

$$L_{\alpha} = \frac{l_{\alpha}}{l_{\alpha o}} = \left(1 + \varepsilon_{11}^{\beta}\right)\sin\theta$$

$$L_{\beta o} = \frac{l_{\beta}}{l_{\beta o}} = 1$$

$$L_{\beta} = \frac{l_{\beta}}{l_{\beta o}} = (1 + \varepsilon_{11}^{\alpha})\sin\theta$$

(a) Initial configuration
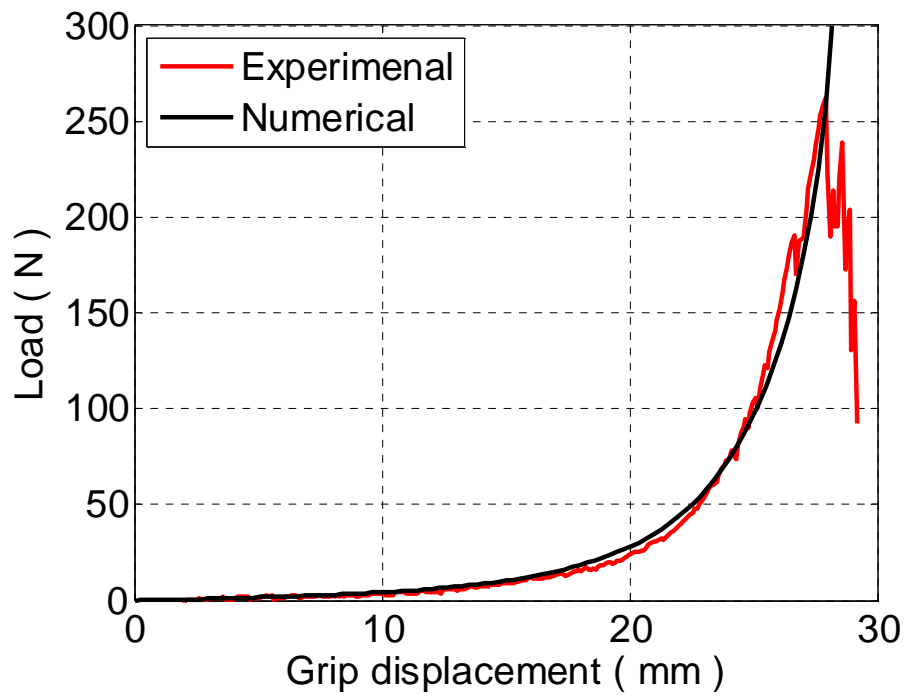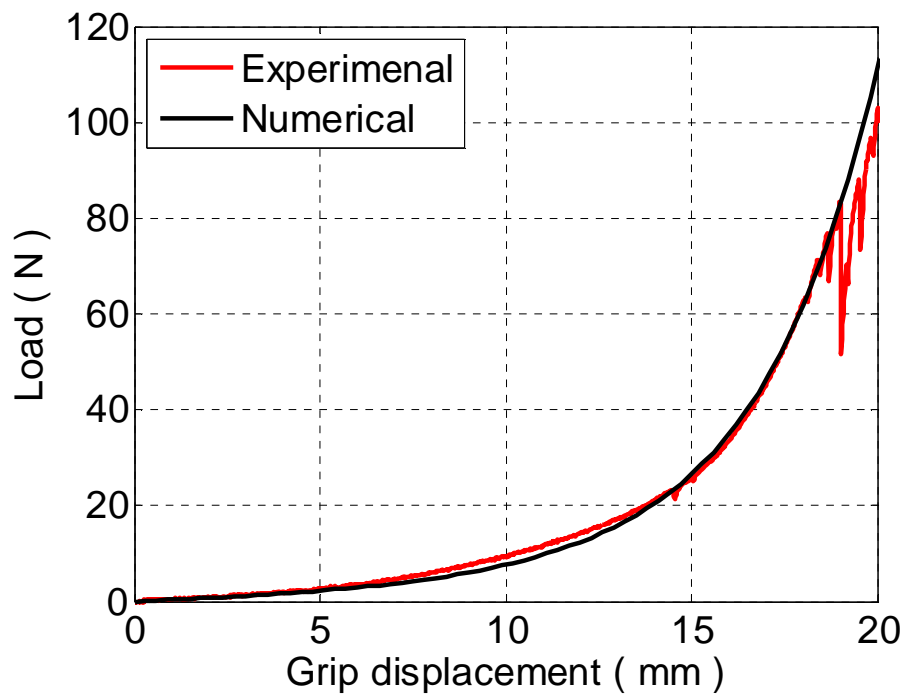
(b) Deformed configuration

Figure 11: Yarn spacing parameters – initial and deformed configurations

(a) 45° off axis tension test (neat K706)

(b) 30° off axis tension test (neat K706)

Figure 12: Experimental and numerical load-displacement curves for a (a) 45° and (b) 30° off axis tension test using neat K706 style fabric
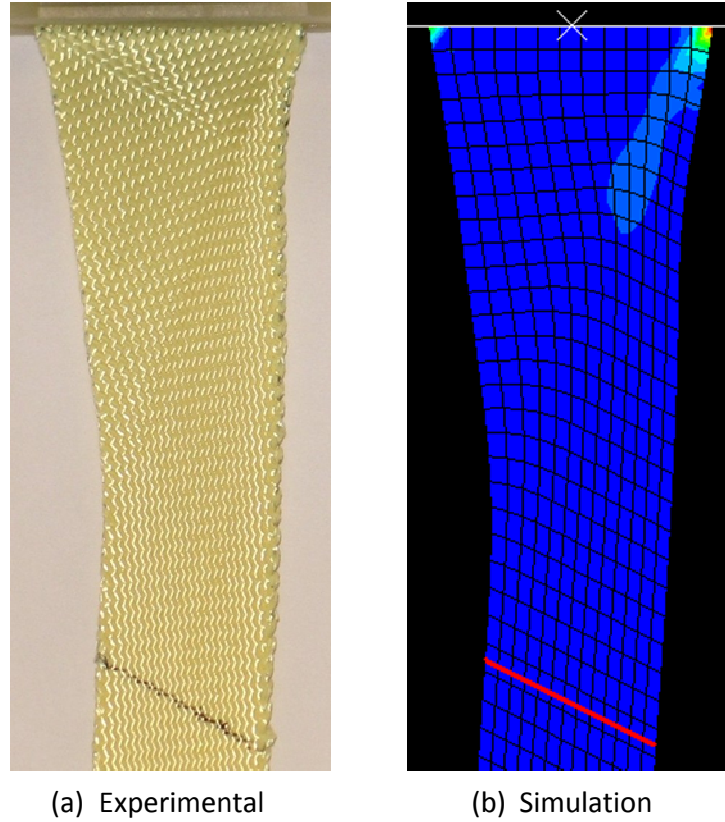
(a) Experimental	(b) Simulation

Figure 13: A snapshot of the deformation in a 30$^{\text{o}}$ off axis tension test using neat K706 style fabric at a grip displacement of 18mm – (a) experimental and (b) simulations

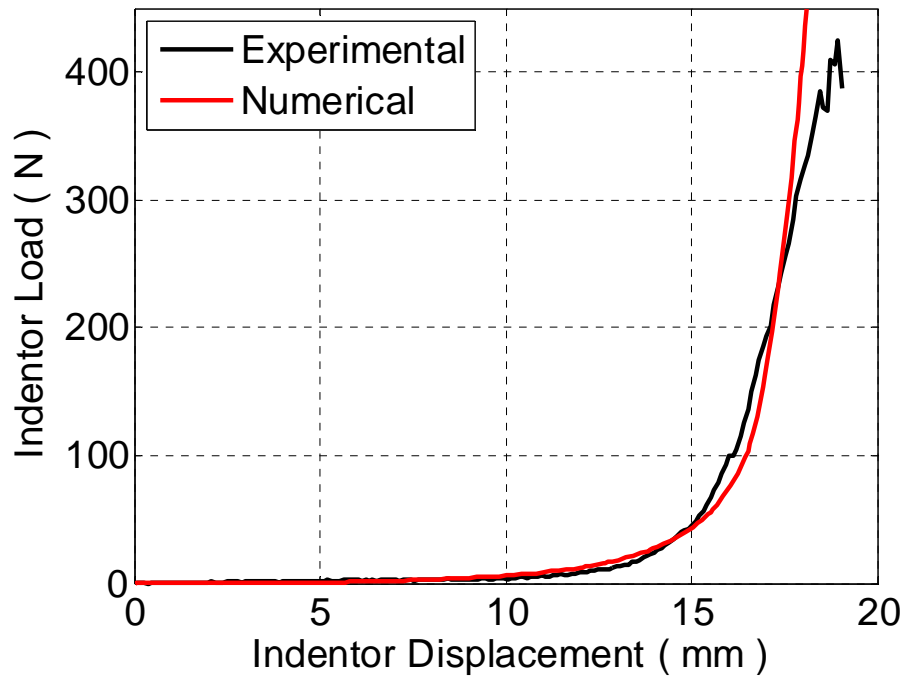Figure 14: Comparison of the experimental and numerical load versus displacement curves from a static indentation test on 45° neat K706 style fabric